eman ta zabal zazu

Universidad del País Vasco

Euskal Herriko Unibertsitatea

Radiolabelling and preclinical evaluation of nanoparticles as drug delivery systems: Application to infectious pulmonary diseases

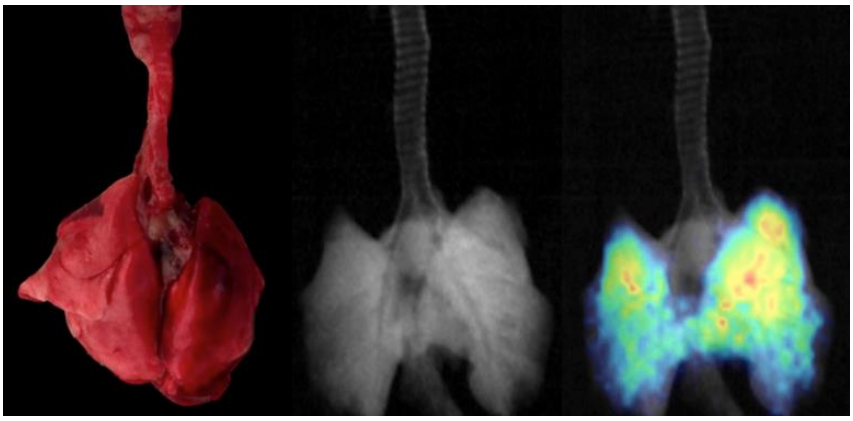

Unai Cossío Arrieta

Donostia, 2018

Table of Contents

Summary ..... **i**

Resumen ..... **iii**

Chapter 1. General introduction **1**

1.1. Nanoparticles and nanomedicine **1**

1.1.1. Nanoparticle: definition and applications 1

1.1.2. NP types 1

1.1.3. Polymeric NPs 1

1.1.4. NPs in Nanomedicine: Oncology 6

1.1.5. NPs in Nanomedicine: Bacterial respiratory infection 8

1.2. Tracing NPs *in vivo*: nuclear imaging techniques **9**

1.2.1. The need for tracking 9

1.2.2. Nuclear imaging: general aspects 10

1.2.3. Radioactive isotopes 10

1.2.4. Gamma-ray detection 12

1.2.5. The key step: Radiolabelling 14

1.3. References **17**

Chapter 2. Motivation and objectives of the thesis **25**

2.1. Justification of the study: The PneumoNP Project **25**

2.2. Objectives **28**

2.3. References **28**

Chapter 3. Development of novel tracers for the assessment of lung ventilation using Positron Emission Tomography **29**

3.1. Introduction **29**

3.2. Objectives **35**

3.3 Experimental Part **36**

3.3.1 Production and analysis of $[^{18}F]CF_4$ and $[^{18}F]SF_6$ 36

3.3.2 Imaging studies 38

3.4 Results and Discussion **39**

3.4.1. Production and analysis of $[^{18}F]CF_4$ and $[^{18}F]SF_6$ 39

3.4.2. Imaging Studies 42

3.5 Summary and Conclusion **45**

3.6. References **45**

Chapter 4. Evaluation of pulmonary administration methods in rodents using nuclear imaging techniques **47**

4.1. Introduction **47**

4.2. Objectives **49**

4.3 Experimental Part **50**

4.3.1 Animal experiments: general 50

4.3.2. Droplets size measurements 53

4.3.3. *In vivo* imaging experiments 54

4.3.4. *Ex vivo* imaging experiments 55

4.4 Results and discussion **55**

4.4.1. Aerosol droplet size measurements 55

4.4.2. *In vivo* imaging experiments 57

4.4.3. *Ex vivo* imaging experiments 60

4.5 Summary and Conclusions **64**

4.6. References **64**

Chapter 5. Evaluation of the pharmacokinetic properties of novel nanoparticle-based antibiotics after lung administration using Positron Emission Tomography 67

5.1. Introduction 67

5.2. Objectives 70

5.3. Experimental Part 71

5.3.1 General remarks 71

5.3.2 Radiolabelling 71

5.3.2.3. Radiolabelling of AMPs 72

5.3.2.4. Preparation of AMP-NP conjugates 73

5.3.3 Animal Experiments 76

5.4. Results and discussion 78

5.4.1. Radiolabelling 78

5.4.2. Animal Experiments 85

5.5. Summary and Conclusion 92

5.6. References 92

Chapter 6. General conclusions 97

Acknowledgments 99

Summary

According to the World Health Organization (WHO) the threat of global antibiotic resistance of bacteria is no longer a prediction, but a reality; indeed, it affects every region of the world and potentially people of any age. Antibiotic resistant Gram-negative bacteria are one of the major issues currently affecting global health, mainly due to a lack of effective antibiotic therapy for this type of infection. Within this context, the EU Commission launched a call in 2013 encouraging the development of novel nanotherapeutics to treat bacterial infectious diseases. One of the projects selected in this call was the PneumoNP project, a collaborative work funded under the FP7-NMP-2013-LARGE-7 call (No. 604434 grant). The aim of the project was to develop a therapeutic system for the treatment of lung Gram-negative bacterial infections, based on the combination of an antimicrobial peptide (AMP) and a nanocarrier (NC) to yield the resulting nanomedicine (or nanosystem, NS), and focusing the attention on *Klebsiella pneumoniae* caused infections for proof of concept experiments. In parallel, the project aimed at developing a new nebulization system for the administration of aerosols in experimental animals and the validation of a diagnostic kit.

The consortium as a whole included 11 partners from 6 member states (Spain, Germany, Italy, France, The Netherlands and Denmark) coming from different scientific and technological disciplines. Two of the partners were devoted to the development of novel antimicrobial peptides (AMPs); two of the partners were devoted to the preparation of nanocarriers and the development of strategies for the formation of the nanosystems; one of the partners was in charge of developing a new nebulizer for the administration of the aerosols to rodents and another partner was in charge of performing *in vivo* proof of efficacy studies with selected NSs in relevant animal models.

In this context, The Radiochemistry and Nuclear Imaging Group at CIC biomaGUNE, in which this PhD thesis has been carried out, had two major roles: (i) To evaluate the novel nebulization system developed within the project; and (ii) to assess the

biodistribution and basic pharmacokinetic properties of the nanosystems developed in the context of the project using *in vivo* imaging.

The work performed in this thesis has been divided in three main parts, which result in the three experimental chapters. First, a new tool for the assessment of lung ventilation using Positron Emission Tomography (PET) has been developed and evaluated in healthy (wild type) animals (rats). Despite this task was not formally included in the PneumoNP project description and the results have not been used in the context of the PneumoNP project, it is considered as an essential tool for future works. Indeed, evaluation of the biodistribution or determination of pharmacokinetic properties of new chemical/biological entities after lung administration requires previous evidence of unaltered ventilation, which can be assessed efficiently and with high sensitivity with the newly developed tool.

The second part of the PhD thesis focused on the evaluation of the new nebulization system and its comparison towards commercially available systems. In this chapter, and by using a straightforward methodology to radiolabel the aerosol, the new system was evaluated using PET in terms of uniformity of deposition of the aerosol in the lungs and the percentage of the aerosol that was actually released in the target organ.

The last part of this PhD thesis pursued the determination of the residence time in the lungs of two novel AMPs after lung administration, both as free peptides and in combination with nanocarriers. With that aim, radiolabelling strategies to incorporate either positron or gamma emitters into the different species were developed. In addition, imaging studies were conducted to determine the residence time in the lungs of the labelled AMPs and, eventually, of the nanocarriers. These studies provided evidence about the feasibility of nuclear imaging techniques to investigate innovative nanomedicines in the preclinical setting, where they can provide information about the advantages and limitations of using nanocarriers as drug delivery systems. Additionally, essential pharmacokinetic information for proper planning of therapeutic experiments could be obtained.

Resumen

La mayoría de los actores y responsables internacionales del sector de la salud pública coinciden en que las infecciones provocadas por bacterias Gram-negativas resistentes a los antibióticos constituyen una de las mayores amenazas para la salud mundial a día de hoy, principalmente debido a la falta de antibióticos eficaces para este tipo de infecciones. Diferentes autoridades incluyendo la Unión Europea (UE), la Organización Mundial de la Salud (OMS) o las Naciones Unidas (NU) son conscientes de la gravedad de este problema y por ello están invirtiendo recursos económicos, estructurales y organizativos con el objetivo de resolver el problema de la resistencia a antibióticos. En este contexto, la Comisión de la UE lanzó una convocatoria en el año 2013 para promover el desarrollo de nanoterapias para el tratamiento de enfermedades infecciosas bacterianas.

Uno de los proyectos seleccionados en esta convocatoria fue el proyecto PneumoNP, un proyecto colaborativo financiado bajo el Programa Marco FP7. El objetivo de este proyecto era desarrollar antibióticos basados en nanosistemas inhalables para el tratamiento de infecciones pulmonares causados por la bacteria Gram-negativa *klebsiella pneumoniae.* Estos nanosistemas estaban formados por péptidos antimicrobianos (que son los principios activos o fármacos) unidos a diferentes nanovehículos. En paralelo, el proyecto también pretendía desarrollar un nuevo sistema de nebulización para la administración de aerosoles a pequeños animales (ratas) y la validación de un kit de diagnóstico.

El consorcio estaba formado por 11 socios de 6 países europeos diferentes (España, Italia, Francia, Alemania, Holanda y Dinamarca) procedentes de diferentes disciplinas científicas y tecnológicas. Dos de estos socios, SetLance srl (SET, Italia) y Adenium Biotech (ADE, Dinamarca) fueron los encargados de desarrollar los nuevos péptidos antimicrobianos. Otros dos socios, CIDETEC (CID, España) y la Universidad de Utrecht (UU, Holanda), se dedicaron a la preparación de los nanovehículos y al desarrollo de estrategias para la formación de los nanosistemas. Uno de los socios, Ingeniatrics

Tecnologías (INGEN, España), estaba al cargo del desarrollo del sistema de nebulización para la administración de los aerosoles a los roedores (ratas). Por último, Pathofinder BV (PAT, Alemania) y el Erasmus Medical Center (EMC, Holanda) estuvieron a cargo del desarrollo del kit de diagnóstico y de realizar estudios *in vivo* para evaluar la eficacia de los nanosistemas seleccionados en modelos animales relevantes, respectivamente.

En este gran proyecto, el grupo de Radioquímica e Imagen Nuclear de CIC biomaGUNE (en el que se ha llevado a cabo la tesis doctoral) abordó dos objetivos principales: (i) evaluar el nuevo sistema de nebulización desarrollado por Ingeniatrics Tecnologías; y (ii) determinar la biodistribución y las propiedades farmacocinéticas de los nanosistemas desarrollados. Tal como se planteó inicialmente en la propuesta del proyecto, la evaluación debería realizarse utilizando técnicas de imagen nuclear como la Tomografía por Emisión de Positrones (PET, de sus siglas en inglés) o la Tomografía Computarizada de Emisión de Fotón Único (SPECT), en combinación con otras modalidades de imagen como la Tomografía Computarizada (CT).

El trabajo llevado a cabo en este doctorado se ha dividido en tres partes, que corresponden a los capítulos 3, 4 y 5 del presente documento.

En la primera parte del trabajo (**Capítulo 3**), se presenta el desarrollo de una nueva herramienta para la evaluación de la ventilación pulmonar en ratas sanas (*wild type*), utilizando la tecnología PET. A pesar de que esta tarea no se incluyó formalmente en la descripción inicial del proyecto PneumoNP y los resultados no se han utilizado en el contexto del proyecto, se considera como una herramienta esencial para trabajos futuros. De hecho, la evaluación de la biodistribución o determinación de las propiedades farmacocinéticas de nuevas entidades químicas/biológicas tras la administración pulmonar requiere evidencia previa de una ventilación no alterada, que puede evaluarse de manera eficiente y con alta sensibilidad con la herramienta recientemente desarrollada.

La herramienta para la determinación de la ventilación pulmonar se basa en la utilización de dos gases radiofluorados ($[^{18}F]CF_4$ y $[^{18}F]SF_6$), siguiendo una metodología

completamente innovadora. Estos gases son adecuados para este tipo de estudios, ya que no son tóxicos al ser químicamente inertes en condiciones fisiológicas y son prácticamente insolubles en sangre, evitando así la translocación a otros órganos. La metodología utilizada para generar estos radiotrazadores, consistió en un proceso de irradiación de protones en dos etapas (ver Figura 1): en la primera, el blanco del ciclotrón se rellena con oxígeno puro ($[^{18}O]O_2$) y se irradia con protones para generar el radioisótopo ^{18}F (tiempo de vida media de 109.8 minutos) mediante la reacción nuclear $^{18}O(p,n)^{18}F$. Tras recuperar el gas irradiado, se rellena el blanco con una mezcla de gases CF_4/Ne o SF_6/Ne (el neón se utiliza como gas portador). Mediante una segunda irradiación con protones (etapa 2) se promueve una reacción de intercambio isotópico entre los átomos de flúor del gas y el flúor-18 radiactivo, que queda absorbido en las paredes del blanco tras la primera irradiación, consiguiendo así el gas radiofluorado deseado.

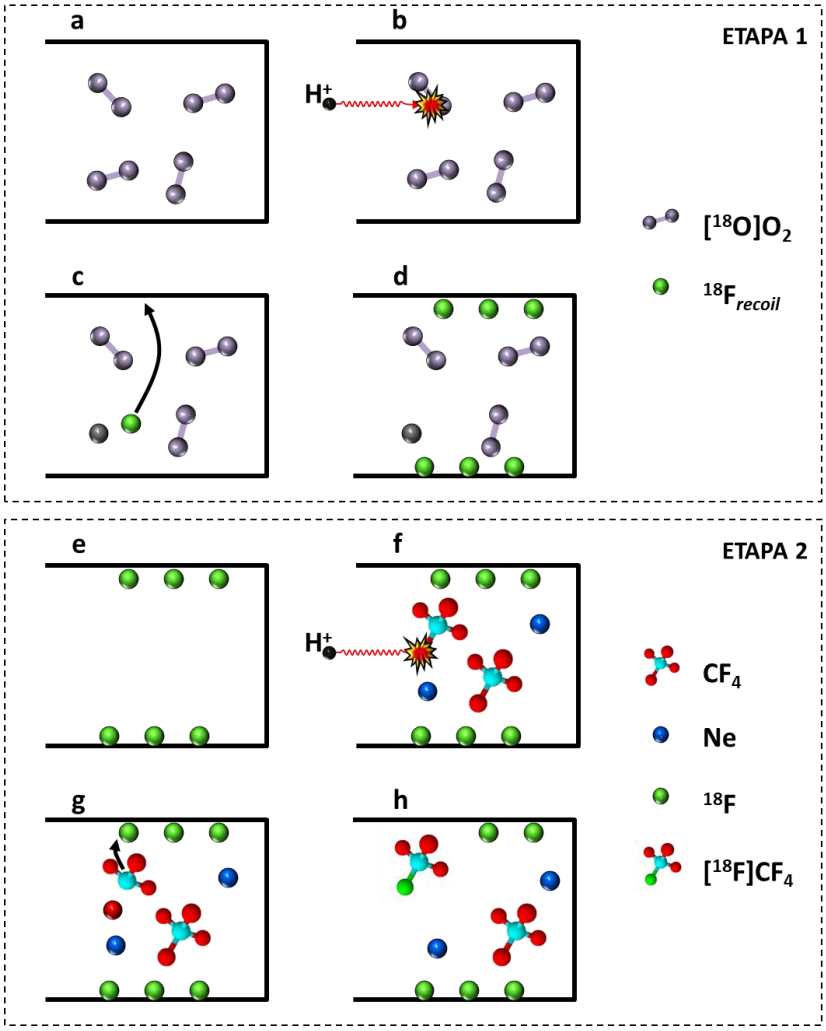

Figura 1. Procedimiento seguido para la producción del gas $[^{18}F]CF_4$. En la etapa 1, el gas $[^{18}O]O_2$ (a) es irradiado con protones (b) para generar el isótopo ^{18}F (reacción nuclear $^{18}O(p,n)^{18}F$), el cual permanece absorbido en las paredes del blanco (c y d). En la etapa 2, después de extraer el $[^{18}O]O_2$ (e), el blanco se rellena con una mezcla de gases CF_4/Ne (f). Durante la segunda irradiación de protones (f), se generan iones (g) que en las condiciones de alta temperatura y presión dan lugar a la formación de $[^{18}F]CF_4$ (h).

Siguiendo el procedimiento descrito y bajo las condiciones optimizadas se obtuvieron hasta 8.43±0.59 GBq de gas $[^{18}F]CF_4$ puro y 6.77±0.21 GBq de $[^{18}F]SF_6$. Los ensayos destinados a determinar la utilidad de los gases radiofluorados como marcadores de ventilación pulmonar se llevaron a cabo en ratas. Para ello, se mezcló oxigeno gas (vehículo) con los gases radiactivos (cantidad total de radiactividad = 74±8 MBq) y estas mezclas fueron administradas a las ratas (ver Figura 2).

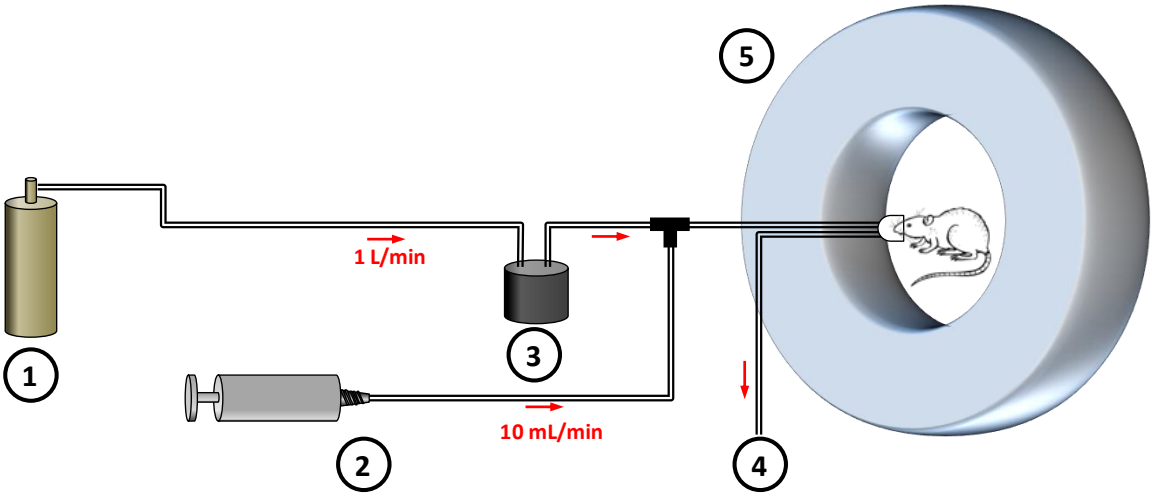

Figura 2. Ilustración del sistema de administración utilizado para llevar a cabo los experimentos de PET; (1) O_2 gas; (2) jeringa hermética con gas radiactivo ([^{18}F]CF_4 o [^{18}F]SF_6); (3) vaporizador de isoflurano; (4) vía de escape; (5) cámara PET-CT.

Inmediatamente después, se llevaron a cabo estudios de imagen PET y se analizaron las diferentes curvas actividad/tiempo de cada sujeto. Como puede observarse en la Figura 3, estas curvas mostraban un aumento brusco de radiactividad justo después del inicio de la administración del gas radiofluorado. Cuando se interrumpió la administración, se logró una eliminación casi completa del gas de los pulmones en pocos segundos. Asimismo, las imágenes PET obtenidas en estos estudios mostraron una distribución uniforme del gas dentro de los pulmones.

Debido a la alta eficacia del método de producción descrito más arriba, y a la semivida (o vida media) relativamente larga del Flúor-18, nuestros resultados sugieren que los gases fluorados podrían convertirse en herramientas muy útiles para el diagnóstico, el pronóstico o la evaluación de la respuesta al tratamiento para una amplia variedad de enfermedades pulmonares.

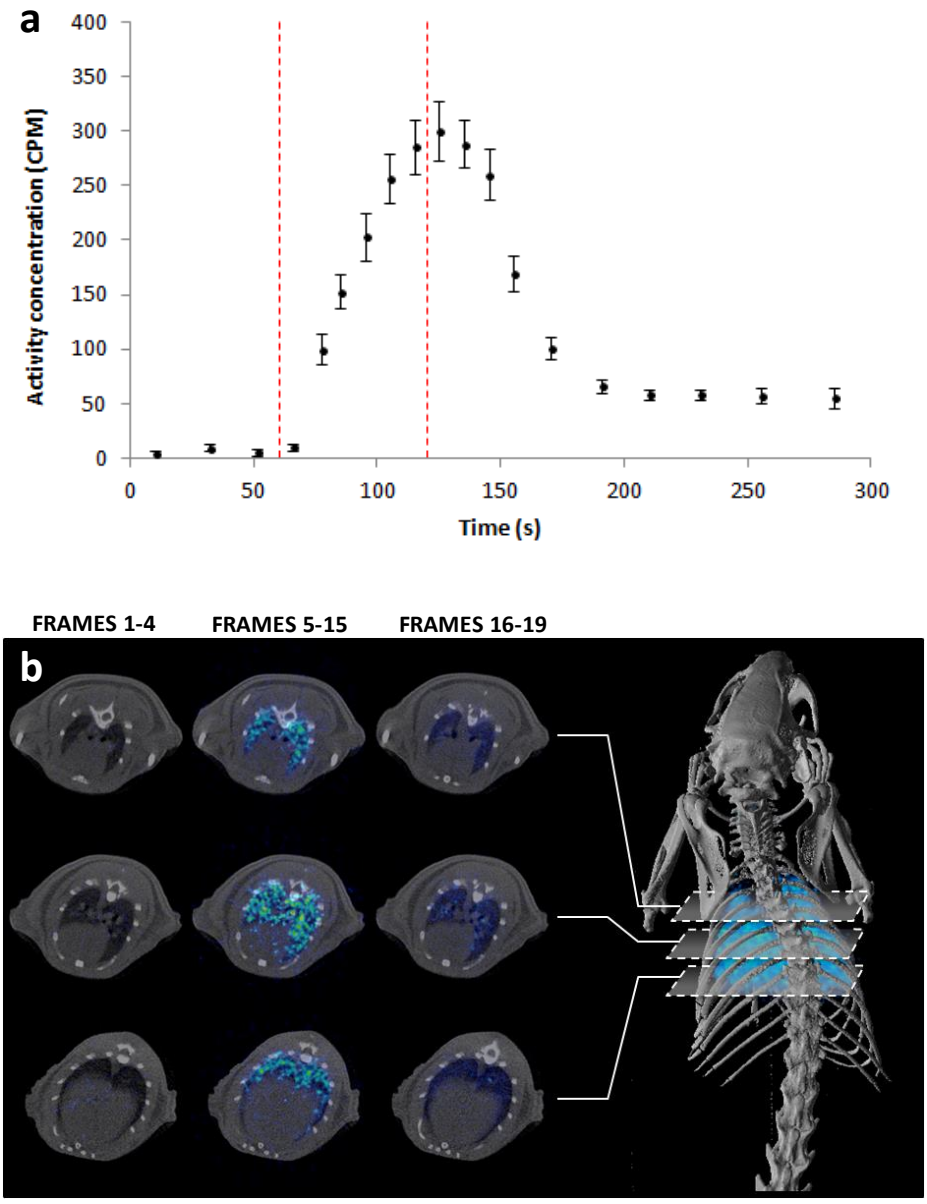

Figura 3. a) Concentración de radiactividad (unidades arbitrarias, cuentas por minuto, CPM) en los pulmones en función del tiempo (promedio ± desviación estándar, n=2). (b) Izquierda: imágenes PET-CT axiales de la cavidad torácica, antes (*frames* 1-4), durante (*frames* 5-15) y después (*frames* 16-19) de la administración del gas [^{18}F]CF_4; derecha: imagen CT en 3D del esqueleto corregistrado con la imagen PET en 3D de los pulmones (promedio de los *frames* 5-15).

En la segunda parte del trabajo (**Capítulo 4**), se describe la evaluación del nuevo sistema de nebulización desarrollado por Ingeniatrics y la comparación de éste con otros dos sistemas de administración pulmonar comercialmente disponibles. Estos dos dispositivos eran por un lado, el generador de microspray de la de la compañía

PennCentury (FMJ-250 High Pressure Syringe Model, PennCentury. Inc. Wyndmoor, USA) y el nebulizador comercial de la compañía Aeroneb (Aeroneb® Lab Micropump Nebulizer). Para evaluar y comparar tanto la eficiencia de deposición como la distribución regional del aerosol tras la administración utilizando los diferentes sistemas, el aerosol fue previamente marcado con 2-deoxi-2-(^{18}F)fluoro-D-glucosa ([^{18}F]FDG); este radiotrazador es ampliamente conocido en el ámbito clínico, y se utiliza principalmente para el diagnóstico precoz y la evaluación de respuesta a tratamientos de diferentes tipos de cáncer.

Tras la administración pulmonar del radiotrazador se llevaron a cabo estudios PET *in vivo* para determinar la distribución regional del aerosol utilizando los diferentes dispositivos. Tras adquisición de las imágenes, la cuantificación de las mismas se llevó a cabo mediante delineación de diferentes regiones de interés (ROIs) en las diferentes zonas de los pulmones, para posteriormente determinar la cantidad de radiactividad presente en dichas regiones. Paralelamente a los estudios de imagen, se llevaron a cabo estudios *ex vivo*, tanto para confirmar estos resultados como para evaluar la eficacia de los dispositivos en términos de deposición pulmonar de aerosoles. Con este fin, una vez finalizados los estudios de imagen se extrajeron los pulmones de los animales y se dividieron según los diferentes lóbulos. Finalmente, se midió la cantidad de radiactividad presente en dichos lóbulos utilizando una cámara de ionización/rayos gamma (WIZARD2 Gamma Counter, PerkinElmer, Waltham, USA). Al mismo tiempo, se determinó la eficiencia de deposición de cada método calculando la fracción depositada en los pulmones respecto a la cantidad administrada.

Según los resultados obtenidos en los ensayos *in vivo* y *ex vivo*, la distribución regional del aerosol en los pulmones es homogénea cuando la administración se lleva a cabo con cualquiera de los nebulizadores (Ingeniatrics y Aeroneb), mientras que el patrón de distribución es muy irregular cuando la administración se lleva a cabo con el generador de miscrospray PennCentury. Por otro lado, los resultados de los ensayos *ex vivo* confirmaron que, utilizando cualquiera de los dos nebulizadores (Ingeniatrics o Aeroneb), solamente el 0.1% de lo nebulizado se deposita en los pulmones; por el

contrario, más del 85% de la fracción nebulizada termina en los pulmones cuando la administración se lleva a cabo mediante el microspray PennCentury.

La tercera y última parte del presente trabajo (**Capítulo 5**) ha consistido en la evaluación mediante PET del tiempo de residencia en el pulmón de los dos péptidos antimicrobianos desarrollados por los socios SET y ADE tras la administración pulmonar, bien en su forma libre o conjugados con diferentes nanovehículos. En primer lugar, se estudiaron diferentes estrategias para incorporar un radioisótopo emisor de positrones o de fotones gamma a los diferentes compuestos (péptidos y nanovehículos). Puesto que los péptidos desarrollados por SET y ADE incorporaban una unidad tirosina, se optó por una estrategia de radio-yodación por sustitución electrofílica aromática, utilizando yodo-124 (isótopo emisor de positrones con una vida media superior a los 4 días) para permitir los estudios de imagen. Asimismo, uno de los nanovehículos se marcó mediante formación de un complejo agente quelante-radiometal, utilizando para ello galio-67, emisor de fotones gamma con una vida media de algo más de tres días.

Una vez implementadas las estrategias de marcaje, tanto los péptidos como los nanovehículos como sus combinaciones fueron administrados en ratas *wild type* utilizando el generador de microspray PennCentury (que se consideró el sistema más adecuado en el contexto de este proyecto, tras analizar los resultados incluidos en el capítulo 4) y se llevaron a cabo estudios de imagen para determinar el tiempo de residencia en los pulmones tanto de los péptidos marcados como de los nanovehículos seleccionados.

Estos estudios confirmaron que las técnicas de imagen nuclear son adecuadas para la investigación preclínica de nuevas nanomedicinas, y que las propiedades farmacocinéticas de los fármacos pueden alterarse significativamente mediante el uso de nanovehículos.

Chapter 1. General introduction

1.1. Nanoparticles and nanomedicine

1.1.1. Nanoparticle: definition and applications

Nanoparticles (NPs) are generally defined as particles between 1 and 100 nanometres (nm) in size, in at least one dimension. Due to their small size and large surface area, nanoparticles (NPs) have physico-chemical properties that differ from bulk materials or larger mesh powders, which make them attractive as e.g. catalysts (1), food additives (2), semiconductors (3) or additives for cosmetics (4), among others. In addition, by appropriate modification of their surface, NPs can become stable in water and biocompatible, and can be functionalised with bioactive tags which facilitate selective or preferential interaction with specific receptors or transporters. Because of this, they have emerged as potential drugs or drug-delivery systems.

1.1.2. NP types

NPs can be made from a large number of materials including proteins, peptides, polymers, lipids, metals and metal oxides, and carbon. In addition, NPs of multiple sizes and shapes can be prepared. As a consequence, there are different options to classify NPs, based e.g. on their properties, structure, size, etc. In this thesis, only polymeric NPs will be described to some extent, as these are the NPs that have been used in the experimental part. The description of the other types of NPs is out of the scope of this chapter, although excellent reviews can be found in the literature (5).

1.1.3. Polymeric NPs

Polymeric nanoparticles (PNPs) have received increased attention in biomedicine, where they are frequently used to improve the therapeutic worth of drugs and bioactive molecules by improving their bioavailability, solubility in physiological environment and retention time in the target organ or tissue (6, 7). Polymeric nanoparticles are optimal carriers for drug delivery due to their tunable characteristics

and high capacity to entrap, dissolve, or be attached to drug molecules or other active principles, overcoming thus limitations of traditional therapies such as low absorption of drugs, short biological half-life, low specificity and un-desired side effects. During the last years, many efforts have been done to render PNPs suitable for *in vivo* applications. Materials used for nanomedicine should fulfil several requirements including high biocompatibility and biodegradability, low toxicity, appropriate elimination and ease of processing (8).

Polymeric nanoparticles can be made of either synthetic or natural polymers, although synthetic polymers present certain advantages, as (i) they can be tailored to give a wider range of desired properties, such as controlled linearity/branching, hydrophobicity, or molecular weight; (ii) they frequently show good biocompatibility and biodegradability; and (iii) they result in better lot-to-lot uniformity than natural materials (9).

Different types of synthetic polymers have been used to prepare PNPs with application in biomedicine, including polyesters, polyurethanes, polyacrylamides and poly(amino acids) (10). Among these, the aliphatic polyesters polylactic and polyglicolic acids as well as their copolymer poly(lactic-co-glicolic) acid (PLGA) have been approved by the *Food and Drug Administration* (FDA) for drug delivery and biomedical applications. These polymers undergo complete biodegradation in physiological medium *via* hydrolytic degradation of the ester linkages, resulting in the formation of the original monomers and lactic and glycolic acids, which are rapidly metabolized (11).

Amphiphilic block copolymers, formed by two types of monomers or polymeric chains, typically one hydrophilic and one hydrophobic, have been also increasingly utilized. Examples of these kind of copolymers are polyesters, poly(amino acids) or poly(acrylic acids) covalently bound or copolymerized with polyethylene glycol (PEG) (12-14).

Natural polymers including polysaccharides (15), dextran (16), chitosan (17), and alginate (18), among others, have also been applied to the preparation of PNPs (19-21). They are generally non-toxic, exhibit high biodegradability and biocompatibility and they are often ready for use without expensive preparation/purification steps.

Polymeric NPs can be classified in different groups, according to their structure: Polymeric nanospheres, polymersomes, nanocapsules and micelles (Figure 1.1).

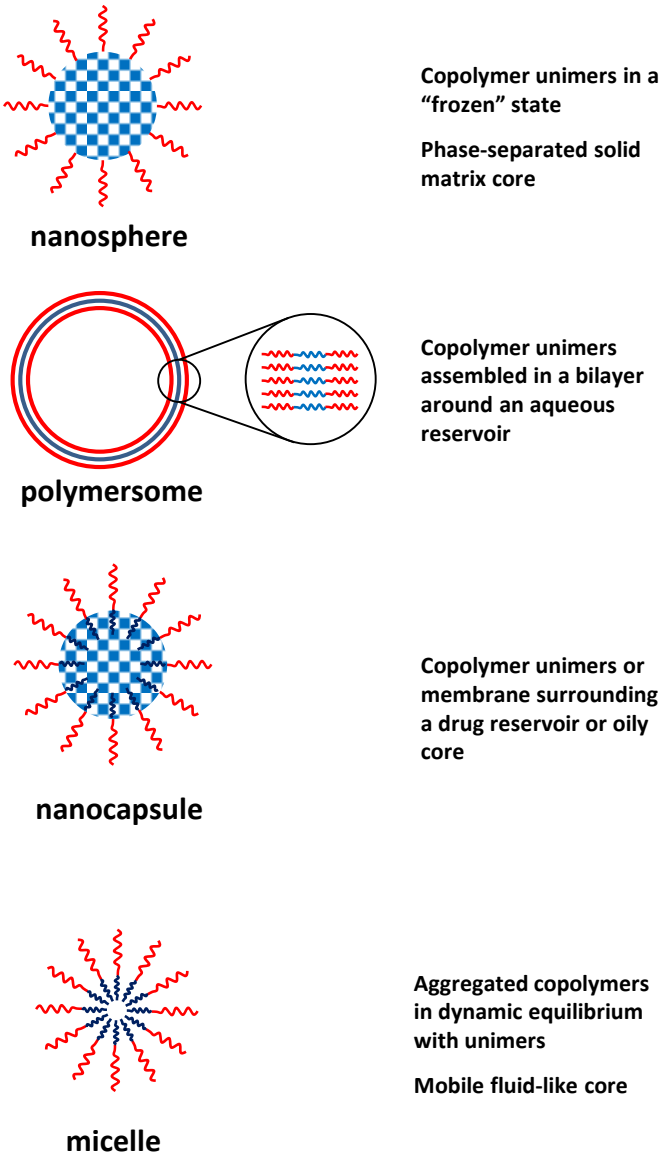

Figure 1.1. Different polymeric nanoparticles and their general characteristics. Adapted from (22).

Polymeric nanospheres are solid colloidal particles in which the polymer establishes a uniform matrix like in a frozen state, and can be prepared using different methods, including emulsion polymerization (23), emulsion/solvent evaporation or diffusion (24), salting out techniques (25) and nanoprecipitation (26). In nanospheres, which frequently present a hydrophobic surface, drugs can be either entrapped-in or adsorbed-on the polymer matrix. One subtype of polymeric nanospheres is single

chain polymeric nanoparticles (SCPNs), which production is based on the controlled compaction of single polymer coils into unimolecular soft nano-objects. Single chain polymeric nanoparticles, which have been assayed as drug carriers in the context of this PhD thesis, can be made of synthetic polymers, benefiting thus from the possibility of a controlled construction of the precursors in order to tune the size and functionality of the final particles (27), as well as from biocompatible, non-toxic and ready-to-use natural polymers. Synthetic routes to SCPN are mainly based on intra-chain homo- and hetero-coupling or crosslinker-induced collapse of pre-functionalized polymers through covalent, dynamic covalent, and non-covalent bonding (28). Most covalent strategies require organic solvents and the reactions need to be carried out using highly diluted polymer solutions, at high temperatures and/or in the presence of metal catalysts, although this can be mitigated e.g. by using polymers with side-chain functionalities like oligo(ethylene glycol) (OEG) brushes which prevent intermolecular cross-linking (29). Recently, the group of Dr. Loinaz, co-director of this PhD thesis, has reported strategies to generate SCPN (30-32), and hence SCPNs have been also assayed (see Chapter 5).

Polymersomes are vesicular nanosystems in which the core consists of an aqueous phase and the surrounding coating is a bilayer formed by an amphiphilic block copolymer. The vesicular structure is similar to the cellular membrane, in which the hydrophobic tails of the polymer or the lipid are oriented towards each other while the heads are in contact with the aqueous phases, both in the core and in the surrounding environment (33). Polymersomes are suitable for the encapsulation and subsequent delivery of water soluble drugs in the aqueous core, and are prepared using the so-called film rehydration technique (34).

Nanocapsules are similar to polymersomes with some differences, mainly: (i) the nature of the core, which in the case of nanocapsules is an oily phase, and (ii) in the surrounding polymer, which is not a bilayer but a single layer (35). Nanocapsules are useful for encapsulation of hydrophobic drugs, thus enhancing their bioavailability. The methods for the production of nanocapsules include interfacial deposition and solvent displacement (36, 37).

Micelles are formed by amphiphilc polymers brought into contact with an aqueous solution. At the critical micelle concentration (CMC), the amphiphilic moieties self-assemble into nano- or micro-sized particles, in which the hydrophilic portion is oriented towards water and the hydrophobic part is oriented towards the inner core of the particle. The inner core, which is integrated by the hydrophobic regions, is able to host small lipophilic drugs. Polymeric micelles can be constructed by using both biocompatible synthetic polymers and natural macromolecules, thus combining the processability and adaptability of the first with the ability of the latter to program assemblage mechanisms and control the structure and function (38). Several polymers have been used to achieve effective steric stabilization of micelles.

Poly ethylene glycol (PEG) is widely chosen as shell-forming segment for developing polymeric micelles because of its hydrophilicity, linearity, chain flexibility, lack of charge, and availability in a wide range of molecular weights (MWs) with narrow MW distribution, facilitating the preparation of narrowly distributed block copolymers capable to assemble monodisperse polymeric micelles with low polydispersity index (PDI). Additionally, the end-groups of PEG can be controlled to prepare block copolymers or branched polymers, or even to attach ligand molecules (e.g. targeting moieties). Typically, PEGs with 1−20 kDa are used for constructing self-assembled nanostructures (39). Besides PEG, other polymers have been applied as shell-forming segments for the preparation of polymeric micelles, including poly(N-vinyl-2-pyrrolidone) (PVP) (40), poly(vinyl alcohol) (PVA) (41), and poly(acrylamide) (PAAm) (42), among others.

The composition of the core-forming segment is essential for the stabilization of the micelle and eventually the drug cargo. For constructing cores containing hydrophobic drugs, the most commonly used polymers are polyethers (43, 44), polyesters (45, 46), and polyamino acids (38). For a recent review regarding the preparation and applications of polymeric micelles, please refer to (47). Polymeric micelles are the second type of carrier that has been used in the context of this PhD thesis. More information about the preparation method and properties is included in chapter 5.

1.1.4. NPs in Nanomedicine: Oncology

Nanoparticle formulations are being deeply investigated in the field of biomedicine, mainly as therapeutic agents in oncology; this is due to three factors: (1) their size, which enables preferential accumulation in the tumour tissue (see below); (2) their high surface-to-volume ratio, which enables multi-functionalization; and (3) the possibility to load a high amount of cargo, which turns NPs into ideal drug carriers. It is commonly accepted that NPs preferentially accumulate in tumour tissue due to the well-known enhanced permeability and retention (EPR) effect (48). This effect is based on the presence of leaky vasculature in the vicinity of tumours, whose endothelium is fenestrated with gaps between 100 nm and 780 nm in size. This, together with a deficient lymphatic drainage, results in a passive accumulation of NPs in tumour tissue (see Figure 1.2a). Such accumulation can be even improved by attaching targeting moieties to the surface of the NPs, with high affinity for specific receptors over-expressed in tumour cells but not in the surrounding healthy tissue. Because multiple targeting moieties can be attached to each individual NP, multiple interactions with the receptors present at the cell surface lead to improved retention and, eventually, internalization of the NP (49-51).

This said, it is important to remark that both EPR effect and the concept of targeted nanomedicine in oncology are often overrated and/or misinterpreted. The EPR effect is indeed a highly heterogeneous phenomenon, which varies substantially from tumour model to tumour model, from patient to patient and also from one region to another within the same tumour (52). Hence, extravasation of the nanomedicines will follow a heterogeneous pattern. Additionally, nanomedicines find different barriers during extravasation, including pericyte-, smooth muscle cell- and fibroblast-based cell layers between endothelial and tumour cells. Once the NPs succeed in leaving the blood vessels, the extravasated NPs need to penetrate the interstitium to reach cancer cells. Due to their large size (when compared to small-molecule drugs) their penetration is hampered due to the high cell density usually found in tumours together with the high interstitial fluid pressure (Fig 1.2b).

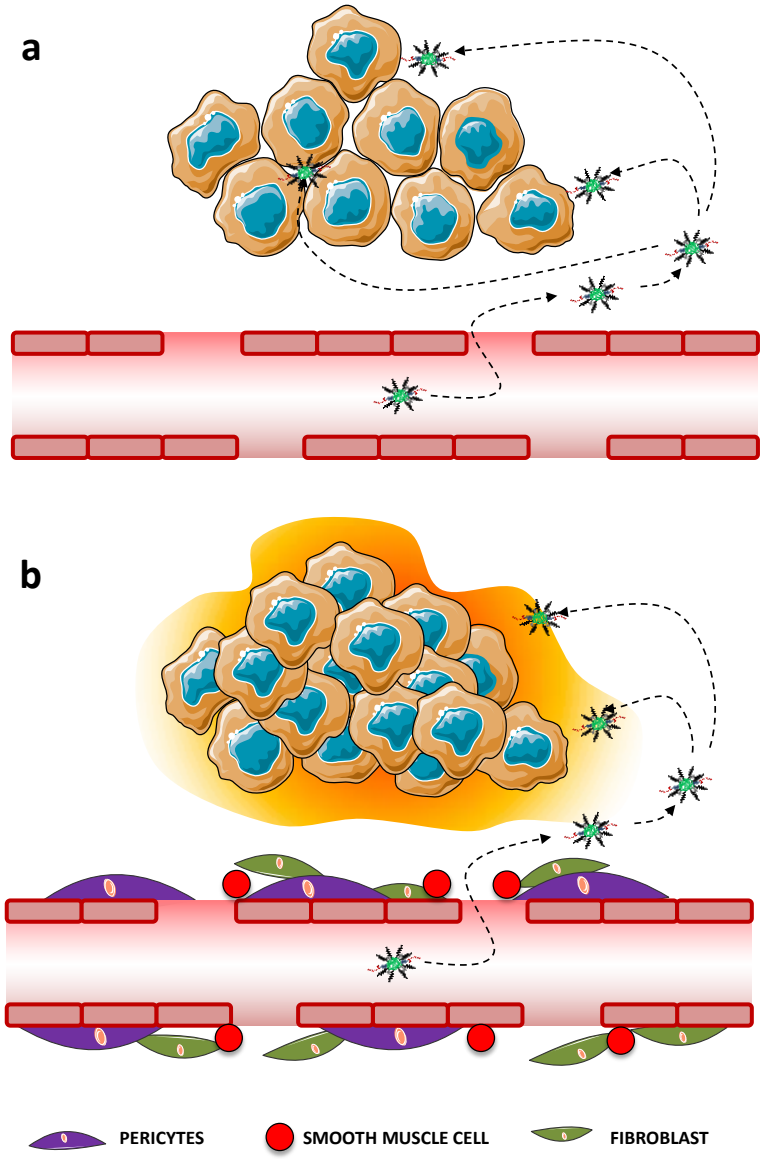

Figure 1.2. (a) Schematic representation of an idealized passive accumulation of NPs in tumours by EPR effect. Tumours possess leaky blood vessels than allow extravasation of NPs, which can reach tumour cells; (b) realistic model: NPs need to cross pericyte-, smooth muscle- and fibroblast-based cell layers before they are able to bind to cancer cells. Once there, high cell density and interstitial fluid pressure need to be overcome before the NPs reach tumour cells.

As a consequence of the above mentioned issues, incorporating targeting ligands in nanomedicine formulations is less useful than expected *a priori* (53). Indeed, the primary mode of tumour accumulation relies on EPR-mediated passive extravasation. After leaving tumour blood vessels and penetrating into the interstitium, NPs can find tumour cells and bind to them. Only at this stage the presence of the targeting moiety can contribute to enhance cell uptake. Hence, incorporation of targeting moieties to

improve accumulation in the target tissue or organ only makes sense in a limited number of specific cases, whereas in other cases, it just complicates and increases the cost of the formulation. For example, it has been shown that HER2-antibody targeted nanosystems do not increase tumour concentrations as compared to passively targeted formulations (54), although alterations on the local distribution of the agents within tumours was observed together with a higher degree of cell internalisation.

1.1.5. NPs in Nanomedicine: Bacterial respiratory infection

Besides the classical and widely explored (and exploited) application in oncology, the use of nanomedicines is also gaining attention in other therapeutic areas, and one of these is for the treatment of **bacterial respiratory infections**, which predominate over viral infections in secondary and tertiary care (55). Although effective antimicrobial treatments are available, pathogenic bacteria continue to demonstrate their ability to adapt to different types of antimicrobial compounds, increasing thus antibiotic resistance (56), while relatively few new candidate antibiotics reach the market. In view of this, global authorities are investing money by focusing on several key 'One Health' action areas, which include the development of new antibiotics and treatment strategies, among other actions.

Together with the development of new, more potent antibiotics, such as antimicrobial peptides (AMPs) (57), some emphasis has been made in the administration route. Intravenous and/or oral administration usually results in a low accumulation of the drug in the target organ or tissue, and consequently in a high accumulation in non-targeted organs. This, ultimately, may result in undesired toxicity (58) together with enhanced selection of antibiotic-resistant bacteria residing in the endogenous microbiota, so-called collateral damage (59). To overcome this problem, local administration of the antibiotics has been considered, especially when the lung is the target organ as it is the case in bacterial respiratory infections. The accurate delivery of antibiotics into the lungs would allow the antibiotics to reach higher local concentrations, avoid ‘first-pass’ metabolism and reduce the toxic side-effects associated with systemic administration (60). However, for the majority of antibiotics,

direct lung administration results in a short residence time of the antibiotic in the lungs due to pulmonary clearance, enzymatic/chemical degradation and rapid adsorption. These drawbacks could be overcome by using appropriate nanocarriers to deliver the antibiotics, resulting in: (i) an increase in the drug concentration in the target organ at a lower dose; (ii) Protection of the antibiotic from enzymatic/chemical degradation; and (iii) protection of the antibiotic from pulmonary clearance mechanisms. Eventually, controlled released of the drug could be even achieved.

In principle, a wide variety of nanocarriers could potentially be utilized to enhance the deposition of antibiotics to lung (61). However, the choice of the nanocarrier is restricted by the architecture of the respiratory tract and biological clearance mechanisms; it is commonly accepted that, when targeting the lower airways, nanomedicines with an aerodynamic diameter of 1–5 µm are deposited efficiently (62), which means that micron-size agglomerated nanomedicines or aerosols are currently mainly used for the pulmonary delivery of nanomedicines (63, 64).

1.2. Tracing NPs *in vivo*: nuclear imaging techniques

1.2.1. The need for tracking

Nanomedicines need to fulfil certain prerequisites which include good biocompatibility, sufficient blood residence time to reach the target (when intravenously administered), efficient clearance from the body, and high accumulation in the target organs as well as low accumulation in off-target sites to minimize side effects. This, together with a good understanding of the pharmacokinetics and the biological fate of the nanomedicine and its integral parts, this is, the nanocarrier and the drug itself, is paramount to safely and efficiently tackle therapeutic experiments in the clinical arena with an appropriate selection of the dosing regimen.

One particularly problematic aspect in the study of the biological fate of nanoformulations is that they are extremely difficult to detect and quantify once distributed in a material or biological system. One alternative to overcome this problem consists of labelling the nanoformulation with radioisotopes which allow their

detection with high sensitivity and in a non-invasive fashion by using molecular imaging techniques such as single-photon emission computed tomography (SPECT) and positron emission tomography (PET). Both techniques are non-invasive and fully translational and enable the evaluation of pharmacokinetics both in the preclinical and clinical fields (65-72).

1.2.2. Nuclear imaging: general aspects

Nuclear imaging techniques rely on the administration of trace amount of a compound that is labelled with a positron or gamma-emitting radionuclide. When a positron or gamma-emitter disintegrates, gamma rays are ultimately generated. These gamma rays (or high energy photons) can be detected by specific equipment in such way that the original concentration of the compound can be accurately quantified. In this manner, as long as the radioisotope remains bound to the compound, the biodistribution of the latter within a living organism can be assessed. In other words, nuclear imaging techniques enable the absolute quantification of the concentration of a radionuclide (or the compound labelled with the radionuclide) over time, *in vivo*, non-invasively and with high sensitivity.

1.2.3. Radioactive isotopes

In general, there are two different types of radioisotopes which are commonly used in nuclear imaging: gamma emitters and positron emitters. These radioisotopes differ in their route of decay (Figure 1.3); single-photon emitters decay by emitting gamma rays which generally have energies in the range of 100-300 keV. On the other hand, the positron is the antiparticle of the electron, with equivalent mass but positive electrical charge. When a positron emitter disintegrates by spontaneous radioactive decay, the positron is emitted. During its short lifetime, the positron interacts with other charged particles and progressively loses its kinetic energy while describing a random path. When most of its energy has been lost, the positron annihilates with an electron of a surrounding atom, resulting in the emission of a pair of gamma rays traveling 180° apart and with energies of 511 keV each. The linear distance between the locations

where the disintegration and the annihilation occur is called positron range and is typically of a few millimetres in water.

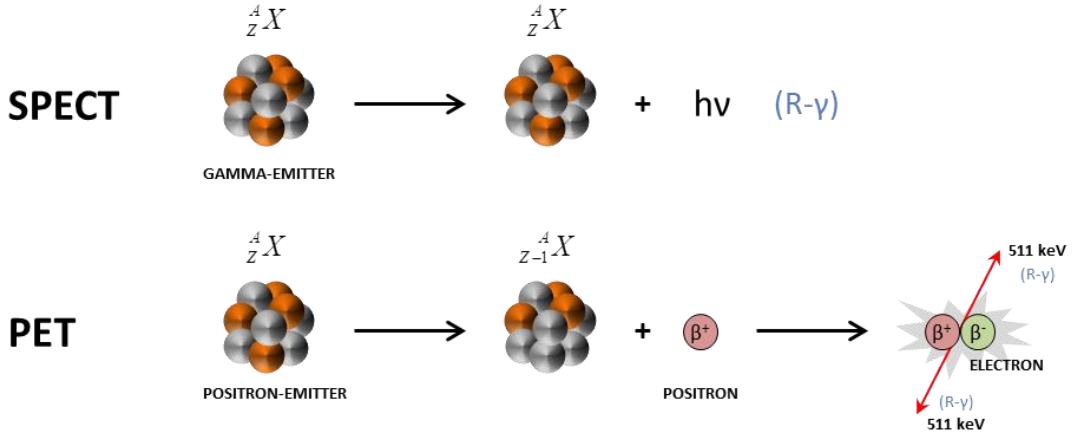

Figure 1.3. Schematic representation of radioactive decay by gamma (top) and positron (bottom) emission.

Gamma and positron-emitters have different physical properties, the most notable being the half-life ($T_{1/2}$). The half-life of a radioisotope is defined as the period of time required to decrease the number of radioactive atoms to one half of the starting value. In general, most single-photon emitter radioisotopes present longer half-lives (from a few hours to days; see table 1.1) compared to positron emitters (from a few minutes to hours; see table 1.2). The selection of a radionuclide with an appropriate half-life is paramount to guarantee successful *in vivo* studies. In general, the physical half-life of the radionuclide should match the biological half-life of the molecule to be investigated. If the physical half-life is too short, only partial information about the pharmacokinetics will be obtained. If the half-life is too long, a high (and unnecessary) radiation dose will be imposed on the subject under investigation. The latter is especially relevant in clinical studies.

Table 1.1: Typical single photon emitters (with half-life and energy)

Isotope	Half-life	γ Energy (γ Fraction)
^{99m}Tc	6.02 h	141 keV (89%)
^{123}I	13.22 d	159 keV (83%)
^{111}In	2.80 h	171 (91%), 245 keV (94%)
^{67}Ga	3.26 d	93 (39%), 185 (21%), 300 (17%), 394 keV (5%)
^{131}I	8.02 d	364 keV (82%)

Table 1.2: Typical positron emitters (with half-life and energy)

Isotope	Half-life	β^+ Energy$_{max}$ (β^+ Fraction)*
^{18}F	109.8 min	0.63 MeV (0.97)
^{11}C	20.4 min	0.96 MeV (1.00)
^{13}N	9.97 min	1.20 MeV (1.00)
^{15}O	122 seg	1.73 MeV (1.00)
^{68}Ga	67.6 min	1.89 MeV (0.89)

* The positrons are not emitted with a unique energy. The energies of the positrons emitted by a radionuclide follow a Poisson distribution. The maximum value of the distribution is presented in the table.

1.2.4. Gamma-ray detection

In order to obtain information about the regional concentration of the labelled molecule after administration into a living organism, it is necessary to detect the gamma-rays emitted as a result of the disintegration process and to determine the direction of such gamma rays. Hence, many angular views (projections) need to be acquired to feed mathematical reconstruction algorithms in order to obtain tomographic datasets. This technique is also known as emission CT (ECT) which should not be confused with standard X-ray transmission CT in which the X-ray source is external to the specimen.

As mentioned above, both PET and SPECT rely on the detection of gamma rays originated during radioactive decay of gamma and positron emitting radionuclides, respectively. However, due to their different physical characteristics, SPECT and PET scanners' detection system is different. SPECT scanners typically consist of at least one gamma ray detection module and a collimator. The core of the detection module is normally a scintillation crystal which, when excited by a gamma ray, absorbs its energy and re-emits it in the form of a flash light, typically in the ultraviolet range. This flash is subsequently detected by a photo-electronic system which records its location in the crystal and its intensity, which is proportional to the energy of the incidental gamma-ray. The collimator most commonly consists of a lead plate which has a large number of holes to stop all the rays that do not reach the detector in a given direction. Hence, the collimator forms a projected image of the radioisotope distribution on the surface

of the scintillation crystal. SPECT systems are typically composed of one or more detection heads which are set up in a gantry that rotates around the imaged subject (Figure 1.4a). If only one static detection head is used, the technique is referred to as planar scintigraphy.

In PET, the imaging strategy needs back-to-back detection heads and coincidence detection circuitry. Typically, PET scanners consist of a stationary array of a full-ring of detectors which simultaneously detect both gamma rays resulting from the positron-electron annihilation. This kind of detection system is known as "electronic" collimation as opposed to the "physical" collimation implemented in SPECT scanners. A schematic representation of a PET scanner is shown in Figure 1.4b.

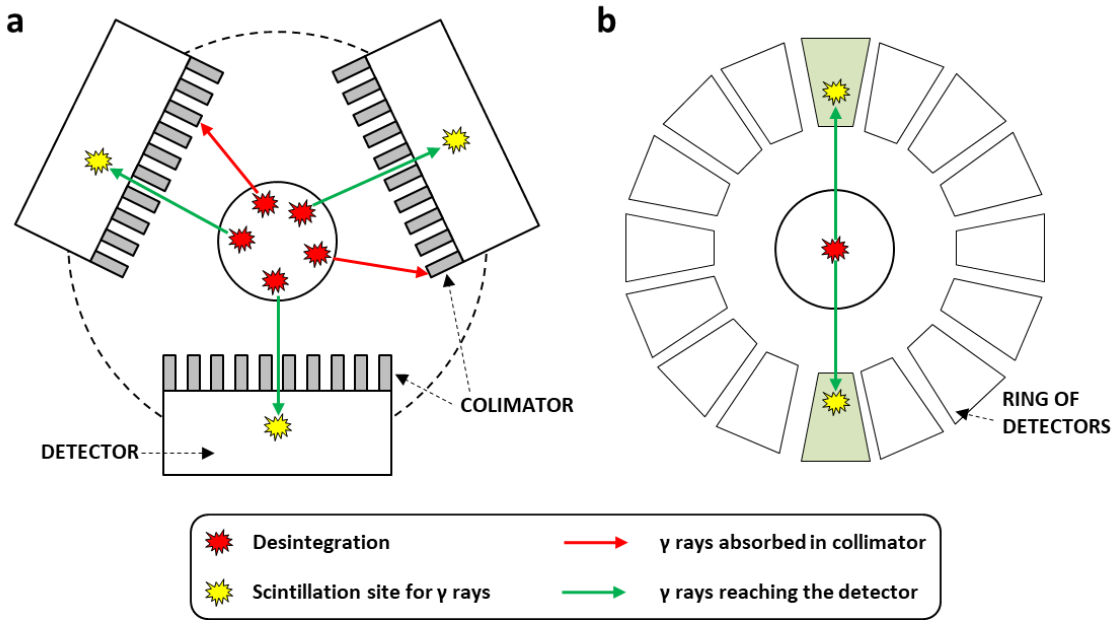

Figure 1.4. Schematic representation of the detection of photons using SPECT (a) and PET (b) scanners.

The physical collimation implemented in SPECT scanners hampers the detection of a large fraction of the gamma-rays emitted and, as a consequence, the absolute sensitivity (the ratio of detected to actual desintegrations) is much lower than in PET. Since the signal-to-noise ratio of the obtained data is proportional to the square root of the number of events detected, this has an enormous impact on the image quality,

as well as on the ability to acquire shorter scans to achieve improved temporal resolution and acquire multiple fields of view for whole body imaging.

Both PET and SPECT systems acquire a set of projections at different angular positions around the specimen being imaged. Reconstruction tomography makes use of computers and mathematical algorithms to determine the unknown distribution of the radiotracer in the body from the detected projection data. The mathematical principles of image reconstruction fall beyond the scope of this PhD thesis. From a user's perspective, reconstruction algorithms can be split into analytical methods, and most notably the Filtered Back Projection (FBP) algorithm; and the iterative statistical reconstruction method such as Ordered Subset Expectation Maximization (OSEM) and its many variants. Usually, iterative reconstruction methods provide images with improved spatial resolution and better signal-to-noise ratios at the expense of increased computational time and some unpredictability in the final outcome. For an extensive review about reconstruction methods, the reader is referred to (73-75).

1.2.5. The key step: Radiolabelling

Radiolabelling is a key step in the application of nuclear imaging techniques to the *in vivo* investigation of drugs and nanomedicines. So far, a huge number of strategies to incorporate both positron and gamma emitters to a wide range of molecular modalities (from small molecules to peptides, proteins, antibodies and NPs) have been developed. Here, only the most commonly used methodologies for the radiolabelling of NPs, together with the strategies commonly employed for the radiolabelling of peptides will be covered. For detailed reviews, the reader is referred to (76-78).

1.2.5.1. Radiolabelling of NPs

As mentioned in the previous sections, there is a large variety of NPs, and different radiolabelling strategies have been developed (79). However, they can be summarized in 2 main categories:

The first category collects all the strategies that rely on the in situ generation of the radioisotope by activation of the NPs. This is usually achieved by irradiation with high-

energy particles, i.e. ions (protons or deuterons) or neutrons. The high energetic reaction of the incident particle with a stable atom of the NP results in a nuclear reaction, which may lead to the formation of a radionuclide suitable for imaging studies. Some examples include the activation of Al_2O_3 NPs by proton irradiation *via* the $^{16}O(p,\alpha)^{13}N$ nuclear reaction (80), the activation of CeO_2 NPs by deuteron irradiation *via* the $^{140}Ce(d, p)^{141}Ce$ nuclear reaction (81), and neutron activation of ^{197}Au NPs to generate *in situ* ^{198}Au-labelled NPs (82). While the application of proton and deuteron activation is limited to NPs in the solid state and can result in thermal damage of the irradiated material, neutron irradiation can be conducted in solution, allowing the activation of nanoparticles or nanoparticle suspensions that are sensitive to thermal damage or radiation exposure (83). However, it is required that the NP to be activated contains a stable atom with a high capacity to interact with thermal neutrons. This property is limited to gold and a few more elements. As a consequence, direct activation is not usually applied to the activation of NPs with biomedical applications. Indeed, its use has been more restricted to the activation of metal and metal oxide NPs in toxicity studies.

The second strategy is known as after-loading, and relies on the attachment or entrapment of the radionuclide once the NP has been synthesized. This is usually achieved using bifunctional chelators (BFCs), which contain one functional group and a metal binding moiety function. The functional group allows for anchoring the BFC to the surface of the NP, while the latter enables the sequestration of a metallic radionuclide. This strategy has been successfully applied to the preparation of NPs labelled with different positron and gamma emitters, including ^{64}Cu, ^{68}Ga and ^{99m}Tc (84-86). This methodology has one clear advantage: The NP can be designed to already contain the BFC and be submitted to full characterisation. The chelation reaction (for the formation of the radiometal-chelator complex) usually takes place under mild conditions, and hence it is expected not to significantly alter the NPs properties. Alternatively to the use of BFCs, the attachment of pre-labelled tags to the NP surface (69), attachment of radioactive ions (87) as well as diffusion of radioactive species into the NPs (88) have also been reported. In the particular case of liposomes, transport of

the radionuclide through the lipid bilayer using a hydrophobic complex and subsequent sequestration of the radionuclide in the inner aqueous phase has been commonly used (89, 90).

As mentioned above, the second strategy (afterloading) is the most widely used in biomedicine, because the fact that the radionuclide can be incorporated in a very late stage in the synthetic process and the relatively mild reaction conditions required are definite advantages. In this PhD thesis, the labelling of polymeric NPs has been approached by formation of a radiometal-chelator complex, as discussed in detail in Chapter 5.

1.2.5.2. Radiolabelling of peptides

Radiolabelling of peptides has been typically approached by following two different strategies. The first strategy, commonly applied in classical nuclear medicine, relies in the attachment of a BFC to the peptide and subsequent incubation with a radiometal to form the corresponding complex (91). The second strategy is based on radioiodination, mainly using two different synthetic routes. The first one relies on the *in situ* oxidation of the anionic species (I^-) using an oxidizing agent in solution, e.g. *N*-chloro tosylamide or chloramine-T (92). This species subsequently undergoes electrophilic aromatic substitution (SEAr) reactions on aromatic rings containing electron-donating groups, this is, on tyrosine residues (which bear a hydroxyl group). This method results in high yields and has been widely applied to the radiolabelling of proteins and peptides. To prevent the degradation of the peptide/protein, milder oxidizing agents have been developed, such as 1,3,4,6-tetrachloro-3α,6α-diphenyl glycoluril (Iodogen) (93). The second labelling strategy is based on an indirect method, by covalent attachment of a pre-labelled prosthetic group, being the most commonly used the Bolton–Hunter reagent (94) which readily reacts with primary amines to form the corresponding amides.

Besides radioiodination and BFC-radiometal complex formation, the attachment of pre-labelled tags using click chemistry approaches has recently gained attention (95, 96) .

The AMPs evaluated in the context of the current PhD thesis were designed to contain at least one tyrosine residue. Because of this, the direct iodination method was employed (see Chapter 5 for details about experimental procedures).

1.3. References

1. Burton PD, Boyle TJ, Datye AK. Facile, surfactant-free synthesis of Pd nanoparticles for heterogeneous catalysts. *Journal of Catalysis*. **2011**;280(2):145-9.

2. Blasco C, Picó Y. Determining nanomaterials in food. *TrAC - Trends in Analytical Chemistry*. **2011**;30(1):84-99.

3. Stroyuk AL, Shvalagin VV, Kuchmii SY. Photochemical synthesis and optical properties of binary and ternary metal-semiconductor composites based on zinc oxide nanoparticles. *Journal of Photochemistry and Photobiology A: Chemistry*. **2005**;173(2):185-94.

4. Labille J, Feng J, Botta C, Borschneck D, Sammut M, Cabie M, et al. Aging of TiO_2 nanocomposites used in sunscreen. Dispersion and fate of the degradation products in aqueous environment. *Environmental Pollution*. **2010**;158(12):3482-9.

5. Janib SM, Moses AS, MacKay JA. Imaging and drug delivery using theranostic nanoparticles. *Advanced Drug Delivery Reviews*. **2010**;62(11):1052-63.

6. Shenoy DB, Amiji MM. Poly(ethylene oxide)-modified poly(epsilon-caprolactone) nanoparticles for targeted delivery of tamoxifen in breast cancer. *International journal of pharmaceutics*. **2005**;293(1-2):261-70.

7. Chan JM, Valencia PM, Zhang L, Langer R, Farokhzad OC. Polymeric nanoparticles for drug delivery. *Methods in Molecular Biology*. **2010**;624:163-75.

8. Sahoo SK, Labhasetwar V. Nanotech approaches to drug delivery and imaging. *Drug Discovery Today*. **2003**;8(24):1112-20.

9. Hawker CJ, Wooley KL. The convergence of synthetic organic and polymer chemistries. *Science*. **2005**;309(5738):1200-5.

10. Panyam J, Labhasetwar V. Biodegradable nanoparticles for drug and gene delivery to cells and tissue. *Advanced Drug Delivery Reviews*. **2003**;55(3):329-47.

11. Muthu MS. Nanoparticles based on PLGA and its co-polymer: An overview. *Asian Journal of Pharmaceutics*. **2009**;3(4):266-73.

12. Locatelli E, Franchini MC. Biodegradable PLGA-b-PEG polymeric nanoparticles: Synthesis, properties, and nanomedical applications as drug delivery system. *Journal of Nanoparticle Research*. **2012**;14(12).

13. Lele BS, Leroux JC. Synthesis and micellar characterization of novel amphiphilic A-B-A triblock copolymers of N-(2-hydroxypropyl)methacrylamide or N-vinyl-2-pyrrolidone with poly(ε-caprolactone). *Macromolecules*. **2002**;35(17):6714-23.

14. Letchford K, Zastre J, Liggins R, Burt H. Synthesis and micellar characterization of short block length methoxy poly(ethylene glycol)-block-poly(caprolactone) diblock copolymers. *Colloids and Surfaces B: Biointerfaces*. **2004**;35(2):81-91.

15. Shu S, Sun L, Zhang X, Wu Z, Wang Z, Li C. Polysaccharides-based polyelectrolyte nanoparticles as protein drugs delivery system. *Journal of Nanoparticle Research*. **2011**;13(9):3657-70.

16. Sun G, Mao JJ. Engineering dextran-based scaffolds for drug delivery and tissue repair. *Nanomedicine*. **2012**;7(11):1771-84.

17. Ahsan SM, Thomas M, Reddy KK, Sooraparaju SG, Asthana A, Bhatnagar I. Chitosan as biomaterial in drug delivery and tissue engineering. *International Journal of Biological Macromolecules*. **2018**;110:97-109.

18. Guarino V, Caputo T, Altobelli R, Ambrosio L. Degradation properties and metabolic activity of alginate and chitosan polyelectrolytes for drug delivery and tissue engineering applications. *AIMS Materials Science*. **2015**;2(4):497-502.

19. Dang JM, Leong KW. Natural polymers for gene delivery and tissue engineering. *Advanced Drug Delivery Reviews*. **2006**;58(4):487-99.

20. Baabur-Cohen H, Omer L, Satchi-Fainaro R. Recent progress in polymer therapeutics as nanomedicines. Handbook of Harnessing Biomaterials in Nanomedicine: Pan Stanford Publishing Pte. Ltd.; 2012. p. 77-122.

21. Duncan R. Polymer therapeutics as nanomedicines: New perspectives. *Current Opinion in Biotechnology*. **2011**;22(4):492-501.

22. Letchford K, Burt H. A review of the formation and classification of amphiphilic block copolymer nanoparticulate structures: micelles, nanospheres, nanocapsules and polymersomes. *European Journal of Pharmaceutics and Biopharmaceutics*. **2007**;65(3):259-69.

23. Zhang W, D'Agosto F, Boyron O, Rieger J, Charleux B. Toward a better understanding of the parameters that lead to the formation of nonspherical polystyrene particles via RAFT-mediated one-pot aqueous emulsion polymerization. *Macromolecules*. **2012**;45(10):4075-84.

24. Jelvehgari M, Barar J, Valizadeh H, Shadrou S, Nokhodchi A. Formulation, characterization and in vitro evaluation of theophylline-loaded Eudragit RS 100 microspheres prepared by an emulsion-solvent diffusion/evaporation technique. *Pharmaceutical Development and Technology*. **2011**;16(6):637-44.

25. Mendoza-Muñoz N, Quintanar-Guerrero D, Allémann E. The impact of the salting-out technique on the preparation of colloidal particulate systems for pharmaceutical applications. *Recent Patents on Drug Delivery and Formulation*. **2012**;6(3):236-49.

26. Chin SF, Pang SC, Tay SH. Size controlled synthesis of starch nanoparticles by a simple nanoprecipitation method. *Carbohydrate Polymers*. **2011**;86(4):1817-9.

27. Hanlon AM, Lyon CK, Berda EB. What Is Next in Single-Chain Nanoparticles? *Macromolecules*. **2016**;49(1):2-14.

28. Lyon CK, Prasher A, Hanlon AM, Tuten BT, Tooley CA, Frank PG, et al. A brief user's guide to single-chain nanoparticles. *Polymer Chemistry*. **2015**;6(2):181-97.

29. Wong EHH, Lam SJ, Nam E, Qiao GG. Biocompatible single-chain polymeric nanoparticles via organo-catalyzed ring-opening polymerization. *ACS Macro Letters*. **2014**;3(6):524-8.

30. Aiertza MK, Sánchez L, Benito AB, Loinaz I, Cabañero G, Grande HJ, et al., inventors; FUNDACIÓN CIDETEC, assignee. A process for preparing water-dispersible single-chain polymeric nanoparticles. United States2017.

31. Benito AB, Aiertza MK, Marradi M, Gil-Iceta L, Shekhter Zahavi T, Szczupak B, et al. Functional Single-Chain Polymer Nanoparticles: Targeting and Imaging Pancreatic Tumors in Vivo. *Biomacromolecules*. **2016**;17(10):3213-21.

32. Gracia R, Marradi M, Cossío U, Benito A, Pérez-San Vicente A, Gómez-Vallejo V, et al. Synthesis and functionalization of dextran-based single-chain nanoparticles in aqueous media. *Journal of Materials Chemistry B*. **2017**;5(6):1143-7.

33. Chandrawati R, Caruso F. Biomimetic liposome- and polymersome-based multicompartmentalized assemblies. *Langmuir*. **2012**;28(39):13798-807.

34. Lee James CM, Bermudez H, Discher BM, Sheehan MA, Won YY, Bates FS, et al. Preparation, stability, and in vitro performance of vesicles made with diblock copolymers. *Biotechnol Bioeng*. **2001**;73(2):135-45.

35. Mora-Huertas CE, Fessi H, Elaissari A. Polymer-based nanocapsules for drug delivery. *International journal of pharmaceutics*. **2010**;385(1-2):113-42.

36. Fessi H, Puisieux F, Devissaguet JP, Ammoury N, Benita S. Nanocapsule formation by interfacial polymer deposition following solvent displacement. *International journal of pharmaceutics*. **1989**;55(1):R1-R4.

37. Mosqueira VCF, Legrand P, Pinto-Alphandary H, Puisieux F, Barratt G. Poly(D,L-Lactide) nanocapsules prepared by a solvent displacement process: Influence of the composition on physicochemical and structural properties. *Journal of Pharmaceutical Sciences*. **2000**;89(5):614-26.

38. Kataoka K, Harada A, Nagasaki Y. Block copolymer micelles for drug delivery: Design, characterization and biological significance. *Advanced Drug Delivery Reviews*. **2012**;64(SUPPL.):37-48.

39. Knop K, Hoogenboom R, Fischer D, Schubert US. Poly(ethylene glycol) in drug delivery: Pros and cons as well as potential alternatives. *Angewandte Chemie - International Edition*. **2010**;49(36):6288-308.

40. Torchilin VP, Trubetskoy VS. Which polymers can make nanoparticulate drug carriers long-circulating? *Advanced Drug Delivery Reviews*. **1995**;16(2-3):141-55.

41. Takeuchi H, Kojima H, Yamamoto H, Kawashima Y. Evaluation of circulation profiles of liposomes coated with hydrophilic polymers having different molecular weights in rats. *Journal of Controlled Release*. **2001**;75(1-2):83-91.

42. Torchilin VP, Shtilman MI, Trubetskoy VS, Whiteman K, Milstein AM. Amphiphilic vinyl polymers effectively prolong liposome circulation time in vivo. *BBA - Biomembranes*. **1994**;1195(1):181-4.

43. Kabanov AV, Chekhonin VP, Alakhov VY, Batrakova EV, Lebedev AS, Melik-Nubarov NS, et al. The neuroleptic activity of haloperidol increases after its solubilization in surfactant micelles. Micelles as microcontainers for drug targeting. *FEBS Letters*. **1989**;258(2):343-5.

44. Elsabahy M, Perron MÉ, Bertrand N, Yu GE, Leroux JC. Solubilization of docetaxel in poly(ethylene oxide)-block-poly(butylene/styrene oxide) micelles. *Biomacromolecules*. **2007**;8(7):2250-7.

45. Ikada Y, Tsuji H. Biodegradable polyesters for medical and ecological applications. *Macromolecular Rapid Communications*. **2000**;21(3):117-32.

46. Gaucher G, Marchessault RH, Leroux JC. Polyester-based micelles and nanoparticles for the parenteral delivery of taxanes. *Journal of Controlled Release*. **2010**;143(1):2-12.

47. Cabral H, Miyata K, Osada K, Kataoka K. Block Copolymer Micelles in Nanomedicine Applications. *Chemical Reviews*. **2018**;118(14):6844-92.

48. Maeda H, Matsumura Y. EPR effect based drug design and clinical outlook for enhanced cancer chemotherapy. *Advanced Drug Delivery Reviews*. **2011**;63(3):129-30.

49. Kaltsas GA, Papadogias D, Makras P, Grossman AB. Treatment of advanced neuroendocrine tumours with radiolabelled somatostatin analogues. *Endocrine-Related Cancer*. **2005**;12(4):683-99.

50. Wang M, Thanou M. Targeting nanoparticles to cancer. *Pharmacological Research*. **2010**;62(2):90-9.

51. Alexis F, Pridgen E, Molnar LK, Farokhzad OC. Factors affecting the clearance and biodistribution of polymeric nanoparticles. *Molecular Pharmaceutics*. **2008**;5(4):505-15.

52. Bae YH, Park K. Targeted drug delivery to tumors: myths, reality and possibility. *Journal of Controlled Release*. **2011**;153(3):198-205.

53. Rizzo LY, Theek B, Storm G, Kiessling F, Lammers T. Recent progress in nanomedicine: Therapeutic, diagnostic and theranostic applications. *Current Opinion in Biotechnology*. **2013**;24(6):1159-66.

54. Kirpotin DB, Drummond DC, Shao Y, Shalaby MR, Hong K, Nielsen UB, et al. Antibody targeting of long-circulating lipidic nanoparticles does not increase tumor localization but does increase internalization in animal models. *Cancer research*. **2006**;66(13):6732-40.

55. McCullers JA. Insights into the interaction between influenza virus and pneumococcus. *Clinical Microbiology Reviews*. **2006**;19(3):571-82.

56. Davies J, Davies D. Origins and evolution of antibiotic resistance. *Microbiology and Molecular Biology Reviews*. **2010**;74(3):417-33.

57. Gordon YJ, Romanowski EG, McDermott AM. Mini review: A review of antimicrobial peptides and their therapeutic potential as anti-infective drugs. *Current Eye Research*. **2005**;30(7):505-15.

58. Falagas ME, Kasiakou SK. Toxicity of polymyxins: A systematic review of the evidence from old and recent studies. *Critical Care*. **2006**;10(1).

59. Paterson DL. "Collateral damage" from cephalosporin or quinolone antibiotic therapy. *Clinical Infectious Diseases*. **2004**;38(SUPPL. 4):S341-S5.

60. Patton JS, Byron PR. Inhaling medicines: Delivering drugs to the body through the lungs. *Nature Reviews Drug Discovery*. **2007**;6(1):67-74.

61. Mansour HM, Rhee YS, Wu X. Nanomedicine in pulmonary delivery. *International journal of nanomedicine*. **2009**;4:299-319.

62. Heyder J, Gebhart J, Rudolf G, Schiller CF, Stahlhofen W. Deposition of particles in the human respiratory tract in the size range 0.005-15 μm. *Journal of Aerosol Science*. **1986**;17(5):811-25.

63. Bohr A, Water J, Beck-Broichsitter M, Yang M. Nanoembedded microparticles for stabilization and delivery of drug-loaded nanoparticles. *Current Pharmaceutical Design*. **2015**;21(40):5829-44.

64. Mangal S, Gao W, Li T, Zhou QT. Pulmonary delivery of nanoparticle chemotherapy for the treatment of lung cancers: Challenges and opportunities. *Acta Pharmacologica Sinica*. **2017**;38(6):782-97.

65. Chrastina A, Schnitzer JE. Iodine-125 radiolabeling of silver nanoparticles for in vivo SPECT imaging. *International Journal of Nanomedicine*. **2010**;5(1):653-9.

66. Devaraj NK, Keliher EJ, Thurber GM, Nahrendorf M, Weissleder R. ^{18}F labeled nanoparticles for in Vivo PET-CT imaging. *Bioconjugate Chemistry*. **2009**;20(2):397-401.

67. Guerrero S, Herance JR, Rojas S, Mena JF, Gispert JD, Acosta GA, et al. Synthesis and in vivo evaluation of the biodistribution of a ^{18}F-labeled conjugate gold-nanoparticle-peptide with potential biomedical application. *Bioconjugate Chemistry*. **2012**;23(3):399-408.

68. Pressly ED, Rossin R, Hagooly A, Fukukawa KI, Messmore BW, Welch MJ, et al. Structural effects on the biodistribution and positron emission tomograpgy (PET) imaging of well-defined ^{64}Cu-labeled nanoparticles comprised of amphiphilic block graft copolymers. *Biomacromolecules*. **2007**;8(10):3126-34.

69. Rojas S, Gispert JD, Martín R, Abad S, Menchón C, Pareto D, et al. Biodistribution of amino-functionalized diamond nanoparticles. in vivo studies based on ^{18}F radionuclide emission. *ACS Nano*. **2011**;5(7):5552-9.

70. Schluep T, Hwang J, Hildebrandt IJ, Czernin J, Choi CHJ, Alabi CA, et al. Pharmacokinetics and tumor dynamics of the nanoparticle IT-101 from PET imaging and tumor histological measurements. *Proceedings of the National Academy of Sciences of the United States of America*. **2009**;106(27):11394-9.

71. Zhang Y, Sun Y, Xu X, Zhang X, Zhu H, Huang L, et al. Synthesis, biodistribution, and microsingle photon emission computed tomography (SPECT) imaging study of technetium-99m labeled PEGylated dendrimer poly(amidoamine) (PAMAM)-folic acid conjugates. *Journal of Medicinal Chemistry*. **2010**;53(8):3262-72.

72. Rojas S, Gispert JD, Abad S, Buaki-Sogo M, Victor VM, Garcia H, et al. In vivo biodistribution of amino-functionalized ceria nanoparticles in rats using positron emission tomography. *Molecular Pharmaceutics*. **2012**;9(12):3543-50.

73. Tong S, Alessio AM, Kinahan PE. Image reconstruction for PET/CT scanners: Past achievements and future challenges. *Imaging in Medicine*. **2010**;2(5):529-45.

74. Defrise M, Gullberg GT. Image reconstruction. *Physics in Medicine and Biology*. **2006**;51(13):R139-R54.

75. Zoccarato O. Innovative reconstruction algorithms in cardiac SPECT scintigraphy. *Quarterly Journal of Nuclear Medicine and Molecular Imaging*. **2012**;56(3):230-46.

76. Boschi S, Lodi F. Chemistry of PET Radiopharmaceuticals: Labelling Strategies. Basic Science of PET Imaging: Springer, Cham; 2017. p. 79-103.

77. Chen X, Lang L. PET chemistry. In: Xiaoyuan C, editor. Molecular Imaging Probes for Cancer Research: World Scientific Publishing Company; 2012. p. 151-64.

78. Dilworth JR, Pascu SI. The Radiopharmaceutical Chemistry of Gallium(III) and Indium(III) for SPECT Imaging. In: Nicholas L, Wing-Tak W, editors. The Chemistry of Molecular Imaging: John Wiley & Sons, Inc; 2014. p. 165-78.

79. Roig JL, Gómez-Vallejo V, Gibson PN. Isotopes in nanoparticles: Fundamentals and applications: Pan Stanford; 2016. 1-521 p.

80. Pérez-Campaña C, Gómez-Vallejo V, Puigivila M, Martín A, Calvo-Fernández T, Moya SE, et al. Biodistribution of different sized nanoparticles assessed by positron emission tomography: A general strategy for direct activation of metal oxide particles. *ACS Nano*. **2013**;7(4):3498-505.

81. Simonelli F, Marmorato P, Abbas K, Ponti J, Kozempel J, Holzwarth U, et al. Cyclotron production of radioactive CeO_2 nanoparticles and their application for in vitro uptake studies. *IEEE Transactions on Nanobioscience*. **2011**;10(1):44-50.

82. Lipka J, Semmler-Behnke M, Sperling RA, Wenk A, Takenaka S, Schleh C, et al. Biodistribution of PEG-modified gold nanoparticles following intratracheal instillation and intravenous injection. *Biomaterials*. **2010**;31(25):6574-81.

83. Hamoudeh M, Fessi H, Mehier H, Faraj AA, Canet-Soulas E. Dirhenium decacarbonyl-loaded PLLA nanoparticles: Influence of neutron irradiation and preliminary in vivo administration by the TMT technique. *International journal of pharmaceutics*. **2008**;348(1-2):125-36.

84. Rossin R, Muro S, Welch MJ, Muzykantov VR, Schustery DP. In vivo imaging of ^{64}Cu-labeled polymer nanoparticles targeted to the lung endothelium. *Journal of Nuclear Medicine*. **2008**;49(1):103-11.

85. Locatelli E, Gil L, Israel LL, Passoni L, Naddaka M, Pucci A, et al. Biocompatible nanocomposite for PET/MRI hybrid imaging. *International journal of nanomedicine*. **2012**;7:6021-33.

86. De Souza Albernaz M, Ospina CA, Rossi AM, Santos-Oliveira R. Radiolabelled nanohydroxyapatite with 99mTc: Perspectives to nanoradiopharmaceuticals construction. *Artificial Cells, Nanomedicine and Biotechnology*. **2014**;42(2):88-91.

87. Jauregui-Osoro M, Williamson PA, Glaria A, Sunassee K, Charoenphun P, Green MA, et al. Biocompatible inorganic nanoparticles for [^{18}F]-fluoride binding with applications in PET imaging. *Dalton Transactions*. **2011**;40(23):6226-37.

88. Hildebrand H, Franke K. A new radiolabeling method for commercial Ag^0 nanopowder with ^{110m}Ag for sensitive nanoparticle detection in complex media. *Journal of Nanoparticle Research*. **2012**;14(10).

89. Van Der Geest T, Laverman P, Gerrits D, Franssen GM, Metselaar JM, Storm G, et al. Comparison of three remote radiolabelling methods for long-circulating liposomes. *Journal of Controlled Release*. **2015**;220:239-44.

90. Laverman P, Boerman OC, Oyen WJG, Dams ETM, Storm G, Corstens FHM. Liposomes for scintigraphic detection of infection and inflammation. *Advanced Drug Delivery Reviews*. **1999**;37(1-3):225-35.

91. Tornesello AL, Tornesello ML, Buonaguro FM. An overview of bioactive peptides for in Vivo imaging and therapy in human diseases. *Mini-Reviews in Medicinal Chemistry*. **2017**;17(9):758-70.

92. Hunter WM, Greenwood FC. Preparation of iodine-131 labelled human growth hormone of high specific activity. *Nature*. **1962**;194(4827):495-6.

93. Fraker PJ, Speck Jr JC. Protein and cell membrane iodinations with a sparingly soluble chloroamide, 1,3,4,6-tetrachloro-3a,6a-diphenylglycoluril. *Biochemical and Biophysical Research Communications*. **1978**;80(4):849-57.

94. Bolton AE, Hunter WM. The labelling of proteins to high specific radioactivities by conjugation to a ^{125}I containing acylating agent. Application to the radioimmunoassay. *Biochemical Journal*. **1973**;133(3):529-38.

95. Krishnan HS, Ma L, Vasdev N, Liang SH. ^{18}F-Labeling of Sensitive Biomolecules for Positron Emission Tomography. *Chemistry - A European Journal*. **2017**;23(62):15553-77.

96. Meyer JP, Adumeau P, Lewis JS, Zeglis BM. Click Chemistry and Radiochemistry: The First 10 Years. *Bioconjugate Chemistry*. **2016**;27(12):2791-807.

Chapter 2. Motivation and objectives of the thesis

2.1. Justification of the study: The PneumoNP Project

As mentioned in Chapter 1, the majority of international stakeholders from the healthcare sector agree that infections due to antibiotic resistant Gram-negative bacteria are one of the major issues currently affecting global health, largely due to a lack of effective antibiotic therapy for this type of infection. Global authorities such as the European Union (EU), the World Health Organization (WHO) as well as the United Nations (UN) are aware of this problem and are investing money in trying to solve the worldwide endemic of antibiotic resistance by focusing on several key 'One Health' action areas. In this context, the EU Commission launched a call in 2013 encouraging the development of novel nanotherapeutics to treat bacterial infectious diseases.

One of the projects selected for funding in this call was the PneumoNP project, a collaborative work funded by the European Commission under the FP7-NMP-2013-LARGE-7 call (No. 604434 grant). The aim of the project was to develop a therapeutic system for the treatment of lung Gram-negative bacterial infections, based on the combination of an antimicrobial peptide (AMP) and a nanocarrier (NC) to yield the resulting nanomedicine (or nanosystem, NS), and focusing the attention on *Klebsiella pneumoniae* caused infections for proof of concept experiments. In parallel, the project aimed at developing a new nebulization system for the administration of aerosols in experimental animals and the validation of a diagnostic kit.

The consortium as a whole included 11 partners from 6 member states (Spain, Germany, Italy, France, The Netherlands and Denmark) coming from different scientific and technological disciplines. Two of the partners, namely Setlance srl (SET, Italy) and Adenium Biotech (ADE, Denmark) were devoted to the development of novel AMPs. Two of the partners, CIDETEC (CID, Spain) and Utrecht University (UU, The Netherlands), were devoted to the preparation of nanocarriers and the development of strategies for the formation of the nanosystems. One of the partners, Ingeniatrics Tecnologías (INGEN, Spain), was in charge of developing the new nebulizer for the

administration of the aerosols to rodents. Finally, Pathofinder BV (PAT, Germany) and Erasmus Medical Centre (EMC, The Netherlands) were in charge of developing the diagnostic kit and performing *in vivo* proof of efficacy studies with selected NSs in relevant animal models, respectively.

In this large project, The Radiochemistry and Nuclear Imaging Group at CIC biomaGUNE, in which this PhD has been conducted, had two major roles: (i) To evaluate the novel nebulization system developed by INGEN in comparison with commercially available systems; and (ii) to assess the biodistribution and basic pharmacokinetic properties of the nanosystems developed in the context of the project. As initially planned in the project proposal, evaluation should be conducted using nuclear imaging techniques, opportunistically in combination with other imaging modalities such as computerised tomography (CT).

The piece of work included in this PhD comprises three parts, which constitute the three experimental chapters (chapters 3-5).

In the first part of the work (chapter 3), a new tool for the assessment of lung ventilation using Positron Emission Tomography (PET) has been developed and evaluated in wild type animals (rats). This task was not formally included in the PneumoNP project description and the results have not been used in the context of the PneumoNP project. However, it is considered as an essential tool for future works. Indeed, evaluation of the biodistribution or determination of pharmacokinetic properties of new chemical/biological entities after lung administration requires previous evidence of unaltered ventilation, and this can be assessed efficiently and with high sensitivity with the newly developed tool. Hence, this work, which was published in *Chemical Communications* (1) and is included in Chapter 3 of this PhD thesis, will be paramount for future studies tackling lung diseases carried out at CIC biomaGUNE.

The second part of the work, included in Chapter 4 of this PhD thesis, describes the evaluation of the new nebulization system developed by partner INGEN and its comparison towards two different commercially available systems. In the preclinical

context, in which experimental animals are used, the evaluation of innovative lung-administered therapeutics requires administration of the drug in the form of aerosol or dry powder. Different technologies have been developed and tested, and none of them is ideal. Additionally, there is little information regarding the capacity of the different administration systems to release the drug in the lungs and the uniformity of the deposition. Hence, in this chapter, and by using a straightforward methodology to radiolabel the aerosol, the system developed by INGEN was evaluated in terms of uniformity of deposition of the aerosol in the lungs and the percentage of the aerosol that is actually released in the target organ. Both parameters are essential when planning therapeutic experiments. The performance of the new system was compared to an endotracheal insufflator and a commercially available nebulizer. This work was published in the *European Journal of Pharmaceutics and Biopharmaceutics* scientific journal (2), and the results were very useful in the selection of the administration system to be used in therapeutic experiments (carried out by partner EMC) and to establish the dose to be nebulised.

In the third part of the work, which constitutes chapter 5 of the current PhD thesis, the residence time in the lungs of AMPs developed by partners SET and ADE after lung administration was investigated, both as free peptides and in combination with the nanocarriers, which were provided by partners UU and CID. With that aim, radiolabelling strategies to incorporate either positron or gamma emitters into the different species were developed, and imaging studies were conducted to determine the residence time in the lungs of the labelled AMPs and, eventually, of the nanocarriers. These studies provided clear information about the advantages of using nanocarriers as drug delivery systems for nanomedicines targeting the lungs, and the results were used in therapeutic experiments carried out at EMC. The work related to the radiolabelling of the AMPs and the radiolabelling of the NPs has been published in part in two different papers, in the journals *Scientific Reports* and *Journal of Materials Chemistry B*, respectively (3, 4). The manuscripts collecting other parts of the work developed in this chapter are currently under preparation.

2.2. Objectives

The specific objectives of this PhD thesis are

1. To develop an imaging tool for the quantitative assessment of lung ventilation in experimental animals using Positron Emission Tomography.
2. To evaluate three different systems for the administration of aerosols to small rodents, in terms of: (i) Uniformity of the deposition within the lungs; and (ii) percentage of aerosol deposited in the lungs.
3. To develop labelling strategies for the incorporation of positron emitters in selected antimicrobial peptides.
4. To determine the residence time in the lungs of radiolabelled antimicrobial peptides, either administered as "free peptides" or combined with selected nanocarriers, after aerosol administration.
5. To develop labelling strategies for the incorporation of gamma emitters in selected nanocarriers and evaluate their residence time in the lungs after aerosol administration.

2.3. References

1. Gómez-Vallejo V, Lekuona A, Baz Z, Szczupak B, Cossío U, Llop J. Ion beam induced ^{18}F-radiofluorination: Straightforward synthesis of gaseous radiotracers for the assessment of regional lung ventilation using positron emission tomography. *Chemical Communications*. **2016**;52(80):11931-4.

2. Cossío U, Gómez-Vallejo V, Flores M, Gañán-Calvo B, Jurado G, Llop J. Preclinical evaluation of aerosol administration systems using Positron Emission Tomography. *European Journal of Pharmaceutics and Biopharmaceutics*. **2018**;130:59-65.

3. Gracia R, Marradi M, Cossío U, Benito A, Pérez-San Vicente A, Gómez-Vallejo V, et al. Synthesis and functionalization of dextran-based single-chain nanoparticles in aqueous media. *Journal of Materials Chemistry B*. **2017**;5(6):1143-7.

4. Brunetti J, Falciani C, Roscia G, Pollini S, Bindi S, Scali S, et al. In vitro and in vivo efficacy, toxicity, bio-distribution and resistance selection of a novel antibacterial drug candidate. *Scientific Reports*. **2016**;6.

Chapter 3. Development of novel tracers for the assessment of lung ventilation using Positron Emission Tomography

3.1. Introduction

As mentioned in previous chapters, pulmonary administration of drugs is extremely attractive, especially when the lung is the portal organ. However, in a real clinical scenario, the distribution of the drug over the whole lung relies on proper ventilation. Areas with impaired ventilation may result in low regional deposition, while hyperventilated areas may lead to local overexposure. In this scenario, it seems appropriate to evaluate, previously to the administration of the drug, the regional lung ventilation in order to identify those areas that may be submitted to under- or over-exposure.

In the clinical setting, the most accessible and economic tool to evaluate lung ventilation is spirometry, which provides information regarding the amount (volume) and/or speed (flow) of air that can be inhaled and exhaled. However, this routinely used function test is relatively insensitive to subtle changes and does not provide any regional information. Contrary to spirometry, *in vivo* medical imaging techniques have the potential to provide regional information in a non-invasive way. Unfortunately, the perfect imaging tool to quantitatively evaluate regional lung ventilation with high sensitivity and on real time has not been developed.

One of the most convenient imaging techniques to assess regional lung ventilation is magnetic resonance imaging (MRI). This high-resolution technique uses the intrinsic signals generated from the underlying proton (^{1}H) signal in tissues. Due to the low water content in the lung, MRI-lung imaging has severe limitations in terms of sensitivity. However, this limitation can be overcome by using exogenous contrast agents. For example, hyperpolarized (hP) gas MRI using the stable gaseous isotope helium-3 (^{3}He) in combination with conventional MRI has offered hope to evaluate, noninvasively and with high sensitivity and excellent spatial resolution, the regional lung function together with structural integrity (1). For example, ventilation MRI

studies in humans using hP ^{3}He allowed the visualization of ventilation defects in healthy volunteers, patients with asthma and lung-transplanted patients (Figure 3.1) together with the anatomical information of the lung structures (2). Unfortunately, the high cost and limited supply of ^{3}He gas limit the dissemination of this technology (3).

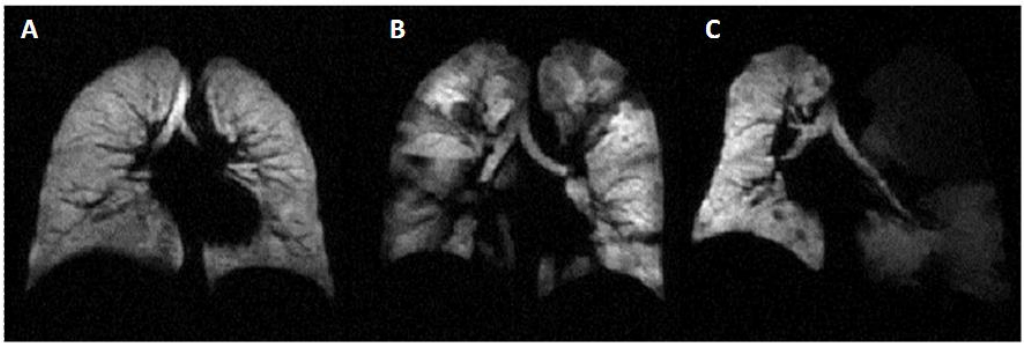

Figure 3.1. Static ^{3}He gas density images from (A) a healthy volunteer, (B) a patient with asthma and (C) a lung-transplant recipient. The image from the healthy volunteer has a homogeneous signal intensity, while the asthmatic patients' image has multiple "ventilation defects". The image from the lung transplant recipient is homogeneous in transplanted (right) lung, and is markedly hypo-intense in the native emphysematous lung. Image obtained from reference (2).

Alternatively to hP MRI, compounds containing a relatively large number of fluorine (^{19}F, Larmor frequency 59.9 MHz) atoms per molecule can be used as gaseous contrast agents for ventilation ^{19}F-MRI. Inert fluorinated gases, such as tetrafluoromethane (CF_4), hexafluoroethane (C_2F_6), or sulfur hexafluoride (SF_6), possess a T1 relaxation time of the order of milliseconds. The spin-rotation relaxation of these paramagnetic gases is so fast that the paramagnetism of oxygen has no effect. This short T1 makes rapid repetition radiofrequency pulses feasible. This enables the acquisition of a high number of signals, compensating for the low spin density of the gas (4). As a result, fluorinated gases have proven useful as lung contrast agents with sufficient MRI sensitivity (5). Additionally, availability of multiple litres of gas enables image acquisition during steady-state breathing. Among fluorinated gases, SF_6 has the advantage that it is almost insoluble in blood, has no known toxic effects, is relatively inexpensive, and has been used for many years in clinical trials as part of the multiple inert gas elimination technique.

Despite high resolution images can be obtained with ^{19}F-MRI, one of the main drawbacks arises from the poor intrinsic sensitivity of the technique; because of this, high concentration of contrast agent (in this case, fluorinated gas) needs to be administered. For example, in the first human study reported in the literature (see Figure 3.2) ^{19}F-enhanced acquisitions were carried out following breath of a mixture of 71-78% SF_6 and oxygen (6). No adverse side effects were observed and the subjects tolerated the gas mixture well. However, because of the higher density of the fluorinated gas in comparison with the physiologically inhaled gases (O_2, N_2, CO_2), transfer of data under normal ventilation conditions might be critical when compared with breathing ambient air.

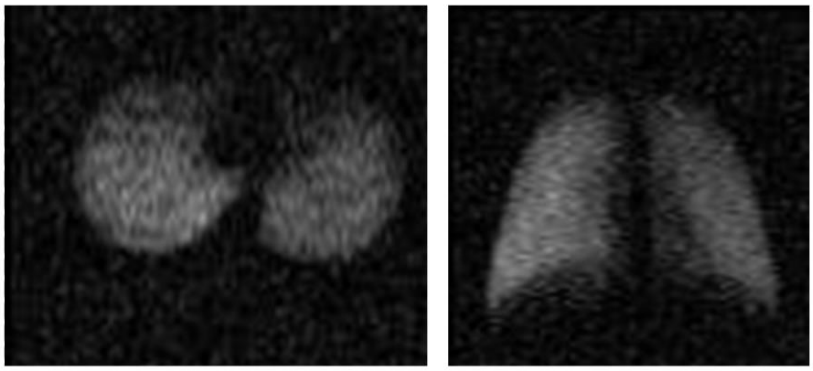

Figure 3.2. Left: Transverse image of a human lung after 3 breaths of 71% SF_6. Right: coronal image of a human lung after 5 breaths of 78% SF_6. Image obtained from reference (6).

The limitations of MRI can be easily overcome by using more sensitive imaging modalities, such as nuclear imaging techniques, i.e. planar scintigraphy, single photon emission computerized tomography (SPECT) or positron emission tomography (PET). In nuclear imaging experiments, only trace amounts of the radioactive contrast agent (radiotracer) are required to provide enough signal-to-noise ratio. Additionally, absolute quantification of the distribution of the radiotracer after administration is feasible, especially in PET.

In the clinical arena, lung ventilation is mainly performed with single photon emission computerized tomography (SPECT) or planar scintigraphy, using as contrast agents gases such as ^{81m}Kr (7) and more often radiolabelled aerosols generated either from

water-soluble agents ([^{99m}Tc]DTPA) (8) or solid particles (Technegas, or *in situ* generated ^{99m}Tc-labelled graphite particles) (9). After inhalation, ^{81m}Kr is distributed according to regional ventilation without any local accumulation on airway walls. However, limited access, short half-life ($T_{1/2}$ = 13 s) and high cost restrict its use. Liquid radio-aerosols, and to a lower extent Technegas, show central airway deposition and peripheral "hotspot" formation in patients with obstructive lung diseases. Moreover, SPECT has limitations in terms of sensitivity, spatiotemporal resolution and image quantification.

The higher sensitivity and quantitative nature of PET may result in a valuable alternative to other nuclear imaging modalities to assess lung ventilation. Compared to SPECT, PET offers much higher sensitivity and better spatial resolution (10). Taking advantage of these features, several methods have been developed to measure ventilation with PET. A continuous inhalation of ^{19}Ne gas can be used to estimate regional ventilation (11). Due to the low solubility in water, its distribution volume is essentially that of the ventilated lung. A PET scan obtained when the distribution of ^{19}Ne is at equilibrium represents a balance between the amount of activity inhaled per unit time, its clearance by alveolar ventilation and radioactive decay. Alveolar ventilation can be thus calculated after determination of regional alveolar volume from regional density measurements (e.g., using CT). Alternatively, ventilation studies using ^{13}N[N_2] gas have also been reported (12). Unfortunately, the short half-life of Neon-19 ($T_{1/2}$=17.4 s) and Nitrogen-13 ($T_{1/2}$=9.97 min) restricts the application of these methodologies to those facilities equipped with a cyclotron and a radiopharmaceutical laboratory able to produce the radiolabelled gases.

In this scenario, the development of inert, water insoluble, non-toxic gas labelled with a long-lived positron emitter would enable the preparation of the radiotracer in centralized production centres. Further distribution to surrounding hospitals equipped with a PET camera, in a similar fashion to ^{18}F-labelled fluorodeoxyglucose ([^{18}F]Fluoro-2-deoxy-2-D-glucose or [^{18}F]FDG), a radiotracer which is currently produced in the gigabecquerel (GBq) scale in many centres worldwide and utilized in the clinical setting

for the early diagnose of certain types of cancer and evaluation of response to therapy, can be envisaged.

A suitable candidate for this purpose would be $[^{18}F]SF_6$. As mentioned earlier in this section, SF_6 is almost insoluble in blood and has no known toxic effect. The production of $[^{18}F]SF_6$ might be approached by following a similar strategy to that already reported under non-radioactive conditions (13). Briefly, combustion of sulphur in $[^{18}F]F_2$ (which occurs at room temperature) would lead to the formation of a mixture of gases containing $[^{18}F]SF_6$ and small concentrations of lower fluorides, such as $[^{18}F]S_2F_2$ and $[^{18}F]S_2F_{10}$. Subsequent purification comprising thermal decomposition of $[^{18}F]S_5F_{10}$ at 400°C, by which procedure the tetrafluoride and hexafluoride are formed, thorough washing and alkali scrubbing to remove hydrogen fluoride and the hydrolysable lower fluorides of sulphur would probably yield pure $[^{18}F]SF_6$. Although this methodology looks feasible from a radiochemical point of view, it can be anticipated to be experimentally challenging and time-consuming.

In this thesis, we envisioned the preparation of radiolabelled $[^{18}F]SF_6$ and also $[^{18}F]CF_4$ relying on a completely innovative methodology: radiotracer production within the cyclotron target, inspired by the method currently used for the in-cyclotron production of $[^{18}F]F_2$, which relies on the $^{18}O(p,n)^{18}F$ nuclear reaction and involves two sequential irradiations ("double shoot method"). In a first step, the target is loaded with pure $[^{18}O]O_2$ and irradiated with protons, to generate ^{18}F (probably as anionic species) which remains absorbed on the walls of the target. The irradiated gas is then removed and the target is refilled with a mixture of F_2 and neon. The second proton irradiation then drives a formal isotopic exchange of the fluorine in the gas with that on the target wall, resulting in the desired $[^{18}F]F_2$ (14, 15). This method can produce several tens of GBq worth of $[^{18}F]F_2$, and is becoming increasingly used worldwide.

Our approach consists of filling the target with mixtures SF_6/Ne or CF_4/Ne (neon as a carrier) before the second irradiation, instead of the mixture F_2/Ne. Our hypothesis relied on the fact that, due to (i) the high temperature and pressure achieved during irradiation; and (ii) the ionizing capacity of incident high-energy protons, isotopic exchange between one of the fluorine atoms in SF_6 (or CF_4) and ^{18}F atoms absorbed on

the target wall may occur, with consequent *in situ* generation of $[^{18}F]SF_6$ (or $[^{18}F]CF_4$, see Figure 3.3).

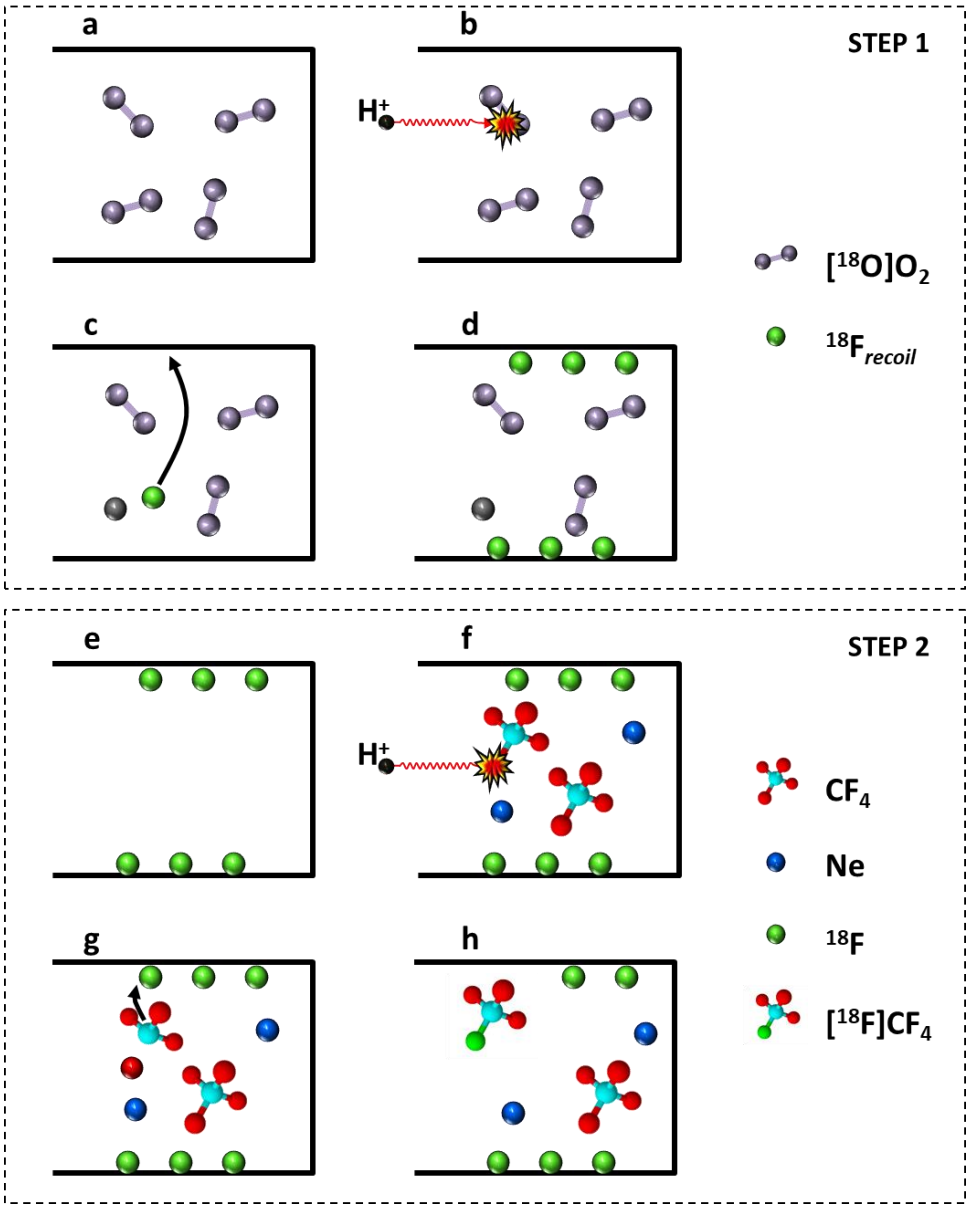

Figure 3.3. Two-step procedure for the production of $[^{18}F]CF_4$. In step 1, $[^{18}O]O_2$ (a) is irradiated with protons (b) to generate ^{18}F ($^{18}O(p,n)^{18}F$ nuclear reaction), which remains absorbed on the target walls (c and d). In step 2, after removal of the $[^{18}O]O_2$ (e), the target is filled with a mixture CF_4/Ne (f). Under proton irradiation (f), ions are generated (g). Under high temperature/pressure, isotopic exchange and consequent formation of $[^{18}F]CF_4$ occurs (h). The parallel reaction pathway can be envisaged for the production of $[^{18}F]SF_6$.

In parallel, a second strategy was also assayed. This was based on the direct irradiation of SF_6/Ne or CF_4/Ne mixtures ("single shot method"). In this approach, the hypothesis

is that the ^{19}F can undergo $^{19}F(p,pn)^{18}F$ nuclear reaction, resulting in the formation of ^{18}F recoil atoms, which may lead to the isotopic exchange reaction with SF_6 or CF_4 molecules to yield the desired labelled gases (see Figure 3.4).

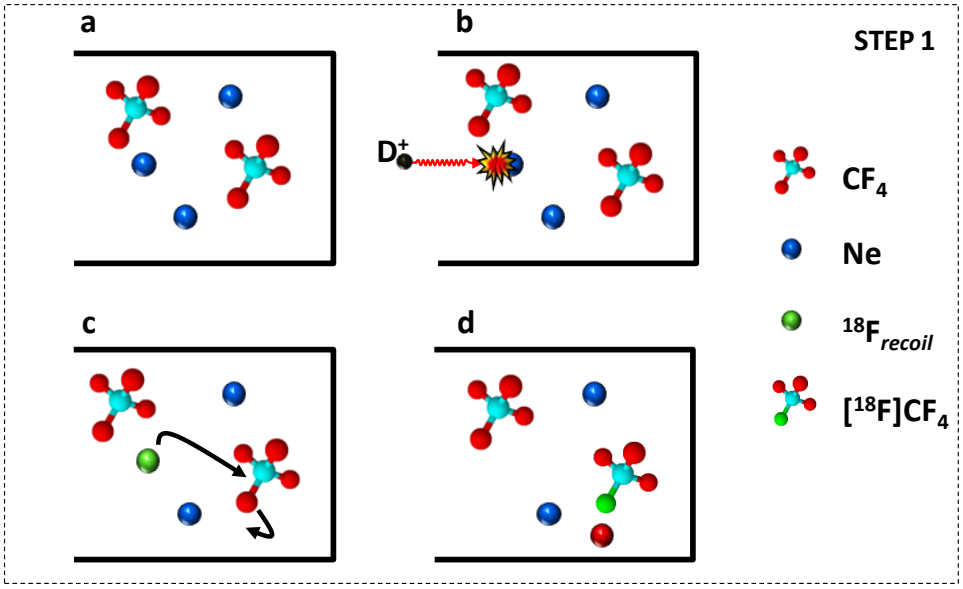

Figure 3.4. One-step procedure for the production of $[^{18}F]CF_4$. The target is filled with a mixture of CF_4 and Neon (a), and is irradiated with protons (b) to generate recoil ^{18}F atoms ($^{19}F(p,pn)^{18}F$ nuclear reaction), which can undergo directly isotopic exchange (c) and consequent formation of $[^{18}F]CF_4$ (d).

The radiolabelled gases proved efficient as ventilation markers in healthy rodents, as demonstrated in our PET studies which showed uniform distribution of the radioactivity in the whole lungs and rapid elimination when the administration was discontinued.

3.2. Objectives

The specific objectives of this work are:

1. To develop a method for the fast, efficient and reliable production of $[^{18}F]CF_4$ and $[^{18}F]SF_6$ by proton irradiation of gas mixtures using the "double shoot method"
2. To evaluate the suitability of the resulting radiofluorinated gases as contrast agents for the non-invasive evaluation of regional lung ventilation.

3.3 Experimental Part

3.3.1 Production and analysis of [^{18}F]CF_4 and [^{18}F]SF_6

Two different strategies were used for the production of [^{18}F]CF_4 and [^{18}F]SF_6. The first strategy (method A) was based on a single irradiation of a mixture CF_4/Ne (production of [^{18}F]CF_4) or SF_6/Ne (production of [^{18}F]SF_6) with 18 MeV protons, using a commercial target for the production of [^{18}F]F_2, consisting of an aluminium target body with an internal volume around 50 mL (see Figure 3.5). Initial assays were carried out with CF_4. The target was first filled with CF_4 to a final pressure (P_1) of 2-4 bar. The target was then topped with Neon to a final pressure of 20 bar and submitted to proton irradiation using a proton intensity of 15 µAh and an integrated current (C_1) in the range 4-8 µAh. After finalising the irradiation, the target gas was transferred by depressurization to the radiochemistry laboratory and collected in a cryogenic trap cooled with liquid nitrogen. This strategy was also applied to the preparation of SF_6. In this case, P_1 was fixed to 4 bar and C_1 was fixed to 4 µAh.

The second strategy (method B) was based in a double shoot method using the same target. The process consisted of four steps: (i) The target was filled with [^{18}O]O_2 (P = 20 bar) and was irradiated with 18 MeV protons using a proton intensity of 15 µAh and an integrated current (C_2) in the range 1-4 µAh; (ii) after irradiation, the target gas was removed by cryogenic retrieval using liquid nitrogen; (iii) the target was filled with CF_4 (or SF_6) to a final pressure of 4 bar, topped with Neon gas to a final pressure = 20 bar and irradiated with 18 MeV protons using a proton intensity of 15 µAh and an integrated current (C_3) in the range 1-4 µAh; (iv) after the second irradiation, the target gas was transferred by depressurization to the radiochemistry laboratory and collected in a cryogenic trap cooled with liquid nitrogen. Parallel experiments were performed by adding a soda-lime trap before the cryogenic trap. For the production of [^{18}F]SF_6, C_1 and C_2 were fixed to 4 µAh. In all cases, the amount of radioactivity collected in the cryogenic trap was measured in a dose calibrator (Capintec CRC®-25 PET, New Jersey, USA). Samples of the radioactive gas were withdrawn with a customized and automated syringe mounted on a syringe driver, and were analysed by gas

chromatography (GC) coupled to mass spectrometry (MS). Analyses were performed using an Agilent 7820A network GC connected to an Agilent 5975c inert XL MSD with triple axis detector. A J&W PoraPlot column (length: 27.5 m, internal diameter: 0.32 mm) was used as stationary phase. The inlet conditions were 150°C, 6.8 psi and a flow rate of 2.5 ml/min. Helium (99.9999%) was used as the carrier gas. The oven temperature was set to 36°C. The analyses were made in scan mode. Eventually, a radioactivity detector (Gabi, Raytest) was connected via a post-column split to identify the radioactive gases.

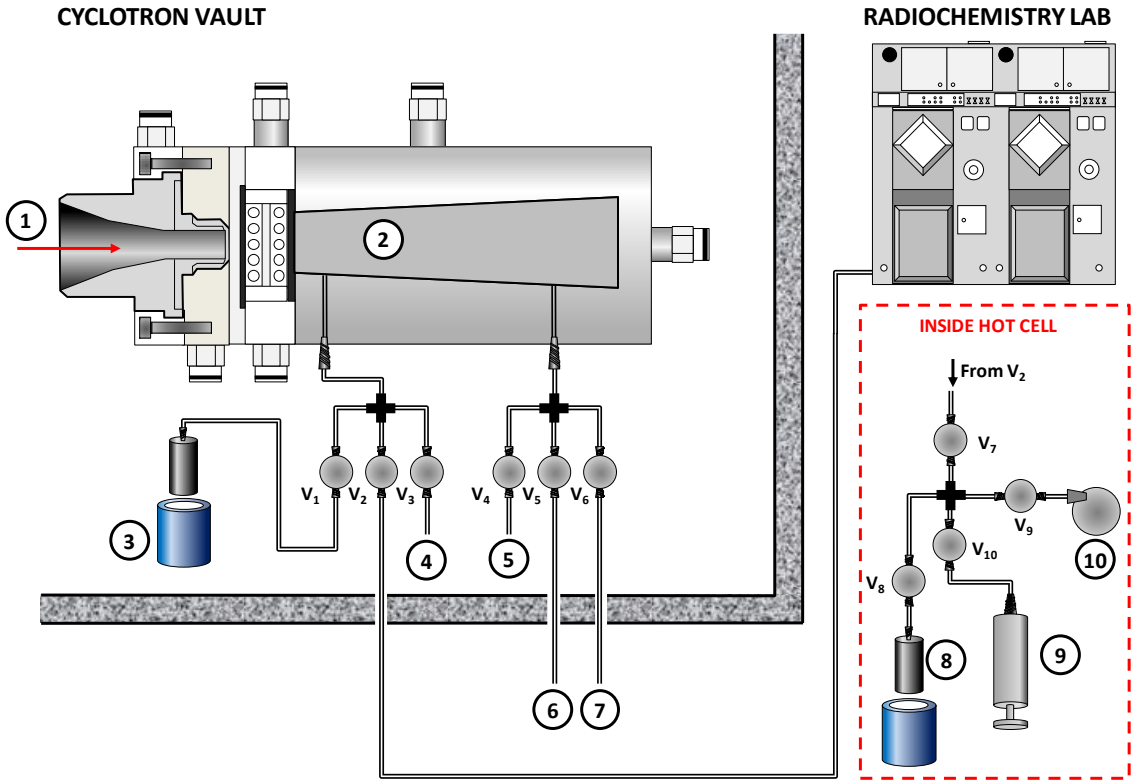

Figure 3.5. Configuration of the target and the recovery system used for the production of [^{18}F]CF_4 using methods A and B; (1) proton beam; (2) target chamber; (3) stainless steel-high pressure container and liquid nitrogen cooling bath; (4) Exhaust; (5) [^{18}O]O_2 gas bottle; (6) Neon gas bottle; (7) CF_4 gas bottle; (8) stainless steel-high pressure container and liquid nitrogen cooling bath; (9) gas-tight syringe mounted on a syringe driver; (10) vacuum pump. V_1-V_{10} are 2-way, normally-closed electro-valves.

3.3.2 Imaging studies

Male rats (n = 2) weighing 350±14 g were used. Animal studies were approved by the ethical committee of CIC biomaGUNE and local authorities, and were conducted in accordance with EU Directives on animal ethics and welfare. Anaesthesia was first induced with 5% isoflurane in 100% O_2. The animals were then moved to the PET/CT scanner (eXplore Vista CT, GE Helthcare) and anaesthesia was maintained with isoflurane in 100% O_2 (1 L/min) administered through a face mask. Breathing frequency was adjusted to 50 ± 10 breaths/minute. The PET acquisition (list mode, 400-700 keV energetic window) was started, and 1 minute later the radioactive gas (74±8 MBq) was introduced in the O_2 main stream (used in the anaesthesia system) over 70 s using a syringe pump (Figure 3.6).

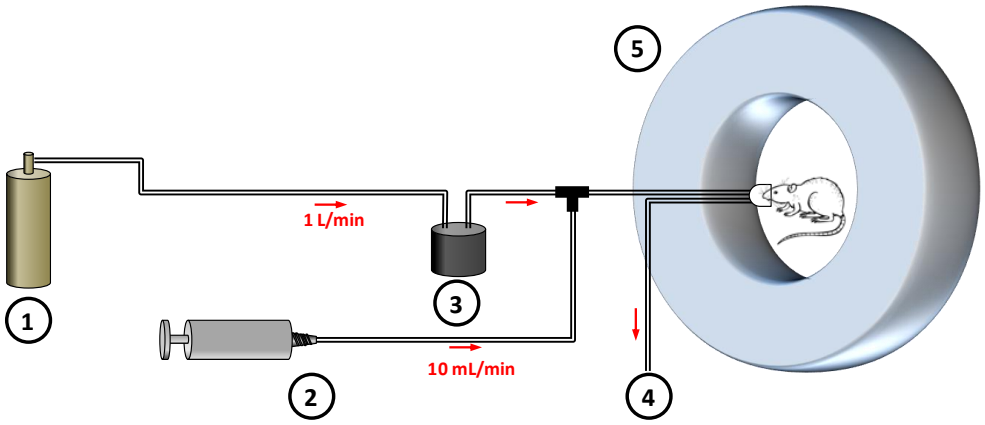

Figure 3.6. Configuration of the administration system utilised to perform PET studies; (1) O_2 gas; (2) gas-tight syringe mounted on a syringe driver, containing the radioactive gas ($[^{18}F]CF_4$ or $[^{18}F]SF_6$); (3) isoflurane vaporizer; (4) exhaust; (5) PET-CT camera.

After the PET scan, a whole-body CT acquisition (140 mA/40kV) was performed. The PET list-mode data were formatted into 19 frames (3x20s, 10x10s, 4x20s and 2x30s) and PET images were reconstructed using the 2D-OSEM algorithm (2 iterations, 16 subsets) into 175x175x61 arrays with a voxel size of 0.3875x0.3875x0.775 mm and were corrected for decay, scatter and random events. The CT images were reconstructed using a cone-beam Feldkamp algorithm into 262x262x688 arrays with a voxel size of 0.246 mm^3. Images were analysed using PMOD image analysis software. Volumes of interest (VOIs) were manually drawn in the lungs on the CT images,

transferred to the PET images and the concentration of the radioactivity was obtained for each time frame. All frames were finally summed in order to obtain more accurate images of the radioactivity distribution within the lungs.

3.4 Results and Discussion

3.4.1. Production and analysis of $[^{18}F]CF_4$ and $[^{18}F]SF_6$

When method A was used to produce $[^{18}F]CF_4$, higher P_1 and C_1 values led to higher activities, with a maximum of 0.80 ± 0.06 GBq for P_1 = 4 bar/C_1 = 8 µAh (Table 3.1). In this first approach (method A), we anticipated that irradiation of CF_4 with protons with an appropriate energy should produce *in situ* recoil ^{18}F atoms *via* the $^{19}F(p,pn)^{18}F$ nuclear reaction, capable to undergo isotopic exchange reaction with surrounding CF_4 molecules to form $[^{18}F]CF_4$. Cross sectional values for the nuclear reaction $^{19}F(p,pn)^{18}F$, which has an energy threshold of approximately 10 MeV and reach a maximum in cross-section values of around 150 mb in the range 20-30 MeV (16), suggest that the limiting step in the production of $[^{18}F]CF_4$ using method A is the generation of the radionuclide, which is limited due to the maximum energy available in our cyclotron (18 MeV). However, as it can be seen in Table 3.1 (entries 1-4), significant amounts of $[^{18}F]CF_4$ could be produced.

When method B was used to produce the same labelled gas, constant C_2 values led to equivalent values of radioactivity, irrespective of C_3 (entries 5-7). However, a clear dependence between C_2 and the final amount of radioactivity could be observed (entries 7 and 8). In this process, during the first irradiation of pure $[^{18}O]O_2$, ^{18}F is generated in high yield, because the cross section values of the nuclear reaction $^{18}O(p,n)^{18}F$ have an energy threshold of around 2 MeV and reach a maximum at energies around 6 MeV (cross section values at this energy around 500 mb) (17). During cryogenic recovery of the ^{18}O-enriched oxygen, Fluorine-18 remains absorbed on the walls of the target chamber, and is ready to undergo isotopic exchange reaction in the following step. Indeed, subsequent irradiation of CF_4/Ne resulted in the formation of $[^{18}F]CF_4$. A clear correlation between the amount of $[^{18}F]CF_4$ and the integrated current used for the first irradiation (entries 7-8, table 3.1) was observed,

suggesting that the formation of Fluorine-18 occurs majorly during the first beam, as expected. Interestingly, the integrated current for the second irradiation had a minor effect on the amount of $[^{18}F]CF_4$, suggesting that the isotopic exchange reaction is relatively fast (see Table 3.1, entries 5-7).

Table 3.1. Amount of radioactivity (mean ± standard deviation, n=3) decay corrected to the end of irradiation, obtained under different experimental conditions for production methods A (single irradiation) and B (double irradiation); NA: not applicable.

Entry	P_1 (bar)	C_1 (µAh)	C_2 (µAh)	C_3 (µAh)	A (GBq)
1[a]	2	4	NA	NA	0.27±0.03
2[a]	2	8	NA	NA	0.49±0.04
3[a]	4	4	NA	NA	0.58±0.04
4[a]	4	8	NA	NA	0.80±0.06
5[b]	NA	NA	1	1	2.30±0.08
6[b]	NA	NA	1	2	2.47±0.08
7[b]	NA	NA	1	4	2.75±0.13
8[b]	NA	NA	4	4	8.43±0.59

[a] Production method A. [b] Production method B; P_1: CF_4 filling pressure under method A; C_1: integrated current, method A; C_2: integrated current, first irradiation, method B; C_3: integrated current, second irradiation, method B.

In previous works, the mechanism for the formation of $[^{18}F]CF_4$ was described as a result of a substitution reaction of a "hot" ^{18}F atom with CF_4, leading to the vibrationally excited molecule $CF_3{}^{18}F^*$, which ultimately deactivates by collision with the surrounding molecules leading to the formation of $[^{18}F]CF_4$ (18). In our case, when method B was used, the reaction mechanism should differ from that previously

described. During the second irradiation, the incident protons impact majorly in the gas, and hence hot ^{18}F atoms are only produced by the $^{19}F(p,pn)^{18}F$ nuclear reaction. As can be seen in Table 3.1, the irradiation time for the second beam has a minor contribution to the final amount of $[^{18}F]CF_4$. Hence, we hypothesize that the ionic specie CF_3^+, which is unreactive towards CF_4, is formed during irradiation of the CF_4/Ne mixture. This ion beam-induced ionic specie reacts with an ^{18}F atom absorbed on the walls of the target chamber, leading to the rapid formation of $[^{18}F]CF_4$. In our hands, 8.43±0.59 GBq of $[^{18}F]CF_4$ could be produced in short irradiation times. These results are extraordinary, especially considering that full optimization of the experimental conditions was not carried out. An increase in the CF_4 filling pressure or application of higher integrated current values in the first irradiation may lead to higher production yields.

Gas chromatography analysis showed the presence of two radioactive species at the end of the cryogenic trapping step, with retention times (R_t) of 1.93 and 2.53 min (Figure 3.7a), identified as $[^{18}F]CF_4$ and $[^{11}C]CO_2$, respectively. Mass spectrometry analysis confirmed the presence of 5 major species with R_t = 1.45, 1.65, 2.25, 2.70 and 3.92 min, corresponding to N_2, CF_4, CO_2, C_2F_6, and $C_2F_6O_3$, respectively (Figure 3.7c). One very minor peak appeared at R_t = 4.50 min, but the chemical structure could not be elucidated (Figure 3.7c, insert). $[^{11}C]CO_2$ could be easily removed by passing the irradiated gases through a soda lime trap before cryogenic trapping (Figure 3.7b), yielding radiochemically pure $[^{18}F]CF_4$ (Figure 3.7b).

With the aim of proving the suitability of our method for the preparation of other fluorinated gases, the synthesis of $[^{18}F]SF_6$ was approached using the same experimental conditions (methods A and B) but replacing the CF_4 gas bottle by an SF_6 gas bottle. Under method A, an integrated current of 4 μAh resulted in the formation of 0.36±0.05 GBq of $[^{18}F]SF_6$, while under method B, integrated currents of 4 μAh in both irradiations resulted in 6.77±0.21 GBq of pure $[^{18}F]SF_6$. The analysis of the radioactive gas by radio GC-MS after purification using a soda lime trap and cryogenic trapping confirmed the presence of only one radioactive species with R_t = 3.35 min, which was identified as $[^{18}F]SF_6$. MS analysis confirmed the presence of 4 species with

R_t = 1.45, 1.65, 1.70, and 2.95, that were identified with the mass spectra as N_2, CF_4, F_3N, and SF_6. A very minor peak appeared at R_t = 4.35 min, but the chemical structure could not be identified. These results are extremely positive, as they suggest that the strategy reported here might be extrapolated to the preparation of other radiolabelled fluorinated gases.

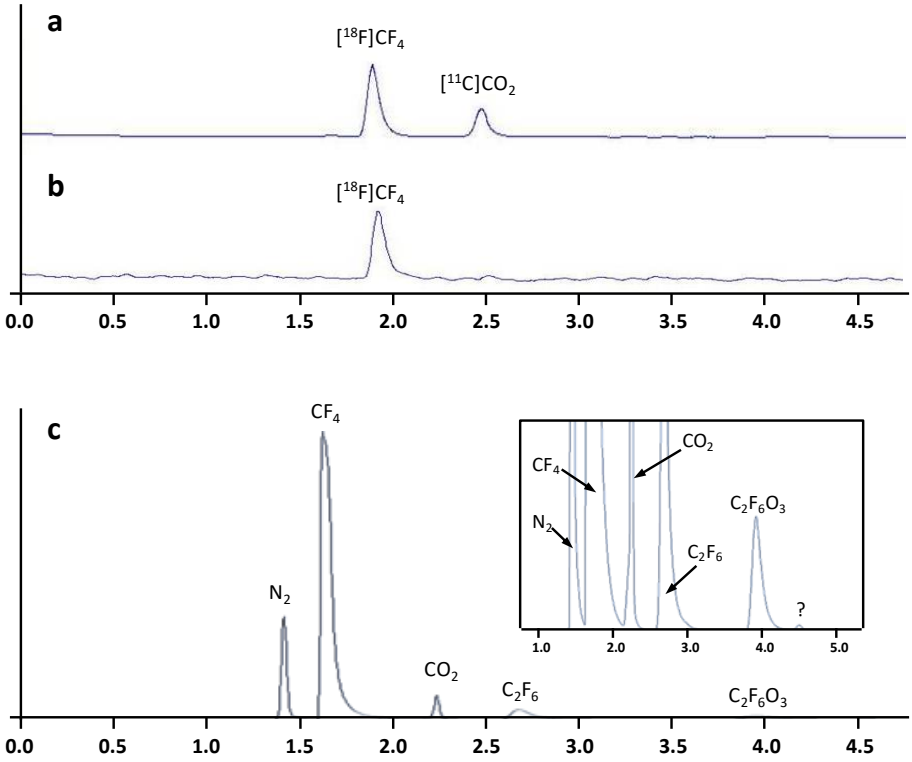

Figure 3.7. (a, b) Chromatograms (radioactivity detector) corresponding to the analysis of $[^{18}F]CF_4$ before (a) and after (b) passing through a soda lime trap; (c) chromatogram (MS detector) corresponding to the analysis of $[^{18}F]CF_4$.

3.4.2. Imaging Studies

To prove the suitability of the radiofluorinated gases for the assessment of lung ventilation, *in vivo* PET studies combined with Computerised Tomography (CT) imaging were approached using $[^{18}F]CF_4$. In nuclear imaging, the administration protocol has to be defined according to the molecular or functional information of interest. Here, a simple administration protocol based on dilution of the radioactive gas (total amount of radioactivity = 74±8 MBq) in the carrier oxygen over ca. 70 seconds and acquisition of dynamic images (19 frames: 3x20s, 10x10s, 4x20s and 2x30s; administration of

[^{18}F]CF_4 starts at t=60 s) was applied in order to get a first proof of concept. The time-activity curve in the lungs showed a sharp increase just after the onset of the administration of [^{18}F]CF_4 (Figure 3.8a). When the delivery was discontinued, almost complete elimination from the lungs was achieved in a few seconds. Time-averaged PET images clearly show uniform distribution of the gas within the lungs (Figure 3.8b).

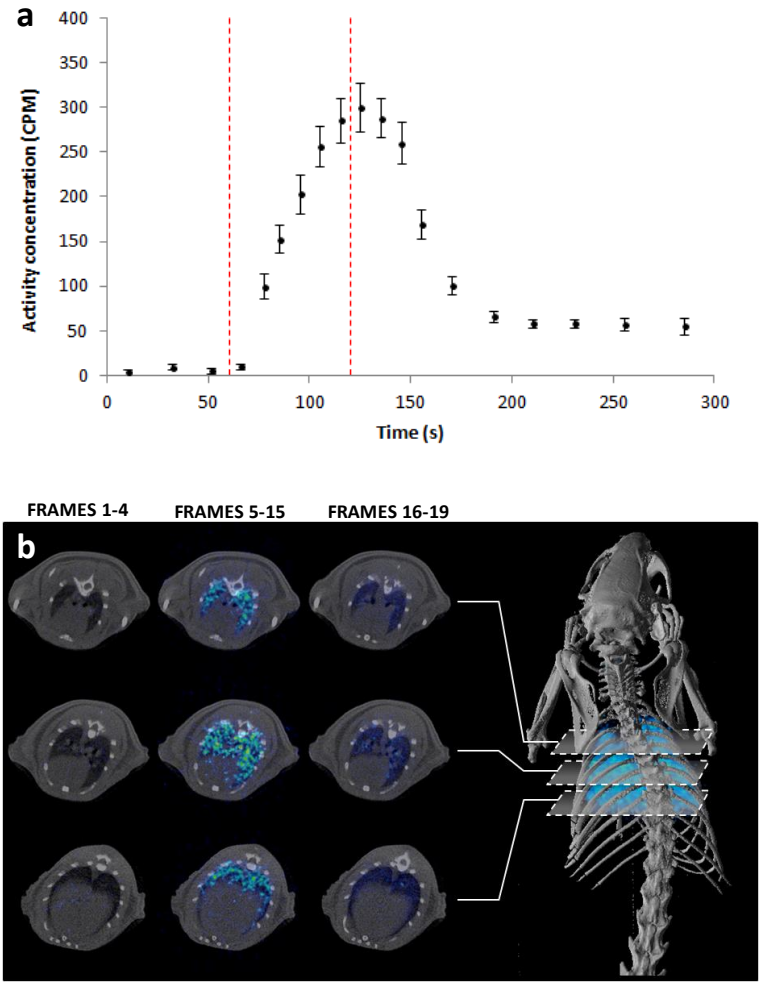

Figure 3.8. (a) Concentration of radioactivity (arbitrary units, counts per minute, CPM) in the lungs as a function of time (mean ± standard deviation, n=2); (b) Left: Axial PET-CT slices of the thoracic cavity, before (frames 1-4), during (frames 5-15) and after (frames 16-19) administration of [^{18}F]CF_4; right: surface-rendered 3D-CT images of the skeleton corregistered with volume-rendered 3D-PET images of the lungs (Averaged frames 5-15).

Considering the administration time (70 s) and average tidal volume of the rats, the total volume of inhaled/exhaled air during [^{18}F]CF_4 administration was estimated to be ca. 100 mL. The whole amount of radioactivity (74±8 MBq) was diluted in 1.16 L of gas

(O_2 flow rate = 1 L/min; administration time = 70s); hence, the amount of radioactivity reaching the lungs can be estimated to be 6.3 MBq. In spite of the low amount of radioactivity, excellent images showing uniform distribution of the radiolabelled gas all over the lungs could be obtained.

The use of inhaled gases as contrast agents has the advantage that, contrary to aerosols or labelled particles, gases distribute according to regional ventilation. The ^{18}F-fluorinated gas reported in this chapter has two major advantages: (i) the non-radioactive analogue is chemically inert, non-toxic, and has poor solubility in water; hence, low translocation to the blood torrent and remote organs is expected. Additionally, the gas is rapidly exhaled. Altogether, these factors contribute to a minimisation of the radiation dose posed on the subject under investigation; and (ii) the relatively long half-life of ^{18}F and the efficient production method reported here should enable centralized production and distribution to nearby imaging centres, facilitating a potential translation into the clinical setting, in a similar fashion to the currently established production/distribution network for the radiotracer 2-deoxy-2-(^{18}F)fluoro-D-glucose, commonly known as [^{18}F]FDG.

Currently, the gold standard used in the clinics for the assessment of regional lung ventilation is planar scintigraphy or SPECT using Technegas as the contrast agent. In this method, ^{99m}Tc-labelled graphite particles are generated and inhaled by the patient before entering the camera. After inhalation, the patient is subjected to an static imaging session and information about the regional ventilation (in 3D when SPECT is used, in 2D when planar scintigraphy is used) can be obtained.

Besides the already mentioned limitations of SPECT in terms of sensitivity, resolution and absolute quantification, there are two significant drawbacks of this approach that are worth to mention. First, as already mentioned, the particles tend to accumulate in central airways and hypo-ventilated areas, due to convection effects. Second, the biological half-life of Technegas in healthy subjects is 135 hours (19), resulting in a high dose posed on the investigated subject. In this regard, our approach would contribute to a less invasive medicine. Although dosimetry studies have not been carried out yet, the rapid exhalation and the low dose required to obtain the images anticipate a

radiation dose for the patient much lower than that released with the current gold standard. Finally, it is worth mentioning that ^{99m}Tc is usually obtained from ^{99}Mo/^{99m}Tc generators, being ^{99}Mo produced in nuclear reactors. The radioactive gases proposed in our work are produced in a cyclotron, and hence represent an environmental friendly alternative to the current state of the art.

3.5 Summary and Conclusion

In summary, we report here the unprecedented, highly efficient, simple and easy-to-automate preparation of [^{18}F]CF_4 and [^{18}F]SF_6 following an ion beam induced chemical reaction based on a double proton irradiation approach. The general methodology reported here might be extended to other fluorinated gases. [^{18}F]CF_4 has proven suitable for the determination of regional lung ventilation using PET-CT. Due to the efficiency of the synthetic method and the relatively long half-life of Fluorine-18, the radiofluorinated gases reported here may become powerful tools in the diagnostic, prognostic or evaluation of response to treatment for a wide variety of lung diseases. The establishment of a production/distribution network to facilitate translation to the clinical setting can be foreseen. Future works will focus on the refinement and full optimization of the experimental set up, an extension of the methodology to the preparation of other ^{18}F-fluorinated gases and the evaluation of the radiolabelled gases as ventilation markers using animal models of impaired lung ventilation.

3.6. References

1. MacFall JR, Charles HC, Black RD, Middleton H, Swartz JC, Saam B, et al. Human lung air spaces: potential for MR imaging with hyperpolarized He-3. *Radiology*. **1996**;200(2):553-8.

2. Roberts DA, Mai VM, Salerno M, Lipson DA, Rizi RR. Functional magnetic resonance imaging of the lung. *Applied Radiology*. **2003**;32(2):41-8.

3. Wittenberg LJ, Cameron EN, Kulcinski GL, Ott SH, Santarius JF, Sviatoslavsky GI, et al. Review of 3He resources and acquisition for use as fusion fuel. *Fusion Technology*. **1992**;21(4):2230-53.

4. Kuethe DO, Caprihan A, Fukushima E, Waggoner RA. Imaging lungs using inert fluorinated gases. *Magnetic resonance in medicine*. **1998**;39(1):85-8.

5. Ruiz-Cabello J, Barnett BP, Bottomley PA, Bulte JW. Fluorine (19F) MRS and MRI in biomedicine. *NMR in Biomedicine*. **2010**;24(2):114-29.

6. Wolf U, Scholz A, Terekhov M, Muennemann K, Kreitner K, Werner K, et al. Fluorine-19 MRI of the lung: first human experiment. *Proceedings of the International Society for Magnetic Resonance in Medicine*. **2008**;16:3207.

7. Fazio F, Jones T. Assessment of Regional Ventilation by Continuous Inhalation of Radioactive Krypton-81m. *British Medical Journal*. **1975**;3(5985):673.

8. Palmer J, Bitzén U, Jonson B, Bajc M. Comprehensive ventilation/perfusion SPECT. *Journal of Nuclear Medicine*. **2001**;42(8):1288-94.

9. Burch WM, Sullivan PJ, McLaren CJ. Technegas - a new ventilation agent for lung scanning. *Nuclear Medicine Communications*. **1986**;7(12):865-71.

10. Rahmim A, Zaidi H. Pet versus spect: Strengths, limitations and challenges. *Nuclear Medicine Communications*. **2008**;29(3):193-207.

11. Rhodes CG, Hughes JM. Pulmonary studies using positron emission tomography. *European Respiratory Journal*. **1995**;8(6):1001-17.

12. Senda M, Murata K, Itoh H, Yonekura Y, Torizuka K. Quantitative evaluation of regional pulmonary ventilation using PET and nitrogen-13 gas. *Journal of Nuclear Medicine*. **1986**;27(2):268-73.

13. Walter CSELG. The preparation of sulfur hexafluoride and some of its physical properties. *Journal of the American Chemical Society*. **1930**;52(11):4302-8.

14. Nickles RJ, Daube ME, Ruth TJ. An ^{18}O target for the production of$[^{18}F]F_2$. *Applied Radiation and Isotopes*. **1984**;35:117.

15. Roberts AD, Oakes TR, Nickles RJ. Development of an improved target for $[^{18}F]F_2$ production. *Applied Radiation and Isotopes*. **1995**;46(2):87-91.

16. Běták E, Mikołajczak R, Staniszewska J, Mikołajewski S, Rurarz E, Wojtkowska J. Production of ^{18}F by proton irradiation of C_6H_6NF and $C_6H_5NF_2$. *Nukleonika*. **2011**;56(4):269-76.

17. Ruth TJ, Wolf AP. Absolute Cross Sections for the Production of ^{18}F via the $^{18}O(p, n)^{18}F$ Reaction. *Radiochimica Acta*. **1979**;26(1):21-4.

18. Bishop A, Satyamurthy N, Bida G, Hendry G, Phelps M, Barrio JR. Proton irradiation of $[^{18}O]O_2$: Production of $[^{18}F]F_2$ and $[^{18}F]F_2$ and $[^{18}F]OF_2$. *Nuclear Medicine and Biology*. **1996**;23(3):189-99.

19. Kawakami K, Iwamura A, Goto E, Mori Y, Abe Hirasawa TY, Ishida H, et al. Kinetics and clinical application of99mTc-technegas. *Kakuigaku*. **1990**;27(7):725-33.

Chapter 4. Evaluation of pulmonary administration methods in rodents using nuclear imaging techniques

4.1. Introduction

Lung administration of drugs has recently gained attention, especially when the lung is the target organ, e.g. to treat lung cancer or airway diseases such as asthma, cystic fibrosis and chronic obstructive pulmonary disease (COPD) (1). Pulmonary administration offers numerous advantages as a delivery route compared to oral or intravenous administration. On one hand, bioavailability of drugs can be enhanced, because contrary to gastrointestinal tract and liver, lung possesses limited intracellular and extracellular drug metabolizing enzyme activities (1). On the other hand, lung administration usually leads to higher absorption rate, reduced drug doses and rapid onset of action (1, 2).

Critical endpoints in the development of a drug formulation are the preclinical studies conducted with various animal models (3). In the particular context of aerosols for inhalation, the administration into animals is a critical challenge especially in small rodent species, and only a few methods of administration have been developed so far. Endotracheal and intratracheal insufflations have the advantage that they enable specific deliver of the drug to the lung, with high predictability in terms of delivered dose. Additionally, compared to intratracheal administration (via an incision into the trachea), endotracheal insufflations are minimally invasive and can be used in repeated dose studies. Two major disadvantages of this method are the potential induction of lesions due to the introduction of the insufflators and the need to maintain the animals under anaesthesia during the administration, which can cause some problems in certain scenarios.

Alternatively to endo/intratracheal insufflations, inhalation towers can be used for pulmonary administration of aerosols to small rodents. In this case, the aerosol is generated in a chamber and is incorporated into the lungs of the exposed animals through natural respiration; hence this method is perceived to result in a

homogeneous distribution of the aerosol within the lungs. Additionally, several animals can be exposed simultaneously. One major drawback of this alternative is the need to keep the animals under anaesthesia during long periods of time. This limitation can be overcome by establishing a training process to ensure that animals are accustomed to the exposure tubes (4), although this process is time-consuming and requires the participation of experienced personnel.

Irrespective of the administration strategy, two critical factors have to be considered in lung administration: (i) the dose actually deposited in the lungs, which is critical when planning dose-dependent pre-clinical studies, such as toxicity, pharmacokinetics and efficacy studies (5); and (ii) the regional distribution within the lungs, which is of utmost importance because uniform distribution among the different lung lobes is required both to guarantee an effective treatment and to prevent toxic or side effects due to local, potentially harmful deposition of the drug.

One of the main challenges in addressing the above mentioned points is that drugs (or the aerosols containing the drugs) are extremely difficult to detect and quantify once distributed in a biological system. One alternative to overcome this difficulty consists of labelling the drug or the aerosol with a fluorescent tag, enabling their localization *in vivo* using optical imaging techniques. For example, in a recent study a newly developed aerosol generator was tested for pulmonary administration to the lungs of mice and compared to an endotracheal insufflator (6), using Fluorescence Molecular Tomography (FMT) and ovalbumin as a model protein labelled with a fluorescent dye. In spite of the suitability of this approach, optical imaging techniques have severe limitations *in vivo*, mainly due to the poor penetration capacity of visible or infrared light in tissues, which limits the application of the technology to small rodents. Additionally, quantification of the images is extremely challenging. One alternative to overcome these drawbacks consist of labelling the drug or the aerosol with a positron emitter (7). The disintegration of the positron emitter leads ultimately to the generation of high energy gamma rays, which have virtually no penetration limits and can be externally detected and processed to generate three dimensional (3D)-images. Such images provide quantitative information about the spatiotemporal distribution of

the labelled specie (8). This approach has been applied to evaluate changes in the deposition of inhaled aerosols within the lung related to the presence of disease or resulting from inhalation challenge interventions or inhaled therapies in the clinical field (9).

In the context of PneumoNP, and as previously mentioned, our consortium has developed novel nanosystems to treat drug-resistant lung infections, which had to be assayed in therapeutic experiments in a rat model using lung administration in aerosol form. In order to select the most convenient administration strategy, three different options were considered: (i) endotracheal insufflations using the PennCentury MicroSprayer® Aerosolizer; (ii) inhalation using a newly developed nebulizer; and (iii) inhalation using a commercially available nebulisation system, the Aeroneb® Lab Micropump Nebulizer (Aerogen, Dangan, Ireland). In all cases, the aerosol was labelled with 2-deoxy-2-(^{18}F)fluoro-D-glucose ([^{18}F]FDG), a radiotracer widely used in the clinical field for the early diagnose and evaluation of the response to treatment of different cancer types. For the three administration methods, the percentage of administered dose deposited in the lungs and the regional distribution of the aerosol within the lungs was evaluated using *in vivo* PET imaging and complementary *ex vivo* techniques such as dissection/gamma counting experiments, and eventually *ex vivo* PET imaging. Uniform deposition of the labelled aerosol within the lungs could be achieved using inhalation, while poorly-uniform distribution was often and unpredictably achieved when the MicroSprayer® Aerosolizer was used, although the latter resulted in almost quantitative deposition of aerosol in the lungs.

4.2. Objectives

The specific objective of this work is:

1. To compare three different aerosol administration systems in wild type rats, in terms of: (a) uniformity of the regional distribution of the aerosol in the lungs; and (b) percentage of the nebulised dose actually deposited in the lungs.

4.3 Experimental Part

4.3.1 Animal experiments: general

All animal experiments described in the following sections were performed in accordance with the Spanish policy for animal protection (RD53/2013), which meets the requirements of the European Union directive 2010/63/UE regarding the protection of animals used in experimental procedures. All experimental procedures were approved by the Ethical Committee of CIC biomaGUNE and authorized by the local authorities.

4.3.1.1. Aerosol administration

Six-to–eight weeks-old female Sprague Dawley rats (Janvier, Le Genest-Saint-Isle, France) weighting ca. 225 g were used in all the experiments.

4.3.1.2. Endotracheal insufflations

Endotracheal insufflations were carried out using the Penn-Century MicroSprayer® Aerosolizer (FMJ-250 High Pressure Syringe Model, Penn-Century. Inc. Wyndmoor, USA; henceforth "Penn-Century Aerosolizer"; Figure 4.1).

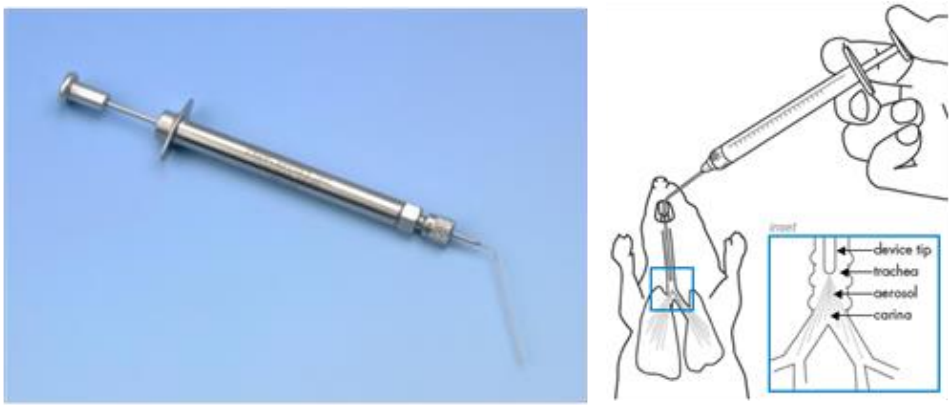

Figure 4.1. Left: Picture of the PennCentury Microsprayer; right: schematic illustration of the endotracheal administration procedure followed to perform the experiments. Image courtesy of Penn-Century, Inc.

Deep sedation was induced to the animals (n = 6) by inhalation of 5% isoflurane in pure O_2. The tip of the delivery needle was carefully positioned just above the carina and a pre-defined volume (established by using spacers in the syringe plunger) of injectable

[^{18}F]FDG solution (Provided by Iba Molecular Spain and diluted with ultrapure water 1:25; 50 µL; amount of radioactivity around 1.85 MBq) was administered. A small animal Laryngoscope (Penn-Century, Model LS-2) was used for correct visualization of the epiglottis. Immediately after administration, rats were divided in two groups (group 1: n = 3; group 2: n = 3), and submitted to *in vivo* and *ex vivo* imaging experiments, respectively (see below).

4.3.1.3. Inhalation using an in-house developed aerosol generation system

The aerosol inhalation system developed at Ingeniatrics Tecnologías (henceforth "Ingeniatrics nebuliser") consisted of the following parts: (a) Aerosol generation unit with Flow Blurring® (FB) technology. Two different models were assayed. One of them, the FB240 nozzle, had an equal exit orifice diameter and inner tube diameter of 240 µm. The other nozzle (FB100) had an orifice and inner tube diameter of 100 µm; (b) a peristaltic pump to push the labelled solution to be nebulised at a constant flow rate; (c) a compressed air supply, equipped with a pressure regulator and a pressure meter; (d) ON/OFF controlling device; (e) main nebulisation and distribution chamber; and (f) an exit outlet to prevent overpressure in the main chamber (see Figure 4.2).

The nebuliser was placed at the bottom of the nebulisation chamber, which was directly connected to four rat holders coupled with rubber adaptors to enable appropriate positioning of the animals and only-nose exposure to the aerosol. An exit outlet was also installed at the top of the nebulisation chamber to avoid overpressure in the system and to trap the radioactive aerosol exiting the main chamber. For this purpose, two washing bottles were connected in series and a vacuum pump was installed to keep the system at slight under-pressure (-50 Pa), thus ensuring that all the radioactive material was properly trapped.

To conduct inhalation studies, rats (n = 6) were anesthetized by an intraperitoneal (IP) injection of a mixture of medetomidine, midazolam and fentanyl (0.6, 6 and 0.02 mg/Kg, respectively). Once animals were under sedation, they were introduced into identical cylindrical oro-nasal exposure holders. Then, a solution (1.5 mL) containing [^{18}F]FDG (Provided by Iba Molecular Spain and diluted with ultrapure water 1:12;

amount of radioactivity: 370±10 MBq) was aerosolized using the system described above. After finalizing the exposure, animals were randomly divided in two groups (group 3: n = 3; group 4: n = 3), and submitted to *in vivo* and *ex vivo* imaging experiments, respectively (see below).

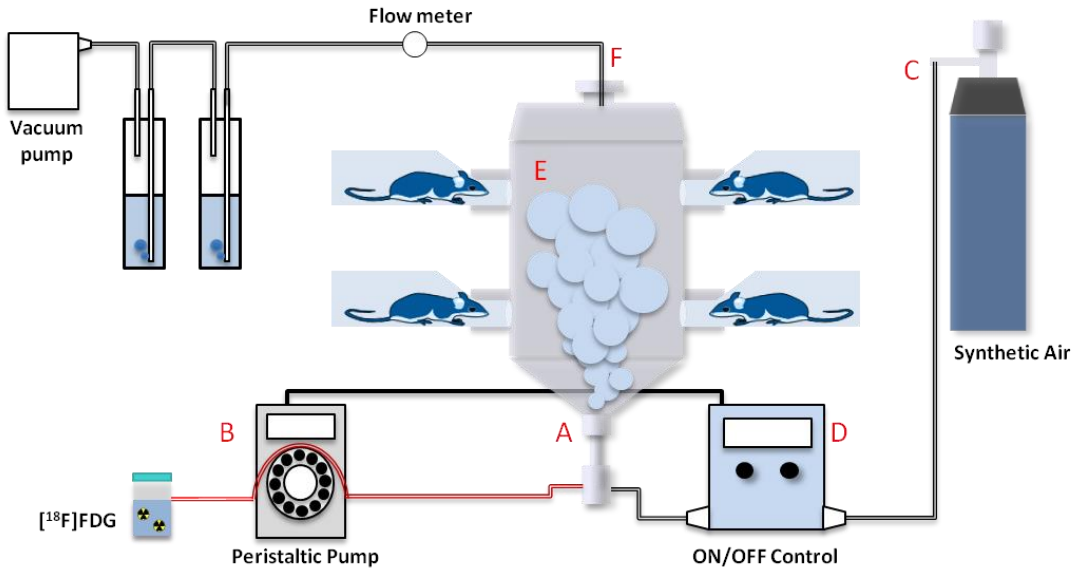

Figure 4.2. Complete aerosol generation system setup for 4 rats: A) Nozzle (FB240 or FB100); B) Peristaltic pump; C) Synthetic air bottle; D) ON/OFF control device; E) nebulisation chamber with four rat holders and F) exit outlet.

4.3.1.4. Inhalation using the Aeroneb® Lab Micropump Nebulizer

For inhalation studies using the commercially available Aeroneb® Lab Micropump Nebulizer (henceforth "Aeroneb nebulizer"), animals (n = 6) were submitted to the same procedure as described above (section 4.3.1.2), using an inhalation configuration as depicted in Figure 4.3. Actually, the system used in our experiments was an adaptation of a device currently used in humans, the Aerogen® Pro nebulizer (Aerogen, Dangan, Ireland) and allowed exposure of one animal at a time, by using a rat nebulizer Delivery System (AG-ALSMHLD-RAT, Kent Scientific Corporation, Connecticut, USA). In this case, the generation of the aerosol relies in the presence of a vibrating membrane just below the nebulizer's reservoir, enabling fast administration of medicines to patients with very low residual losses (10, 11). The droplet size can be

tuned by appropriate selection of the membrane's pore size, which in our case was chosen to generate droplets within 4-6 µm in diameter. The air flow, used to push the aerosol towards the animal, was set to 100 mL/min. The total nebulised volume of [^{18}F]FDG (Provided by Iba Molecular Spain and diluted with ultrapure water 1:4) was 0.5 mL containing 370±10 MBq (total exposure time = 5 min). After exposure, animals were randomly divided in two groups (group 5: n = 3; group 6: n = 3), and submitted to *in vivo* and *ex vivo* imaging experiments, respectively (see below).

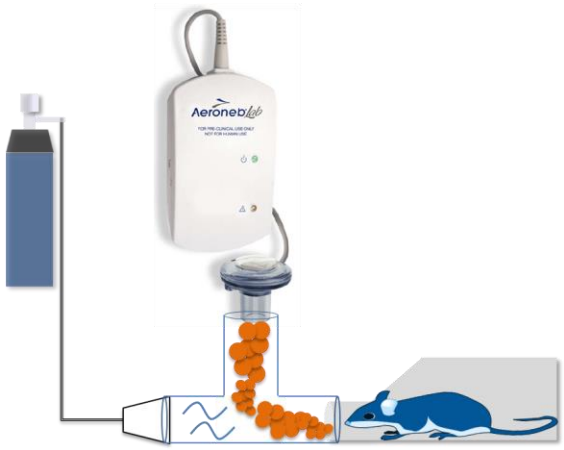

Figure 4.3. Illustration of the Aeroneb Lab Micropump Nebulizer connected to the rat holder.

4.3.2. Droplets size measurements

Aerosols generated by different nebulizers were characterized using a Sympatec Helos/BF Magic laser diffraction system (HELOS, Sympatec, Clausthal-Zellerfeld, Germany; see Figure 4.4) at Ingeniatrics Tecnologías (Seville, Spain). In brief, the nebulizer was clamped into a stand and the mouthpiece exit of the nebulizers positioned ≈50 mm from the Fourier lens face and ≈100 mm from the laser beam. The formulation (appropriate dilution of completely decayed [^{18}F]FDG solution with ultrapure water) was then nebulised through the laser beam. The measurements were performed with six runs of 100 ms duration each. The droplet diameter distributions were parameterised by their Mean Droplet Size Distribution (MDSD) and Geometric Standard Deviation (GSD).

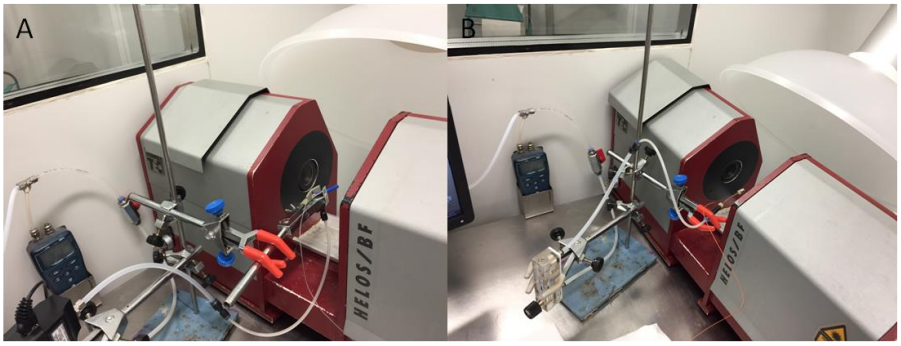

Figure 4.4. Pictures of the Sympatec Helos/BF Magic laser diffraction system used for the assessment of aerosols' droplets size measurements carried out at Ingeniatrics Tecnologías (Seville, Spain), using the FB240 (A) and FB100 (B) nozzles.

4.3.3. *In vivo* imaging experiments

Without recovering from sedation, animals from experimental groups 1, 3 and 5 were positioned in an eXploreVista-CT small animal PET-CT system (GE Healthcare, USA) to perform *in vivo* studies. For animals in groups 3 and 5, still under the effects of medetomidine/midazolam/fentanyl, no additional anaesthesia was required during image acquisition. For animals in group 1, anaesthesia was maintained with 1.5-2% isofluorane in pure O_2.

During imaging, rats were kept normothermic using a heating blanket (Homeothermic Blanket Control Unit; Bruker). Dynamic PET images (energy window: 400-700 KeV) were acquired with the following frames: 4 x 15 s, 4 x 30 s, 3 x 60 s and 3 x 90 seconds. In all cases, four beds were defined to acquire whole body images. After each PET acquisition, a CT scan (X-Ray energy: 40 kV, intensity: 140 µA) was performed for a later attenuation correction in the image reconstruction and for unequivocal localization of the radioactivity. Random and scatter corrections were also applied to the reconstructed image (filtered back projection reconstruction algorithm), generating a 175x175x220 dimension image, with a 2 mm axial FWHM spatial resolution in the centre of the Field Of View (FOV).

PET-CT images of the same animal were co-registered and analysed using PMOD image processing tool. Volumes of interest (VOIs) were manually delineated on the whole lungs to assess the amount of radioactivity deposited in this organ. Additionally, small

spherical VOIs (diameter = 1 mm) were drawn in the different lung lobes and time–activity curves (decay corrected) were obtained as cps/cm^3 in each VOI. Curves were transformed into real activity (Bq/cm^3) curves by using a calibration factor, obtained from previous scans performed on a phantom (micro-deluxe, Data spectrum Corp.) under the same experimental conditions (isotope, reconstruction algorithm and energetic window). For each curve, an exponential equation was adjusted and the amount of radioactivity in each region at administration time was calculated by extrapolation.

4.3.4. *Ex vivo* imaging experiments

Without recovering from sedation, animals from experimental groups 2, 4 and 6 were sacrificed by cervical dislocation immediately after administration of the labelled aerosol. In all cases, the time gap between the end of the exposure to the aerosol and the sacrifice time was less than 10 seconds. The respiratory system of the rats (trachea and both lungs) was fixed with formalin (10% formalin solution, neutral buffered) and subsequently harvested. PET-CT images of the extracted organs were acquired for 60 minutes (n = 3 per group). Image reconstruction and analysis was performed as above, although in this case exponential curves were not adjusted because static images were acquired. After finishing the imaging session, the lungs were dissected into different lobes, and the amount of radioactivity in each lobe was accurately determined by gamma counting (WIZARD2 Gamma Counter, PerkinElmer, Waltham, USA).

4.4 Results and discussion

4.4.1. Aerosol droplet size measurements

For inhalation, the most important characteristic of an aerosol is the respirable dose, which is the fraction of droplets in the respirable range. With the aim of having a homogeneous distribution along the whole respiratory track, main requirement in terms of droplet size is having a MSDS below 4 microns with a high percentage of droplets with a diameter in the range 0.9-5.25 µm (12).

The droplet size obtained after nebulization depends on the electrolyte concentration of the solution, as recently reported (Beck-Broichsitter et al. 2017). For this reason, in the current work the aerosol droplet size was determined with a proper dilution of the [^{18}F]FDG solution with purified water, in order to obtain representative results for in vivo experiments. The [^{18}F]FDG solution provided by IBA Molecular Spain contained 10 mg/mL of NaCl, 1.5 mg/mL of NaH_2PO_4, and 0.4 µg/mL of ethanol, and dilutions with purified water 1:25, 1:12 and 1:4 were carried out to assess droplet size using the Penn-Century Aerosolizer, the Ingeniatrics nebuliser and the Aeroneb nebuliser, respectively.

The aerosol generated with the nozzles developed at Ingeniatrics Tecnologías (FB240 and FB100) was produced using a nebulizer based on Flow Blurring® technology. Flow Blurring® is a purely mechanical atomization technique that produces highly turbulent pre-mixing between gas and liquid streams. As a consequence of this special regime, very good quality aerosols with ultrafine droplets are obtained. Given a specific geometry design, droplet size distribution could be selected by choosing the proper set of operational parameters (pressure and liquid flow rate). Hence, several liquid flow rates and pressures were tested for the FB240 and FB100 nozzles, in order to produce aerosols in the respirable range (optimal conditions are shown in Table 4.1.). At these experimental conditions, both nebulizers were able to generate a high percentage of droplets in the desired range of 0.9-5.25 µm.

The aerosol produced by the Penn-Century Aerosolizer resulted in significantly higher droplet size, in the range of 20 µm, which was in great accordance with the value specified by the manufacturer. In this case, only a small fraction (2.6%) of the droplets fell within the desired range (0.9-5.25 µm).

Evaluation of the droplet size in the aerosol generated with the Aeroneb nebulizer resulted in MSDS of 4.52±1.59 µm, confirming that most of the droplets were within the respirable range. These results are well aligned with previously reported values using the same system.

Table 4.1. Summary of the properties of the aerosols produced using different nozzles (FB240 and FB100) and under different experimental conditions, using pure water; Q liq: liquid flow rate; P air: air pressure; Q air: air flow rate; MSDS: mean droplet size distribution.

Aerosol Producing Device	Q liq (mL/min)	P air (mbar)	Q air (L/min)	MSDS (µm)	% droplets 0.9< MSDS <5.25
FB100	0.25	3000	0.67	3.00	61.15
FB100	0.25	3500	0.82	2.00	66.8
FB240	0.3	3000	1.57	2.43	64.28
FB240	0.3	4500	1.6	3.28	71.11
PennCentury	250 µL	-	-	23.33	2.61

4.4.2. *In vivo* imaging experiments

Evaluation of the dynamic images obtained after administration by endotracheal insufflation using the Penn-Century Aerosolizer showed progressive elimination of the radioactivity from the lungs. However, more than 85% of the starting radioactivity was still in the lungs after 10 minutes, suggesting slow clearance from this organ.

PET images acquired immediately after administration of [^{18}F]FDG using the three nebulisation methods showed different distribution patterns within the lungs (Figure 4.5).

When [^{18}F]FDG was administered by endotraqueal insufflation using the Penn-Century Aerosolizer, the radioactive aerosol was not uniformly deposited in the whole lungs. Indeed, minute involuntary tilts of the microsprayer when administering the dose resulted in the deposition of the aerosol in only one lung, a phenomenon which could be observed even after mastering the technique (Figures 4.5a-4.5c). Of note, even when the aerosol reached both lungs, the regional distribution was not uniform within the lungs, and the presence of hot spots and under-exposed regions could be observed by visual inspection of the images. Generally, the lower regions of the lungs received

systematically less amount of aerosol that the upper regions. Our results are in partial agreement with previous studies in which the regional distribution of TiO_2 NPs in rat lungs was investigated after aerosol administration using the same system (13). In this previous work, the authors found low inter-animal variation in terms of dose deposited in the lungs, although the middle lobes were the regions which systematically received fewer doses. In our case, despite the high intra-individual variation and the high variability of the method, it was the lower regions of the lungs the ones which received fewer doses.

Administration of the labelled aerosol using any of the two nebulisers resulted in a more uniform distribution of the aerosol within the whole lungs, as clearly seen by visual inspection of the images (see Figures 4.5d and 4.5e). The images were quantified to get precise data regarding the amount of radioactivity present in each of the lung lobes. With that aim, and using PMOD image analysis software, different spherical volumes of interest (VOIs) were drawn in the different regions of the lungs. The lungs were divided in six different regions (Figure 4.5f): left superior lobe (LS), left middle lobe (LM), left inferior lobe (LI), right superior lobe (RS), right middle lobe (RM) and right inferior lobe (RI), and VOIs were drawn in the different regions. Quantitative data (Figures 4.5g-4.5i) clearly show the lack of uniformity in the deposition of aerosol in the lungs when the Penn-Century Aerosolizer was used. Indeed, Figure 4.5g confirms that endotracheal insufflation results in non-uniform distribution of radioactivity, while the high standard deviation values reflect the high inter-subject variability. Contrarily, Figures 4.5h and 4.5i show that the relative concentration of radioactivity in the different lobes is similar, while small standard deviation values are obtained, confirming the low intra-subject variability.

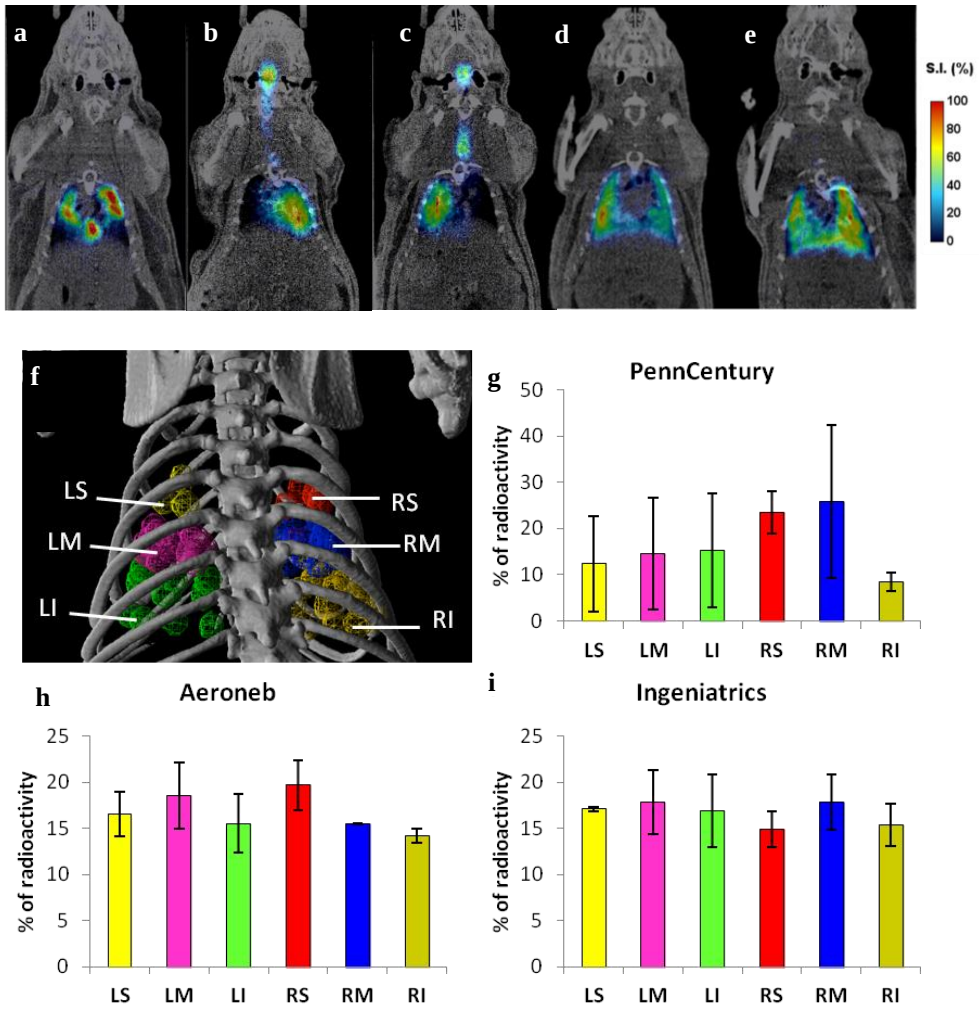

Figure 4.5. (a-e) Representative coronal PET-CT rat images obtained immediately after administration of [^{18}F]FDG by (a-c) endotraqueal insufflation using the Penn-Century Aerosolizer (3 different animals); (d) inhalation using the Ingeniatrics nebuliser; and (e) inhalation using the Aeroneb nebulizer; (f) VOIs drawn in the different regions of the lungs; (g-i) percentage of radioactivity in each VOI after administration using the Penn-Century Aerosolizer (e), Aeroneb nebuliser (f) and Ingeniatrics nebuliser (g). LS: left superior; LM: left medium; LI: left inferior; RS: right superior; RM: right medium; RI: right medium; values in (g-i) are expressed as mean ± standard deviation, n=3.

The PET images obtained *in vivo* were not used to determine the fraction of the dose deposited in the lungs, as these values could be more reliably obtained from *ex vivo* studies. In our case, image acquisition was not synchronised with the respiratory and cardiac cycles, and hence absolute quantification of the whole lung could be subjected to motion artefacts. Such artefacts can be neglected during quantification of the spherical VOIs, as these were strategically located within the region of the organ not

affected by lung and heart motion. Hence the determination of regional distribution is reliable. Indeed, our results are well aligned with previous works (6, 13), in which the authors reported a lack of uniformity within the lungs when the Penn-Century insufflators was used in mice. Such lack of uniformity need to be considered when e.g. therapeutic studies are conducted in the preclinical setting, as unexposed areas may remain undertreated while over-exposed regions may result in localised toxicological effects.

4.4.3. *Ex vivo* imaging experiments

Ex vivo imaging experiments were carried out to confirm the results obtained *in vivo* and to obtain more accurate information regarding the regional and local distribution of the [^{18}F]FDG after administration. With that aim, immediately after finishing PET acquisition, animals were sacrificed, lungs were fixed with formalin and *ex vivo* PET-CT images were acquired. The advantage of *ex vivo* imaging with respect to *in vivo* imaging relies in two facts: (i) there are no motion artefacts due to animal respiration, and (ii) images can be acquired for long times; this is not the case of *in vivo* imaging, where the acquisition time is limited by the total time that the animals can remain under anaesthesia. Hence, higher resolution images can be expected from *ex vivo* imaging. Taking into account that >85% of the administered [^{18}F]FDG remains in the lungs at t=10 min after administration and that the time gap between end of exposure and animal sacrifice was less than 10 seconds, we assumed that lung clearance during this time gap could be neglected.

Visual inspection of the images showed similar results to those obtained *in vivo*, this is, uniform deposition within the lungs when the Ingeniatrics and the Aeroneb nebulisers were used (see Figures 4.6c for example of image) and low uniformity when the Penn-Century Aerosolizer was used.

The lungs were finally divided into different lobes and the amount of radioactivity was determined in a gamma counter (Figures 4.6d and 4.6e). Again, gamma counting results confirmed the results obtained *in vivo*. When [^{18}F]FDG was administered using the Penn-Century Aerosolizer, the amount of radioactivity in the different lobes of the

lungs varied significantly. Additionally, high standard deviation values confirm the high inter-subject variability. When the radiotracer was administered by inhalation, the amount of radioactivity was homogenously distributed within the lungs.

The results also confirmed that endotraqueal insufflation was the most efficient administration method, leading to almost quantitative deposition of the aerosol in the lungs (85±3%). Indeed, the rest of the radioactivity could be either absorbed on the walls of the syringe or in the trachea, the latter being contaminated during introduction or withdrawal of the delivery needle.

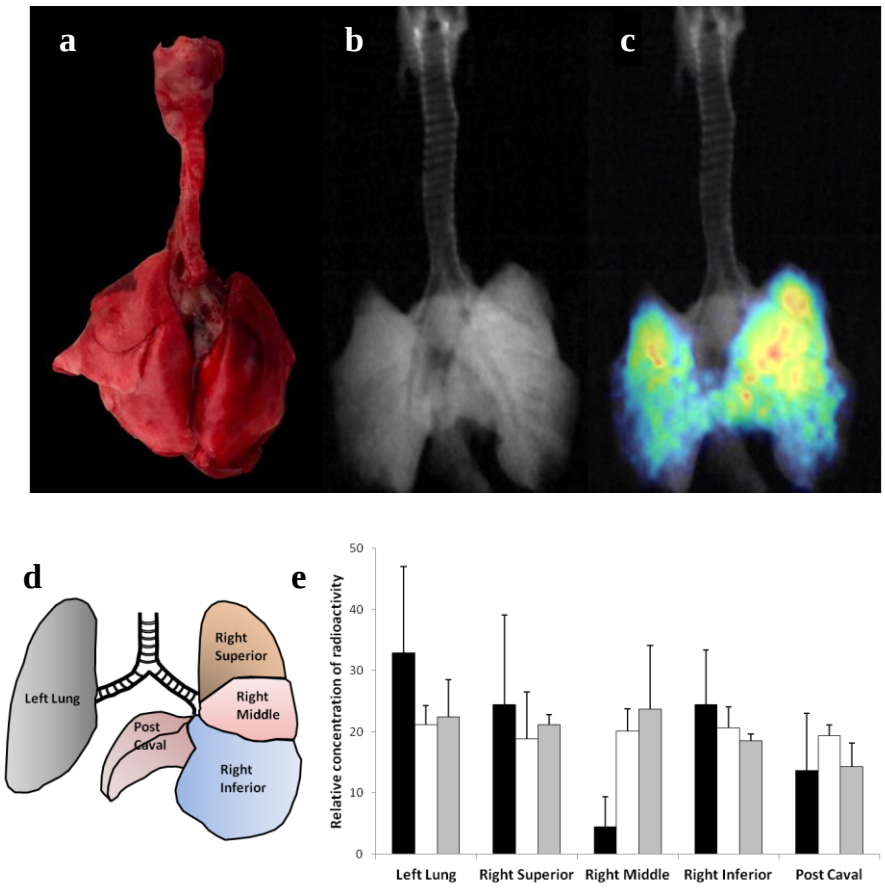

Figure 4.6. (a) Photograph of the harvested, fixed lungs of a rat after exposure to inhalation of [^{18}F]FDG using the Aeroneb nebuliser; (b) Coronal CT image of the harvested lungs; (c) coronal PET-CT *ex vivo* image of the harvested lungs; (d) schematic illustration of the different lung lobes; (e) relative concentration of radioactivity in each lobe after endotraqueal insufflation using the Penn-Century Aerosolizer (black bars), inhalation using Ingeniatric nebuliser (white bars), and inhalation using Aeroneb nebuliser (grey bars).

On the contrary, both aerosol inhalation systems resulted in poor deposition efficiency. Indeed, only 0.07±0.01 and 0.08±0.02 of the aerosolised dose reached the lungs when Ingeniatrics or Aeroneb nebulisers were used. The low dose deposited in the lungs using the Ingeniatrics nebulizer is due to a combination of factors, mainly: 1) The tidal volume of Sprague Dawley rats is around 0.29 mL/100g in resting conditions (14). Considering that under our anaesthetic conditions rats maintained an average breathing frequency of 60 breaths/minute, the inhaled air volume for each rat was estimated to be around 39 mL/min for a rat weight of 225g. Taking into account that in our first trials with the FB240 nebuliser the air flow rate was set to 1.6 L/min (required for a proper generation of the aerosol) a simple mass balance provides a maximum inhaled fraction of 2.4% of the total aerosol, assuming that tidal volume is not significantly affected by the anaesthesia. With the aim of increasing the inhalable fraction, Ingeniatrics developed a new nozzle (FB100) that could work at lower air flow rates (0.6 L/min). Unfortunately, the fraction of the dose actually deposited in the lungs was equivalent to that obtained with the FB240 nozzle.

Additionally to the mass balance issue, a severe condensation of the aerosol in the main chamber could be observed during nebulisation. The fraction of the aerosol condensed was estimated by recovering the condensed fraction and measuring the amount of radioactivity. The results showed that approximately 75% of the nebulised solution was indeed condensed in the walls of the chamber, and hence was not available to be breathed by the animals. Altogether, these results confirm that the maximal theoretical inhalable fraction per animal is close to 0.6%.

Aiming at minimising condensation and to mitigate also mass balance effects, a new device that enabled non-continuous nebulisation was implemented by Ingeniatrics. Different nebulisation experiments were carried out using the ON/OFF control system. In all experiments, the total exposure time was exactly the same (10 minutes) but the time the nebulizer was switched on was modified according to the ON/OFF pattern. Unluckily, continuous and non-continuous nebulisations resulted in equivalent deposition efficiency, which was in all cases very close to 0.1%.

For the Aeroneb nebuliser, the inhaled fraction was similar to that obtained for the Ingeniatrics nebuliser, despite in this case the air flow was set to 100 mL/min and hence higher dose in the lungs could be expected. The low values obtained might be due to severe condensation, which was observed although in this case could not be measured due to the difficulties in recovering the condensed fraction.

Altogether, our results suggest that the administration tool used for the delivery of aerosols in the pre-clinical setting has a huge impact both in the dose deposited in the lungs and in the regional distribution within the lungs. This fact, which has been widely explored in the clinical setting using nuclear imaging techniques (15-17), has remained mostly unexplored in the pre-clinical setting. Taking into account that preclinical studies always precede clinical trials, our results suggest that studies to investigate both parameters should be routinely conducted for a proper interpretation of the results.

The results obtained in the experiments described above have a significant impact on the planning of potential preclinical therapeutic studies using aerosolized drugs. Indeed, the main aim of this work was to provide a recommendation about the nebulisation system to be used in future therapeutic experiments to be conducted at Erasmus Medical Centre (Rotterdam) using an infection rat model and aerosolized antimicrobial peptides encapsulated in/attached to nanocarriers. Based on our results, it was clear that with the Penn-Century Microsprayer most of the drug should be deposited in the lungs, thus reducing the amount of drug required to achieve a certain concentration in the lungs. However, the uniformity of the deposition is questionable and may depend on the operator and uncontrolled experimental factors. On the other hand, the use of the nebulisation systems results in a uniform distribution, but the amount of drug deposited in the lungs is very low, and hence huge amounts of drug would be required to achieve a predefined drug concentration in the lungs.

The distribution of an inhaled drug within the lung clearly influences the effectiveness of that treatment, and a viable treatment may become ineffective if the drug is not delivered in a sufficient concentration to the infected areas within the lung. Considering these facts, our recommendation was to use one of the nebulisation

systems in order to ensure that the whole lung was treated. However, due to the low fraction of the dose deposited in the lungs and the large number of animals to be included in therapeutic experiments, the amount of nanomedicine required to conduct the experiments was too large and could not be produced. Because of this, the Penn-Century Microsprayer was selected as the preferred alternative, at the risk of having a high variability in the regional concentration of the drug in the lungs of the infected animals.

4.5 Summary and Conclusions

The work reported in this chapter shows that Positron Emission Tomography is a very useful tool for the evaluation of the regional distribution of aerosols in the lungs. In our case, radiolabelling of the aerosol using [^{18}F]FDG enabled the investigation of the regional distribution within the lungs, while dissection and gamma counting enabled the determination of the fraction of the dose actually deposited in the lungs after administration using endotracheal insufflation and two different nebulisers. While endotracheal insufflations resulted in ca. 85% of the aerosols reaching the lungs, uniform distribution could not be achieved, most of the dose being deposited in the upper lobes and with high inter-subject variability. Nebulisation using the two different nebulizers resulted in a homogeneous distribution within the lungs, although only <0.1% of the aerosol was actually deposited in the lungs. Both the fraction of the aerosol reaching the lungs and the regional distribution may have a huge impact in putative therapeutic or toxicological studies. Hence, our results confirm that a thoroughly investigation of aerosol generators is of paramount relevance in the pre-clinical context, and that nuclear imaging techniques may offer a valid alternative.

4.6. References

1. Loira-Pastoriza C, Todoroff J, Vanbever R. Delivery strategies for sustained drug release in the lungs. *Advanced Drug Delivery Reviews*. **2014**;75:81-91.

2. Karathanasis E, Ayyagari AL, Bhavane R, Bellamkonda RV, Annapragada AV. Preparation of in vivo cleavable agglomerated liposomes suitable for modulated pulmonary drug delivery. *Journal of Controlled Release*. **2005**;103(1):159-75.

3. Degeorge JJ, Ahn CH, Andrews PA, Brower ME, Choi YS, Chun MY, et al. Considerations of toxicology studies of respiratory drug products. *Regulatory Toxicology and Pharmacology*. **1997**;25(2):189-93.

4. Fuhst R, Runge F, Buschmann J, Ernst H, Praechter C, Hansen T, et al. Toxicity profile of the GATA-3-specific DNAzyme hgd40 after inhalation exposure. *Pulmonary Pharmacology and Therapeutics*. **2013**;26(2):281-9.

5. Duret C, Wauthoz N, Merlos R, Goole J, Maris C, Roland I, et al. In vitro and in vivo evaluation of a dry powder endotracheal insufflator device for use in dose-dependent preclinical studies in mice. *European Journal of Pharmaceutics and Biopharmaceutics*. **2012**;81(3):627-34.

6. Tonnis WF, Bagerman M, Weij M, Sjollema J, Frijlink HW, Hinrichs WLJ, et al. A novel aerosol generator for homogenous distribution of powder over the lungs after pulmonary administration to small laboratory animals. *European Journal of Pharmaceutics and Biopharmaceutics*. **2014**;88(3):1056-63.

7. Lizal F, Jedelsky J, Morgan K, Bauer K, Llop J, Cossio U, et al. Experimental methods for flow and aerosol measurements in human airways and their replicas. *European Journal of Pharmaceutical Sciences*. **2018**;113:95-131.

8. Vaquero JJ, Kinahan P. Positron Emission Tomography: Current Challenges and Opportunities for Technological Advances in Clinical and Preclinical Imaging Systems. *Annual Review of Biomedical Engineering*. **2015**;17:385-414.

9. Dolovich MB. 18F-fluorodeoxyglucose positron emission tomographic imaging of pulmonary functions, pathology, and drug delivery. *Proceedings of the American Thoracic Society*. **2009**;6(5):477-85.

10. Lass JS, Sant A, Knoch M. New advances in aerosolised drug delivery: Vibrating membrane nebuliser technology. *Expert Opinion on Drug Delivery*. **2006**;3(5):693-702.

11. Knoch M, Keller M. The customised electronic nebuliser: A new category of liquid aerosol drug delivery systems. *Expert Opinion on Drug Delivery*. **2005**;2(2):377-90.

12. Patton JS, Byron PR. Inhaling medicines: Delivering drugs to the body through the lungs. *Nature Reviews Drug Discovery*. **2007**;6(1):67-74.

13. Zhang G, Shinohara N, Oshima Y, Kobayashi T, Imatanaka N, Kawaguchi K, et al. Comparison of the local pulmonary distribution of nanoparticles administered intratracheally to rats via gavage needle or microsprayer delivery devices. *Journal of Applied Toxicology*. **2017**;37(4):502-7.

14. Strohl KP, Thomas AJ, St. Jean P, Schlenker EH, Koletsky RJ, Schork NJ. Ventilation and metabolism among rat strains. *Journal of Applied Physiology*. **1997**;82(1):317-23.

15. Brand P, Hederer B, Austen G, Dewberry H, Meyer T. Higher lung deposition with Respimat® Soft Mist™ Inhaler than HFA-MDI in COPD patients with poor technique. *International Journal of COPD*. **2008**;3(4):763-70.

16. Eberl S, Chan HK, Daviskas E, Constable C, Young I. Aerosol deposition and clearance measurement: A novel technique using dynamic SPET. *European Journal of Nuclear Medicine*. **2001**;28(9):1365-72.

17. Behr J, Zimmermann G, Baumgartner R, Leuchte H, Neurohr C, Brand P, et al. Lung deposition of a liposomal cyclosporine a inhalation solution in patients after lung transplantation. *Journal of Aerosol Medicine and Pulmonary Drug Delivery*. **2009**;22(2):121-9.

Chapter 5. Evaluation of the pharmacokinetic properties of novel nanoparticle-based antibiotics after lung administration using Positron Emission Tomography

5.1. Introduction

Nanotherapies based on controlled delivery of drugs entrapped into or attached to nanocarriers (NCs) have emerged as a promising alternative to improve the therapeutic index of drugs by increasing their targeting capacity and accumulation in specific organs, tissues or cells while decreasing potential toxic and off-target side effects. Different nanocarriers are currently used in the clinical field to improve accumulation of drugs in tumours. For example, DaunoXome and Doxil are liposome-based drugs that are nowadays used to treat Kaposi's sarcoma (1, 2) as well as ovarian and breast cancer (1-3). Similarly, micelle-based drugs containing doxorubicin, paclitaxel, or cisplatin are in various stages of clinical trials (4-6). Polymer-based drugs have also experienced similar clinical success; Zoladex and Lupron Depot are small polymer rods and polymer microspheres, respectively. Both can successfully entrap Luteinizing hormone-releasing hormone (LHRH) analogues and are clinically used to treat prostate cancer (7).

The effective transition of novel nanomedicines into the clinical arena demands for a proper assessment of their pharmacokinetic properties. Additionally, as described in the previous chapter, the relationship between the administered dose and the amount of drug deposited in the treated organ, the regional distribution of the nanomedicines in the target organ or tissue and the residence time and/or clearance to the circulatory system need to be assessed for proper therapy planning. For conventional drugs, the pharmacokinetic information can be obtained in pre-clinical tests through classical approaches, e.g. by analysis of biological samples (tissues, fluids) using a combination of techniques such as high performance liquid chromatography (HPLC) and mass spectrometry (MS). In the particular case of nanomedicines, the same approaches can

be utilised to assess the distribution of the entrapped/attached drug. However, tracking the nanocarrier is more challenging, because these are extremely difficult to detect and quantify once distributed in an organism.

One alternative to complement classical approaches at the pre-clinical level consists of radiolabelling the NC, the drug, or both using positron or gamma emitters. Hence, after the administration of the radiolabelled nanomedicines, images at different time points can be acquired in order to determine the regional distribution of the labelled entities at the whole body level at different time points, providing full pharmacokinetic data while minimizing the number of experimental animals (8). This information concerns not only to the targeted organ; because whole body images can be acquired, information about translocation to remote organs or elimination routes can be obtained. Also, blood samples can be withdrawn during image acquisition, providing information about translocation of the labelled species to the blood stream. Importantly, the techniques are fully translational to the clinical setting. In other words, the same experimental techniques used in the preclinical scenario can be applied to humans, because nuclear imaging techniques are minimally invasive and only require the administration of a sub-pharmacological amount of the substance under investigation.

As mentioned in chapter 2, the work conducted in the current PhD project is framed in the context of the EU-funded project PneumoNP, aiming at developing new pulmonary-administered nanodrugs to combat antibiotic resistant lung infections. When the lung is the target organ, the use of nuclear imaging modalities faces some difficulties which need to be overcome. One of the main drawbacks to achieve accurate quantification *in vivo* is the breathing-related motion of the subject during image acquisition. Such movement hampers accurate location of the radioactive signal and hence compromises quantification, especially when small animals are investigated. Of note, gated imaging can be applied to correct for this; alternatively, in the preclinical setting, excision of the organs of interest and *ex vivo* imaging can mitigate this problem, at the cost of animal sacrifice. Additionally, resolution of nuclear imaging is usually poor (around 1 mm in the centre of the field of view for preclinical

systems, close to 5 mm for clinical systems). If higher resolution images are required, tissue dissection, slicing and evaluation using autoradiography can provide accurate information about regional distribution of the administered drug with a resolution close to 50 µm. Imaging studies can be combined with dissection and gamma counting to get more accurate quantitative information about the actual amount of radioactivity accumulated in the different organs.

In the frame of the PneumoNP project, all the above mentioned techniques (*in vivo* imaging, *ex vivo* imaging, dissection and gamma counting) have been used and combined in order to evaluate the pharmacokinetic properties of two novel antimicrobial peptides (AMPs) developed by partners Adenium Biotech (Denmark) and SetLance (Italy), that have shown activity against *Klebsiella pnemoniae*, a multidrug resistant (MDR) Gram-negative bacteria (9, 10); These antibacterial drugs have a positive net charge that allows them to interact selectively with anionic bacterial membranes and with other negatively charged structures, such us lipopolysaccharide (LPS), lipoteichoic acid (LTA) and DNA. Their mechanism of action is normally through specific binding to bacterial surfaces, by which they provoke cell penetration and in some cases inhibition of metabolic pathways.

Both AMPs (identified as AA139 and M33) were modified by the corresponding partners by incorporating one tyrosine residue to enable subsequent labelling with a positron emitter. In this work, radiolabelling was achieved by aromatic iodination using Iodine-124 (positron emitter with a half-life of 4.18 days). The labelled peptides were then administered to wild type (WT) rats by endotracheal insufflation. The pharmacokinetic properties and the residence time of the AMPs in the lungs were assessed in two different scenarios: a) when they were administered in their “free” form and b) conjugated with polymeric NPs or with lipid-core micelles (MC) acting as the nanocarriers. Moreover, the residence time in the lungs of “empty” polymeric NP and its parent polymer was also evaluated (Figure 5.1).

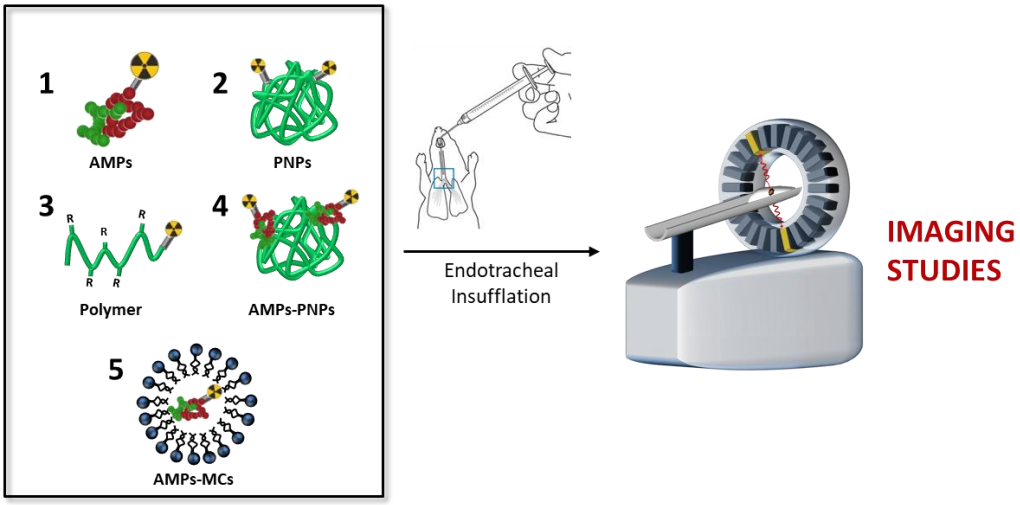

Figure 5.1. Summary of all the radiolabelled species that were evaluated by imaging studies after endotracheal insufflation. 1: AMPs (AA139 and M33); 2: Polymeric NPs (empty nanocarrier); 3: polymer; 4: AMPs-PNPs nanosystems (AA139-PNPs and M33-PNPs); 5: AMPs-MCs nanosystems (AA139-MCs and M33-MCs).

5.2. Objectives

The specific objectives of this work are:

1. To develop labelling strategies for the incorporation of positron emitters in the selected antimicrobial peptides.
2. To determine the residence time in the lungs of radiolabelled antimicrobial peptides, either administered as “free peptides” or combined with selected nanocarriers, after aerosol administration.
3. To develop labelling strategies for the incorporation of gamma emitters in selected nanocarriers.
4. To evaluate the residence time in the lungs of the selected nanocarriers after aerosol administration.

5.3. Experimental Part

5.3.1 General remarks

The AMPs were provided by partners Adenium Biotech (Denmark) and SetLance (Italy), while polymeric NPs and the parent polymer were provided by partner CIDETEC. Hence, the preparation of these AMPs and carriers is not described in this PhD thesis. The technology for the preparation of the micelles was developed by partner UU (The Netherlands) and transferred to CIC biomaGUNE, because the incorporation of the radiolabelled AMP required *in situ* preparation of the nanosystems. For this particular case, a brief description of the preparation protocol will be included in the corresponding section.

5.3.2 Radiolabelling

5.3.2.1. Radiolabelling of polymeric nanoparticles (PNPs) and parent polymer

Gallium-67 (^{67}Ga) was obtained from Mallinckrodt Medical, B.V. (Le Petten, The Netherlands) as a citrate salt. Prior to radiolabelling reactions, ^{67}Ga citrate was converted into ^{67}Ga chloride using a modified procedure reported previously (11). In brief, the ^{67}Ga citrate solution was first eluted through two silica cartridges connected in series (Sep-Pak® Silica Plus Light, Waters Co., Milford, MA, USA) at a constant flow rate of 0.1 mL/min. The cartridges were dried with air for 1 minute and washed with ultrapure water (5 mL, obtained from a Milli-Q® Purification System, Millipore®, Merck KGaA, Darmstadt, Germany). Desorption of ^{67}Ga ions was finally achieved by elution with 0.1 M aqueous HCl solution (1 ml) at a flow rate of 0.1 ml/min. The eluate was collected in different fractions (ca. 100 µL each) and those fractions containing the maximum activity concentration (typically fractions 4-5) were used in subsequent labelling experiments.

Radiolabelling of PNPs and parent polymer was performed by incubation of the NODA-functionalized nanoparticles (PNP-F-NODA) or linear polymer with $^{67}GaCl_3$. In a typical experiment, 50 µL of PNPs or polymer solution (1 mg/mL) and 50 µL of $^{67}GaCl_3$ (ca. 37 MBq) were incubated in sodium acetate buffer solution (0.2M, pH = 4.2, 200 µL) at

25°C for 45 min. After incubation, the crude material was purified by centrifugal filtration using Millipore Amicon® Ultra filters (3 kDa cut-off). The resulting precipitate was washed three times with sodium acetate buffered solution to remove unreacted ^{67}Ga species and the amount of radioactivity in the pellet, the supernatant, and the washings was determined by a dose calibrator (CPCRC-25R, Capintec Inc., NJ, USA). Labelling efficiency (expressed in percentage) was calculated as the ratio between the amount of radioactivity in the filter and the total amount of radioactivity in all fractions. Finally, the nanoparticles or polymer were suspended in 0.2 M sodium acetate buffer solution (pH 4.2). Radiochemical yield was calculated as the ratio between the amount of radioactivity in the resuspended fraction and the starting amount of radioactivity.

5.3.2.2. Radiochemical stability of PNPs and parent polymer

Radiolabelled entities prepared as described above were incubated in sodium acetate buffered solution at 37 °C using a digital block heater. At different time points (1, 3, 24, 48, 72 and 144 hours) samples were withdrawn and the amount of radioactivity was measured. The ^{67}Ga-radiolabelled PNPs and polymer were filtered, washed twice with ultrapure water, and the amount of radioactivity in the filter and the filtrate/washings was measured. The radiochemical stability was calculated as the percentage of radioactivity in the pellet with respect to the total amount of radioactivity (pellet + filtrate + washings).

5.3.2.3. Radiolabelling of AMPs

Experiments were conducted with peptides M33 (provided by partner SetLance) and AA139 (provided by Adenium Biotech). The radio-iodination of the peptides was carried out by electrophilic aromatic substitution on the tyrosine residues. With that aim, a solution of the peptide (50 µg/50 µL) was incubated with Na[^{124}I]I in 0.2 M sodium acetate buffer solution (50 µL, pH 5.5) for 2 hours at 25°C in the presence of Iodobeads®. In case of AA139 peptide, the crude reaction was purified by retention in a C-18 cartridge (Sep-Pak® Light, Waters) and subsequent elution using 0.1% aqueous TFA solution/methanol 20/80 (1 mL). The solvent was evaporated and the residue

reconstituted with 0.2 M sodium acetate buffer solution (300 µL, pH 5.5). The peptide M33 was purified by size exclusion chromatography (SEC) using Illustra™ Nap™-5 Sephadex™ columns G-25 DNA grade (GE Healthcare, USA) columns, preconditioned with a sodium buffer solution (10 mL, 0.02 M, pH=5.5). In both cases, chemical and radiochemical purity were determined by radio-HPLC, using a Mediterranean Sea 18 column (4.6 x 150 mm, 5 µm) as the stationary phase and 0.1% solution of TFA in water (A) and pure methanol (B) as the mobile phase. The following gradient was used for the M33 peptide; initial: A-60% B-40%; 4 min: A-60% B-40%; 14 min: A-20% B-80%; 18 min: A-60% B-40%; 20 min: A-60% B-40%. Injected volume was 20 µl. The gradient used for the AA139 peptide was as follows; initial: A-90% B-10%; 4 min: A-85% B-15%; 6 min: A-75% B-25%; 10 min: A-75% B-25%: 16 min: A-5% B-95%; 18 min: A-5% B-95%; 20 min: A-90% B-10%; 22 min: A-90% B-10%.

Radiochemical stability of the labelled AMPs was assessed by incubation in different media at 37°C. At different time points, samples were withdrawn and analysed by HPLC using the experimental conditions described above. Radiochemical stability was directly calculated from chromatographic profiles.

5.3.2.4. Preparation of AMP-NP conjugates

Preparation of two different AMP-NP conjugates or nanosystems (NSs) was carried out by combining previously radiolabelled AA139 or M33 peptides (following the procedure described above) with either PNPs provided by CIDETEC or lipid-core micelles prepared *in situ*. The protocols to efficiently attach or encapsulate AMPs to/into different NCs were developed by partners CIDETEC (AMP-PNPs) and University of Utrecht (AMP-micelle) and then transferred to our laboratory. These protocols are briefly described below.

Combination of AMPs and PNPs

Partner CIDETEC optimised a protocol to efficiently load AMPs to PNPs. At physiological pH these NCs, which have carboxylic acid groups attached on their surface, are in fact negatively charged and thus it is possible to combine them with

positively charged AMPs (AA139 and M33) by electrostatic interactions (Figure 5.2.). During optimization of the experimental protocol, different concentrations of peptides were added to water-based dispersion of nanoparticles to determine the limit of loading in terms of stability and maximum peptide content in the NSs. After incubation, the solutions were purified by filter centrifugation using Millipore Amicon® Ultra filters (5000 MWCO) and the presence/absence of peptide in the filter and filtrate was assessed by UV-Vis. Moreover, the incorporation of AMPs to PNPs was confirmed by Dynamic Light Scattering (DLS) and Z-potential (Z-pot) measurements. The hydrodynamic radius of the nanoparticles and NSs was measured on a Zetasizer Nano ZS, ZEN3600 Model (Malvern Instruments Ltd) by Dynamic Light Scattering (NIBS®) technique. The scattering angle was fixed at 90°. A filtered (0.22µm) water dispersion of the nanoparticles at a concentration of 0.3 mg/mL was used and the experiments were performed at 25 °C in triplicate. The Z-pot measurements were also performed by using this instrument at a concentration of 1 mg/mL in 1mM NaCl solution without 0.22 µm filtration.

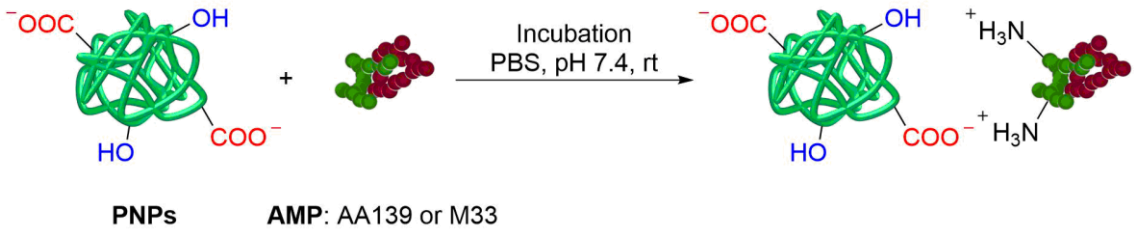

Figure 5.2. Electrostatic coupling of AMPs to PNPs.

Attachment of radiolabelled peptides to the polymeric NPs was carried out following the exact instructions provided by CIDETEC. In brief, the corresponding amount of labelled peptide (^{124}I-labelled AA139 or M33, 50 µg/300 µL) was incubated with polymeric NPs (500 µg/500 µL) at 25 °C for 15 hours. Then, the crude of reaction was purified by centrifugal filtration using Millipore Amicon® Ultra filters (5000 MWCO) to eliminate the unbound peptide.

Combination of AMPs and micelles

In a similar manner, partner Utrecht University investigated the maximum peptide and lipid (DSPE-PEG$_{2000}$) concentration required for efficient encapsulation. A DSPE-PEG$_{2000}$

lipid film was hydrated (see Figure 5.3) with different concentrations of peptides in PBS (10 mM, 0.8% NaCl, pH 7.4), and the excess of free peptide was removed from micelles by dialysis. Finally, the peptide concentration was determined by UPLC.

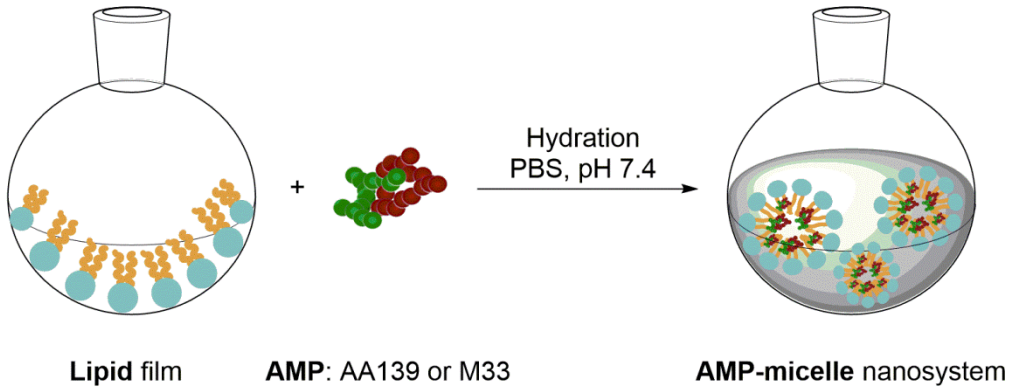

Figure 5.3 Formation of AMP-micelle nanosystems by peptide encapsulation.

Bearing in mind that in our case peptides were radiolabelled with Iodine-124 ($t_{1/2}$=4.18 days) and that dialysis requires long time of incubation, a faster method for NS purification was employed (Figure 5.4). In fact, purification was achieved by size exclusion chromatography (SEC), using Illustra™ Nap™-5 Sephadex™ G-25 DNA grade columns (GE Healthcare, USA), preconditioned with ultrapure water (18MΩcm). The eluted product was collected in 100 µL fractions and those containing the highest concentration of radioactivity (usually in the initial fractions) were diluted with physical saline solution and used for *in vivo* experiments (*vide infra*). Incorporation ratios were calculated as the ratio between the amount of radioactivity present in the NC-AMP conjugates and the starting amount of labelled AMP.

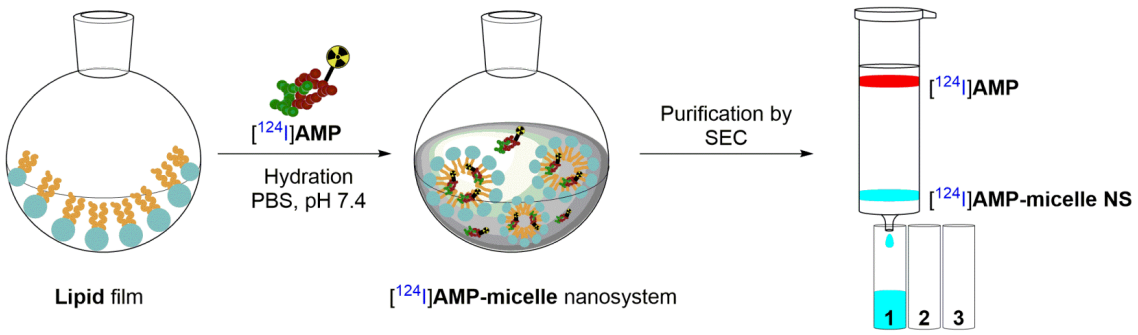

Figure 5.4. Formation of radiolabelled AMP-micelle nanosystems by encapsulation of [^{124}I]AMPs within micelles.

5.3.3 Animal Experiments

5.3.3.1. General considerations

All animal experiments were performed in accordance with the Spanish policy for animal protection (RD53/2013), which meets the requirements of the European Union directive 2010/63/UE regarding the protection of animals used in experimental procedures. The procedures were approved by the Ethical Committee of CIC biomaGUNE and authorized by the regional government.

5.3.3.2. Administration of the radiolabelled NCs, AMPs and AMP-NC conjugates

Female Sprague Dawley rats (Janvier, Le Genest-Saint-Isle, France) were used. Rats were anesthetized with 3-5% isoflurane (IsoFlo®, Abbott Laboratories) in pure O_2 for 5 minutes to ensure deep sedation. Once animals were under sedation, radiolabelled entities were administered by endotracheal insufflation using a Penn-Century MicroSprayer® Aerosolizer (FMJ-250 High Pressure Syringe Model, Penn-Century. Inc. Wyndmoor, USA). A small animal Laryngoscope (Model LS-2, Penn-Century. Inc.) was used for correct visualization of the epiglottis, ensuring a correct positioning of the tip just above the carina. A pre-defined volume of radiolabelled solutions (50 µL, established by using spacers in the syringe plunger) was administered (amount of radioactivity around 1.85 MBq). Immediately after, rats were submitted to *in vivo* imaging studies (see below). Rats administered with ^{67}Ga citrate solution or [^{124}I]NaI in saline solution were used as controls.

5.3.3.3. In vivo imaging experiments of selected NCs: PNPs and its corresponding parent polymer

Immediately after administration of either the radiolabeled PNPs or the parent polymer, and without recovering from sedation, animals were positioned in an eXplore speCZT CT preclinical imaging system (GE Healthcare, USA) to perform *in vivo* studies. Body temperature was maintained with a homeothermic blanket control unit (Bruker BioSpin GmbH, Karlsruhe, Germany) to prevent hypothermia, and a SPECT scan was acquired for 30 minutes. Animals were then recovered from sedation and returned to their cages. Imaging sessions were repeated at t = 24, 48 and 72 hours after

administration. In these cases, anaesthesia was induced by inhalation of 3-5% isoflurane (IsoFlo®, Abbott Laboratories) in pure O_2 as the carrier, and maintained using 1% - 2% isoflurane during image acquisition. After each SPECT scan, a CT acquisition was performed to provide anatomical information of each animal and enable unequivocal localization of the radioactive signal.

The SPECT images were reconstructed using a ordered-subset expectation maximization (OSEM) iterative algorithm (3 iterations/3 subsets, 128 x 128 x 32 array with a voxel size of 0.55 x 0.55 x 2.46 mm^3), whereas for the CT a cone beam filtered back-projection a Feldkamp algorithm (437 x 437 x 993 array with a voxel size of 0.2 x 0.2 x 0.2 mm^3) was used. After reconstruction, images were quantified using πMOD analysis software (version 3.4, PMOD Technologies Ltd.). Volumes of interest (VOIs) were manually drawn in different regions of the lungs on the CT images and translated to the SPECT images. The relative concentration of radioactivity in the different VOIs was finally determined.

5.3.3.4. In vivo imaging experiments of selected AMPs and NSs

Following a similar procedure to that followed for the *in vivo* evaluation of NCs, PET-CT imaging studies were carried out to investigate the residence time in the lungs of selected AMPs, both in their free form and as a part of the NSs. With that aim, immediately after administration of the radiolabelled species and without recovering from sedation, animals (n=4 per compound) were placed in an eXploreVista-CT small animal PET-CT preclinical imaging system (GE Healthcare, USA) to perform *in vivo* studies. Animals were then recovered from sedation and returned to their cages. Imaging sessions were repeated at t = 3, 6, 9, 15 and 24 hours after administration. After image reconstruction using filtered back projection reconstruction algorithm, images were quantified using πMOD software. Volumes of interest (VOIs) were manually drawn in the lungs on the CT images and translated to the PET images. Since absolute quantification is possible in PET, the exact amount of radioactivity in the different VOIs was assessed at all time-points for all the different species and the values were used to determine residence time of the labelled species in the lungs.

5.3.3.5. Ex vivo experiments of selected NCs: PNPs and parent polymer

Since absolute quantification in SPECT-CT is extremely challenging, *ex vivo* experiments were also carried out to confirm the results obtained *in vivo*. With that aim, at pre-defined time points after administration of the labelled species (t=0, 72 and 144 hours) animals were sacrificed by exsanguination followed by perfusion with saline solution. The lungs were harvested, dissected into different lobes and the amount of radioactivity in each lobe and the trachea was accurately determined by gamma counting (WIZARD2 Gamma Counter, Perkin Elmer, Waltham, USA).

5.4. Results and discussion

5.4.1. Radiolabelling

5.4.1.1. Radiolabelling of polymer nanoparticles (PNPs) and the corresponding parent polymer

Radiolabelling of PNPs and parent polymer was approached by formation of a radiometal-chelator complex. Under optimized experimental conditions (T = 25°C, t = 45 min, pH = 4.2), radiochemical yields of 51%±5% and 84%±4% (non-decay corrected) could be achieved for PNPs and its corresponding linear parent polymer (respectively).

The labelling strategy followed for the incorporation of ^{67}Ga into PNPs and the corresponding linear parent polymer, based on the formation of a chelator-^{67}Ga complex, has been previously described in the literature and applied to the radiolabelling of small peptides and also NPs. In the context of NPs, one of the first examples found in the literature was reported by Hwang *et al (12)*, who prepared cobalt–ferrite nanoparticles surrounded by fluorescent rhodamine within a silica shell matrix and functionalized with an aptamer targeting nucleolin, a cellular membrane protein highly expressed in cancer. The resulting particles were further decorated with a bifunctional chelator containing NOTA and labelled with ^{67}Ga. The authors reported a labelling efficiency of 40% as measured by quantitative TLC analysis and good stability of the labelled particles in mouse serum. In our case, slightly superior labelling efficiencies were achieved. Noteworthy, such labelling efficiency could be increased by

just increasing the amount of NPs to be incubated with the radionuclide. However, this was considered as unnecessary and, to a certain extent, not convenient, due to two main reasons: First, the labelling efficiency for both the PNPs and the parent polymer was sufficient to approach *in vivo* studies in rodents. Second, it has to be noted that the purification method employed cannot separate the labelled PNPs (or polymer) from the unlabelled analogues. Hence, increasing the amount of PNPs or polymer leads to a significant decrease in the final molar activity, which ultimately results in a higher mass dose injected into the animal. In our case, the experimental conditions ensured an injected dose <50 μg to the animal, which produced no apparent side or toxicological effects on the animals.

Stability studies of the radiolabelled PNPs and parent polymer were performed by incubation in buffered saline solution. Ideally, the stability of the labelled species should be determined *in vivo.* Indeed, the determination of the stability of the labelled species is paramount because detachment of the radionuclide may have a significant impact on the conclusions obtained from imaging studies. In the context of small molecules or even macromolecules such as proteins or antibodies which are administered intravenously, such information can be obtained by administration of the species under investigation followed by blood sampling, isolation of the plasma and further analysis. However, this strategy is difficult to apply in the case of NPs, mainly due to the fact that NPs are not easily isolated from biological samples. Because of this, alternative strategies have been reported, being the most commonly used the incubation of NPs in fluids that mimic the *in vivo* environment such as water, buffers, saline, serum, plasma or solutions containing amino acids, proteins or complexing agents. Typically, the radiochemical stability of NPs labelled using the formation of a chelator-radiometal complex and aimed to be intravenously administered, is investigated by incubation in a solution of a complexing agent such as DTPA (13), as this can act as a sequestrator of the radiometal, mimicking thus the presence of complexing proteins present in blood. In our case, because the labelled PNPs or polymers were administered by endotracheal insufflation, *in vitro* stability studies in a buffered solution were anticipated as sufficient to predict the stability of the radiolabel

in vivo. Of note, *in vivo* control experiments were performed with "free gallium" to ensure that the distribution pattern observed after the administration of ^{67}Ga-PNPs or polymer was not significantly affected by the detachment of the label (*vide infra*).

5.4.1.2. Radiolabelling of AMPs

Radiolabelling of peptides can be achieved by following mainly three different strategies: Radioiodination, radiofluorination and radiometallation.

Radioiodination is probably the most widely used strategy and can be achieved following three different methods: The easiest one is the incorporation of the radioiodine by *in situ* oxidation of the anionic species (I^-) using an oxidizing agent in solution, e.g. chloramine-T (14), and subsequent electrophilic substitution in the aromatic ring of tyrosine residues. This methodology provides high incorporation yields, although it cannot be always applied because not all peptides contain tyrosine residues. The main drawback of this strategy is that is very unspecific, because no control exists on the position in which the iodine atom is incorporated, the product mixture obtained is often complex and requires extensive HPLC purification (15). Additionally, the strong oxidizing character of chloramine-T can lead to the oxidation of sensitive amino acids. This side effect can be mitigated by using milder oxidants such as Iodogen (16), which is currently commercially available. Alternatively to direct radioiodination, indirect methods consisting of the covalent attachment of a pre-labelled group to one lysine residue have been developed; the most widely used conjugation reagent is radioiodinated N-succinimidyl 3-(4-hydroxyphenyl)propionate (Bolton-Hunter reagent) (17). By following this approach, multiple products can be formed by the reaction with the chain end and/or a variety of side chains and usually time-consuming purification methods are required when single species are to be isolated. Finally, if the peptide under investigation already contains a iodine atom, isotopic exchange can be conducted (18). A summary of these three strategies is summarised in Figure 5.5.

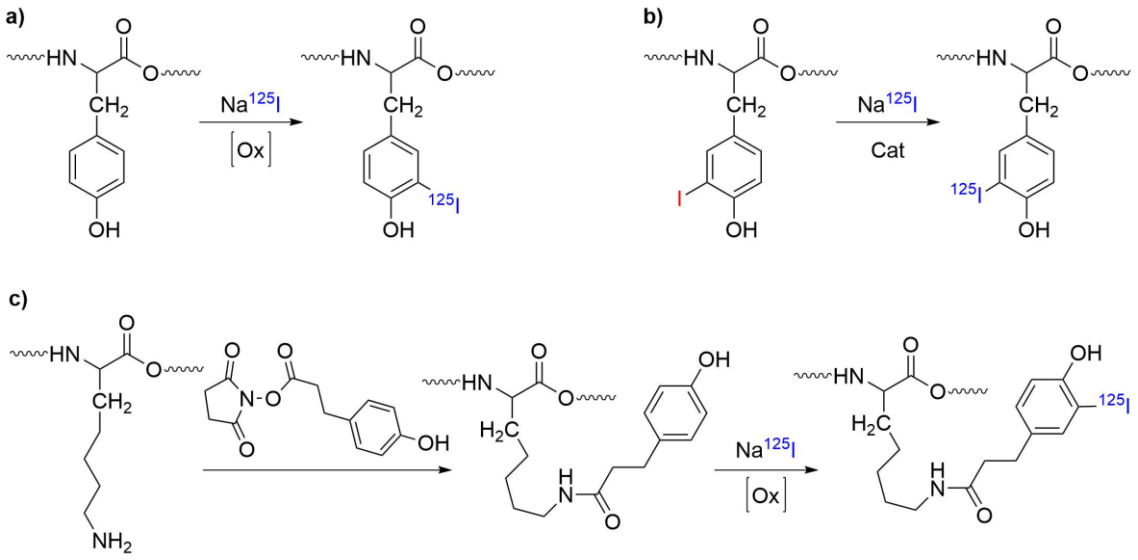

Figure 5.5. Different strategies for the radioiodination of peptides: a) electrophilic substitution in the aromatic ring of tyrosine residues; b) isotopic exchange and c) indirect radioiodination by covalently binding a pre-labelled group (Bolton-Hunter reagent) to lysine residues.

In our case, both peptides M33 and AA139 were designed to contain a tyrosine residue in a non-active region of the peptide sequence, and hence the direct radioiodination was anticipated as the easiest and more efficient methodology. Indeed, by following direct radioiodination in the presence of the oxidizing agent resulted in overall decay-corrected radiochemical yields after purification of 36±9% and 62±2%, respectively, when ^{124}I was used. Molar activities in both cases were in the range 0.5-1.5 GBq/µmol at the end of the synthesis. Both the radiochemical yield and the molar activity were appropriate to approach further steps, either direct *in vivo* investigation or attachment to/entrapment into the NCs.

It is worth mentioning that stability studies for M33 by incubation in saline solution showed that 20% of the parent peptide was degraded after 1 hour, and this value increased up to 60% at t=48 hours. However, the labelled peptide showed much higher stability in 0.1% TFA in water/methanol (20/80). In this media, more than 95% of the parent peptide remained unchanged during 48 hours (Figure 5.6, left), and hence this media was selected to store the labelled peptide until further use. The peptide AA-139 showed good stability in sodium acetate buffer, pH=5.5; see Fig. 5.6, right), with

almost all the radioactivity accounting for the labelled peptide even after 2 days of incubation.

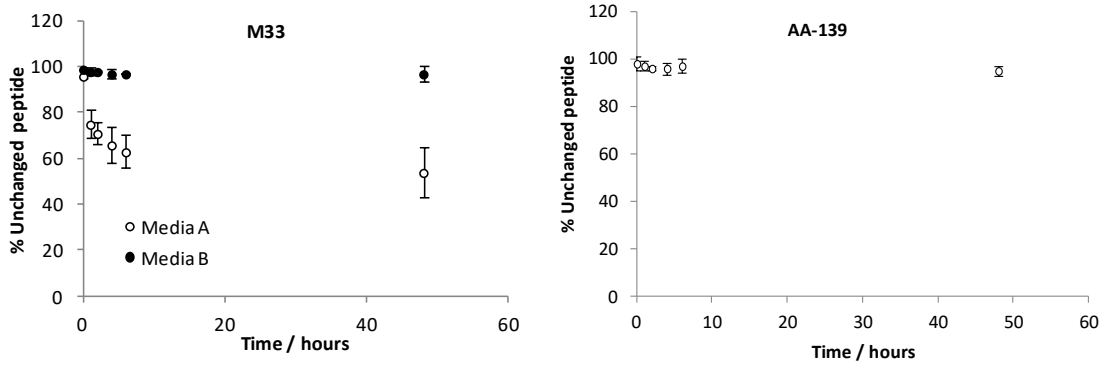

Figure 5.6 Left: Stability of ^{124}I-labelled M33 as determined by HPLC in different media; Media A: PBS 0.02M, pH=7.4; media B: 0.1 % solution of TFA in water/methanol (20/80); right: Stability of ^{124}I-labeled AA-139 as determined by HPLC in sodium acetate buffer at pH = 5.5. Results are expressed as percentage of unchanged labelled peptide as mean ± standard deviation, n=3.

5.4.1.3. Preparation of AMP-NP conjugates

As already stated in the introduction of this chapter, we can find many examples of nanomedicines (combinations of drugs and nanoparticles) that are already being used in the clinics, and others that are in advanced clinical stages. These nanoformulations can be prepared by mainly three different strategies: encapsulation, covalent and non-covalent binding. Indeed, the biological fate of the drug will vary depending on how the drug is attached to the NC. In this regard, we can find different studies in the literature. For example, Kim S.W. *et al* identified that covalently conjugated, non-covalent polyethylene glycol coated and encapsulated nanodrugs selectively influenced drug uptake and the intracellular and extracellular trafficking of cancer cells (19). They prepared three different types of nanodrugs to investigate their effect on intracellular dynamics. More precisely, encapsulated-doxorubicin (DOXOVES®), PEG-coated-DOX (non-covalently bound to carbon nanotubes) and covalently conjugated DOX (using amide bonds with carbon nanotubes) were used in the study. All the nanoformulations exhibited high drug stability (less than 20% drug release until 288 hours) under extracellular physiological conditions (PBS, pH 7.2). In contrast, under intracellular-like conditions (acidic pH and in presence of active enzymes) PEG coated

drugs were abruptly released (nearly 100% of the drugs) from the carbon nanotubes after 2 hours of incubation. On the other hand, both covalent conjugation and liposomal encapsulation exhibited relatively stable drug release (i.e. less than 50% until 288 hours). Regarding nanodrug uptake in cancer cells, authors observed greater uptake in covalently conjugated doxorubicin than liposomal encapsulated or PEG coated.

As explained above, in our project the strategies that were followed to incorporate the AMPs to different nanocarriers were by electrostatic interactions (combination of AMPs and PNPs) and by encapsulation (combination of AMPs and micelles).

Combination of AMPs and PNPs

Electrostatic interactions have been indicated as one of the potentially important physical forces involved in competitive binding. In this way, many peptides and proteins have been attached to NPs following this strategy. For example, Hildebrandt *et al.* prepared superparamagnetic iron-oxide nanoparticles (SPIO) coated with dextran and functionalized with peptides by electrostatic interactions (20). Small peptides containing a specific recognition sequence and amino acids that were positively charged under physiological conditions were bound to the negatively charged surface of a modified dextran. The binding was estimated by size distribution and fluorescence measurements (peptides contained a fluorescent dye). Similarly, Wang *et al.* also investigated the contribution of electrostatic interactions to protein-AuNP binding by studying the pH-dependent binding behavior of two proteins, GB3 and ubiquitin (21). When pH was increased from pH 5 to pH 8.3 and the net charge of proteins went from positive to neutral, both proteins exhibited a decrease in adsorption capacity.

In our case, we also decided to follow this strategy to bind the AMPs to polymeric NPs by electrostatic interactions. According to the results obtained by CIDETEC, the maximum loading was established at 0.1 mg AA139/mg PNPs and 0.140mg M33/mg PNPs. In case of AA139-PNPs based nanosystem, an increase from -22 mV (unloaded PNPs) to -18 mV (AA139-PNPs) was observed in the Z-potential. DLS measurements indicated a final hydrodynamic diameter of the NS of 100-130 nm. Regarding M33-PNP

nanosystem, Z-potential measurements showed an increase from -22 mV to -13 mV and a final hydrodynamic diameter of 125-250 nm after M33 peptide incorporation.

With these results, previously radiolabelled AA139 and M33 were efficiently attached to PNPs. When the relative amount AMP/NP was set to 1/10, almost quantitative attachment of the peptides to the NP was observed. Radiochemical yields after purification close to 60% (referred to pure labelled peptide) could be achieved.

Combination of AMPs and micelles

Peptide based drugs are an important class of therapeutic agents but their development into commercial products is often hampered due to their inherent physico-chemical and biological instabilities. Issues such as aggregation, oxidative and hydrolytic degradation *in vitro* on one hand, and rapid proteolytic degradation and renal elimination *in vivo* on the other hand, impede their development as therapeutic agents. In addition, poor permeability across biological membranes and degradation in the gastrointestinal tract significantly decrease the oral bioavailability of most peptide drugs and require parenteral administration (22, 23). This issue combined with their short biological half-lives requires frequent dosing that make peptide products less convenient for patients. All these pitfalls can be overcome by using phospholipid micelles as carriers. Phospholipids are an integral part of cell membrane and therefore when used in delivery systems, are considered safe and non-immunogenic. These lipids when conjugated with PEG become more soluble in water and when dispersed in aqueous media above a certain concentration form micelles. Unlike liposomes, micelles are self-assemblies of amphiphilic molecules that arrange themselves such that the hydrophobic parts of the molecule are clustered together and directed away from aqueous environment, while the hydrophilic domains are directed toward water.

Phospholipid micelles such as those prepared using PEGylated lipids like DSPE-PEG_{2000} (distearoyl-phosphatidylethanolamine chemically conjugated to PEG_{2000}) are also called sterically stabilized micelles (SSM) and can be used as delivery systems for small molecule drugs (solubilized within the hydrophobic core of the micelles) or peptide drugs (postulated to reside in the PEG palisade of micelles). Several examples of

peptide drugs conjugated with sterically stabilized micelles can be found in the literature (24-33).

In our work, we have used DSPE-PEG_{2000} to encapsulate the antimicrobial peptides, following the procedure provided by Utrecht University. According to their protocol, the maximum lipid concentration at which all the DSPE-PEG_{2000} lipids were solubilized in PBS buffer to form micelles was around 10-15 mM. At this lipid concentration, the maximum loading efficiency (99% ± 2) was achieved at a 7.7 mg/mL AA139 peptide concentration, resulting in a molar ratio of peptide: lipid = 1:5. In addition, stability studies indicated that above 95% of peptide was still encapsulated within micelles after one week of incubation at 4 °C.

Employing the same molar ratio of radiolabelled peptide (both AA139 and M33): lipid (1:5), radiolabelled AMPs were successfully encapsulated within micelles. After purification of the crude of reaction by SEC, incorporation ratios were found to be higher than 95%.

5.4.2. Animal Experiments

5.4.2.1. In vivo imaging experiments of selected NCs: PNPs and its corresponding parent polymer

In order to investigate the biological half-life of polymeric nanocarriers in the lungs, SPECT-CT images were acquired at different time points after administration to have a visual and intuitive idea about the residence time of each radiolabelled species within the lungs (Figure 5.7).

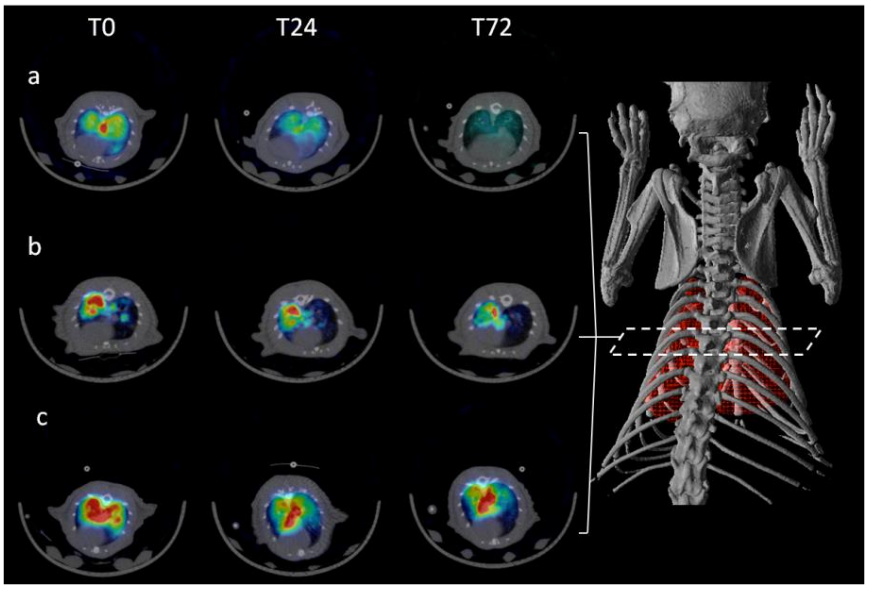

Figure 5.7. SPECT-CT axial images obtained after administration of ^{67}Ga-Citrate (a), ^{67}Ga-Polymer (b), ^{67}Ga-PNPs (c) by endotracheal insufflation at 0, 24 and 72 hours.

Despite the regional distribution of the radioactivity was not completely homogenous, the presence of signal could be detected in almost the whole lungs at all times. The residence time of ^{67}Ga-SCPNs and ^{67}Ga-Polymer was evaluated and compared with ^{67}Ga-Citrate. As it can be seen in the images obtained at 72 hours after administration, only a small fraction of the administered citrate was still left within the lungs, whereas a significant fraction of PNPs and the corresponding linear polymer could still be detected in this organ. Since quantification of radioactivity with SPECT is not possible and images were only interpreted qualitatively, *ex vivo* studies were carried out to determine the amount of radioactivity that was still left at 3 and 6 days after administration (see below, section 5.4.2.3).

5.4.2.2. In vivo imaging experiments of selected AMPs and NSs

Similar to the previous study, PET-CT image sequences were obtained for all the studied AMPs and NSs (see Figure 5.8 for example of the biodistribution patterns of free [^{124}I]AA139 peptide and [^{124}I]NaI, used as control, at different time points).

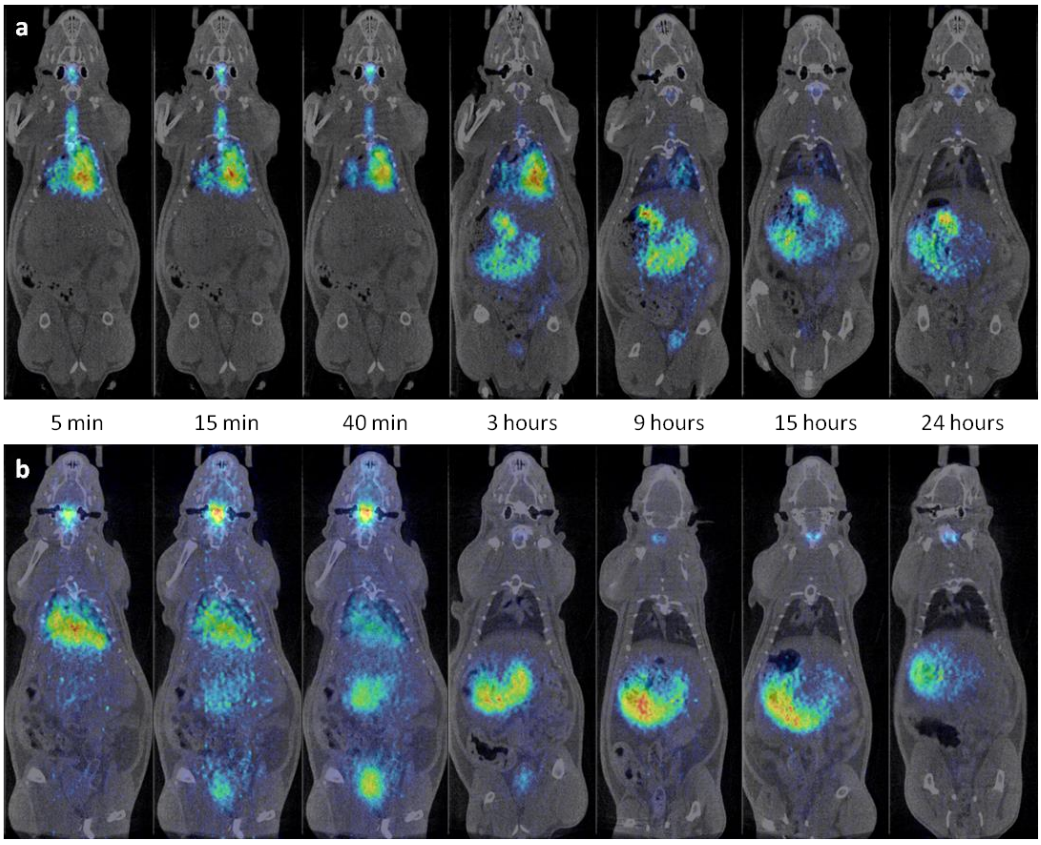

Figure 5.8. PET-CT coronal images obtained at different time points after administration by endotracheal insufflation of [^{124}I]AA139 (a) and [^{124}I]NaI (b). PET images have been corregistered with CT images of the same animals for accurate location of the radioactive signal.

In this particular example, just by visual inspection of the sequences, it was evident that the biodistribution patterns of the two species were different. The residence time of the peptide in the lungs seemed to be significantly higher than radioactive sodium iodide's ([^{124}I]NaI). Indeed, three hours after administration almost no signal was observed within the lungs when [^{124}I]NaI was administered, whereas a significant fraction of peptide was still visible at the same time-point. The elimination pathways of these two species suggested excretion via urine and the gastrointestinal tract.

Quantification results confirmed the trends observed in these *in vivo* sequences. The amount of radioactivity at each time point was fit to a mono-exponential decay equation and in this way half-lives of each compound were determined. As seen in Figure 5.9 (upper row), the residence time of AA139 ($t_{1/2}$= 1.71 hours) was slightly

increased when coupled to polymeric NPs ($t_{1/2}$= 2.08 hours). When the same peptide was encapsulated within a micelle, its biological half-life in the lungs increased significantly, up to 3 hours.

Results obtained with M33 peptide (Figure 5.9, lower row) were quite similar. In this case, the half-life of the free peptide in the lungs was found to be slightly shorter than that obtained for AA139's ($t_{1/2}$= 1.08 hours). When M33 was attached to polymeric NPs, the radioactivity values obtained at different time points did not fit to a mono-exponential decay equation (red line fitting) but to a bi-functional equation. Indeed, this was a two phase decay system where the half-life of the first phase was 1.12 hours (almost the same as for free M33's) while values for the second phase were close to 13 hours. These results suggest that not the whole amount of peptide was attached to the NPs, and a fraction of the peptide was "free" or loosely bound, behaving almost as the free peptide. Finally, when M33 was trapped within a micelle, its half-life was close to three hours. All half-life values are summarised in Figure 5.10.

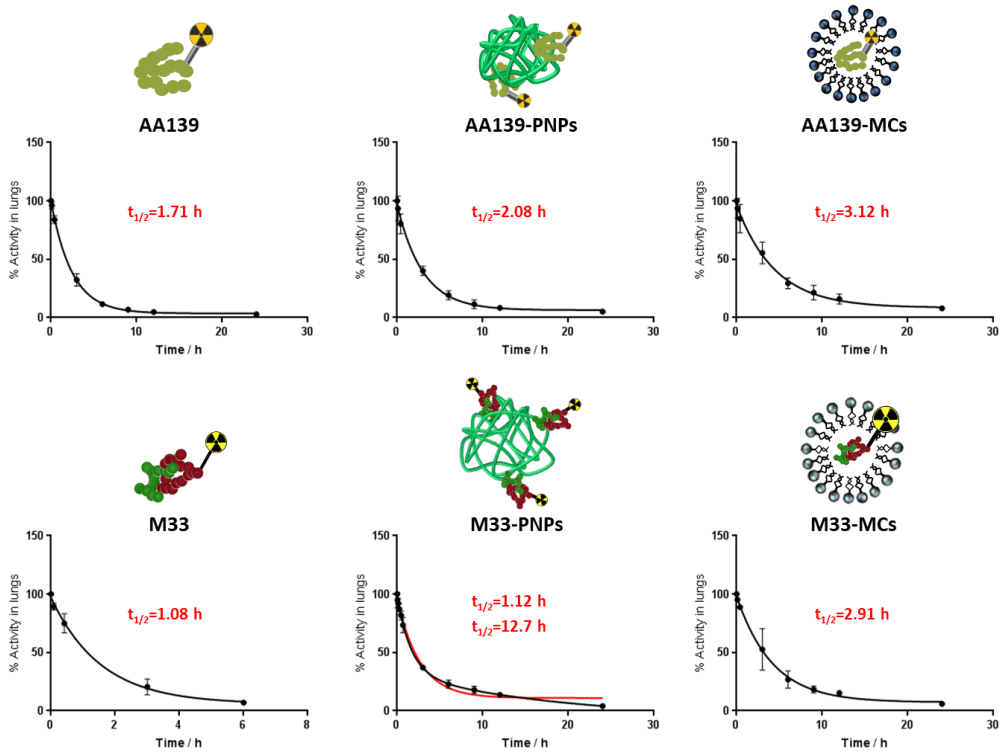

Figure 5.9. Decay curves for the different NSs, obtained from the *in vivo* quantification results. Half-life values are showed in red colour.

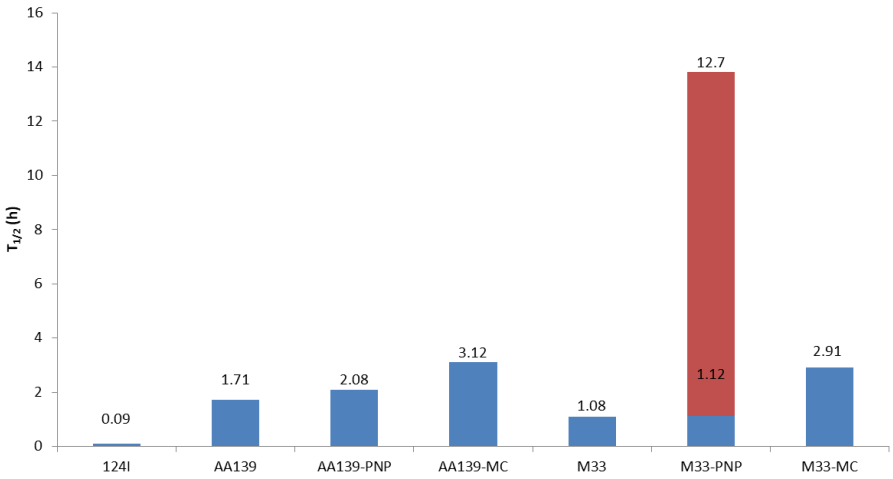

Figure 5.10. Summary of half-life values for all compounds, including [^{124}I]NaI (control). For M33-PNP, the short and long half-lives are represented in blue and red colour, respectively.

According to these results, both peptides were released from the polymeric nanocarriers relatively fast, suggesting that electrostatic interaction between the positively charged AMPs and PNPs (negatively charged) was not very stable *in vivo*. Similar dissociation of surface functionalizations attached via electrostatic interactions have been previously reported in the literature, for example in the case of gold nanoparticles (34) and superparamagnetic iron NPs (35, 36). Llop *et al* also studied the *in vivo* stability of protein coatings on poly(lactic*co*–glycolic) nanoparticles (PLGA-NPs) by nuclear imaging techniques (37). NPs' core and surrounding proteins were radiolabelled with two different gamma emitters and by energy discriminant single-photon emission computerised tomography (SPECT) their biodistribution pattern was assessed. The displacement of the proteins or peptides from the NPs could be related with the formation of protein-coronas (38, 39). Actually, in physiological environment (blood, lymph, mucus, complete cell culture media and other biological fluids) a large amount and variety of proteins is present, which can interact with the administered NSs (AMP-NP) and form protein-coronas around the NPs.

The results presented in this chapter were very useful to properly design the therapeutic-efficacy assays of these drugs carried out by project-partner Erasmus Medical Centre (Rotterdam, The Netherlands). By knowing the half-life of the drug at

different scenarios (free or attached to a NC) the dosing frequency to achieve the required amount of drug in the lungs could be determined.

5.4.2.3. Ex vivo experiments of selected NCs: PNPs and the corresponding parent polymer

When particles are administered by endotracheal insufflation, it is usually difficult to know the fraction that is deposited in the lungs with respect to the nebulised dose, especially in SPECT-CT experiments where absolute quantification is not possible. For this reason, *ex vivo* experiments of ^{67}Ga-PNPs and ^{67}Ga-Polymer immediately after administration were carried out. According to our results (using the Penn-Century MicroSprayer® Aerosolizer) 85±3% of the nebulised dose was deposited in the lungs independently of the nebulised compound. These results were used to correct the values obtained from the *ex vivo* studies of ^{67}Ga-Citrate, ^{67}Ga-PNPs and ^{67}Ga-Polymer (n=3 per compound and labelled species).

Ex vivo dissection and gamma counting results confirmed the trends observed *in vivo*. As it can be seen in Figure 5.11, >85% of the administered radioactivity was still in the lungs after 72 hours when labelled PNPs or the corresponding polymer were administered. On the contrary, almost 85% of the administered was cleared from the lungs at t=72 hours after administration of gallium citrate. Interestingly, at t=144 hours, almost 40% of administered PNPs were cleared from the lungs whereas the amount of polymer within the lungs remained almost unchanged.

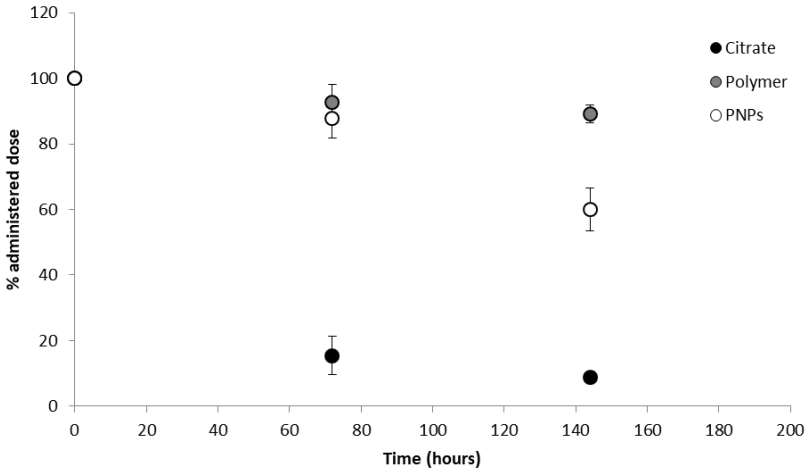

Figure 5.11 Percentage of administered radioactivity present in the lungs after endotracheal insufflation of ^{67}Ga-citrate (black dots), ^{67}Ga-labelled parent polymer (grey dots) and ^{67}Ga-labelled PNPs (white dots). Results are expressed as mean ± standard deviation, n=3.

These results confirm the long residence time of the PNPs as well as its corresponding parent polymer in the lungs. Moreover, they indicate that the way these polymers are organised has an effect on their release from the lungs. When polymers are collapsed forming in this way a NP, they are slowly washed out. On the contrary, when they are administered as polymers (not collapsed) they do not cross the lung membrane and remain in the lungs.

No examples tackling the investigation of the residence time of PNPs after lung administration using molecular imaging techniques have been found in the literature. However, some previous works have investigated other NP types using other analytical techniques and eventually *in vivo* imaging. For example, Anderson *et al.* investigated the residence time of 2 different sized AgNPs (20 and 110 nm) delivered to rats by single nose-only aerosol exposure (40). Rat lung tissue was assessed at different time points for silver accumulations using inductively-coupled plasma mass spectrometry (ICP-MS), autometallography, and enhanced dark field microscopy. According to their results, 56 days post-exposure at least 33% of the initial delivered dose was still present for both AgNPs. Similarly, Woods *et al* also studied the biological fate of Albumin NPs in the lungs by a combination of SPECT-CT *in vivo* imaging experiments

and *in vitro* studies (41). Authors found out that 48 hours post administration, almost 90% of radiolabelled albumin NPs remained in the lungs.

5.5. Summary and Conclusion

In this chapter, it has been demonstrated that nuclear imaging techniques are perfectly suited to investigate pharmacokinetic properties of drugs, drug carriers and their combination into nanosystems. Such determination has a definite incidence when defining the dosing regimen. The combination of nuclear imaging techniques reported here can be applied not only to the model systems assayed in the context of this PhD thesis, but to any novel nanomedicine as long as efficient radiolabelling strategies can be implemented.

5.6. References

1. Wang X, Yang L, Chen Z, Shin DM. Application of nanotechnology in cancer therapy and imaging. *CA Cancer Journal for Clinicians*. **2008**;58(2):97-110.

2. Torchilin VP. Targeted pharmaceutical nanocarriers for cancer therapy and imaging. *AAPS Journal*. **2007**;9(2):E128-E47.

3. Allen TM, Cullis PR. Drug Delivery Systems: Entering the Mainstream. *Science*. **2004**;303(5665):1818-22.

4. Hamaguchi T, Kato K, Yasui H, Morizane C, Ikeda M, Ueno H, et al. A phase I and pharmacokinetic study of NK105, a paclitaxel-incorporating micellar nanoparticle formulation. *British Journal of Cancer*. **2007**;97(2):170-6.

5. Plummer R, Wilson RH, Calvert H, Boddy AV, Griffin M, Sludden J, et al. A Phase i clinical study of cisplatin-incorporated polymeric micelles (NC-6004) in patients with solid tumours. *British Journal of Cancer*. **2011**;104(4):593-8.

6. Valle JW, Armstrong A, Newman C, Alakhov V, Pietrzynski G, Brewer J, et al. A phase 2 study of SP1049C, doxorubicin in P-glycoprotein-targeting pluronics, in patients with advanced adenocarcinoma of the esophagus and gastroesophageal junction. *Investigational New Drugs*. **2011**;29(5):1029-37.

7. Duncan R. Polymer conjugates as anticancer nanomedicines. *Nature Reviews Cancer*. **2006**;6(9):688-701.

8. Llop J, Gómez-Vallejo V, Gibson N. Quantitative determination of the biodistribution of nanoparticles: Could radiolabeling be the answer? *Nanomedicine*. **2013**;8(7):1035-8.

9. Brunetti J, Falciani C, Roscia G, Pollini S, Bindi S, Scali S, et al. In vitro and in vivo efficacy, toxicity, bio-distribution and resistance selection of a novel antibacterial drug candidate. *Scientific Reports*. **2016**;6.

10. van der Weide H, Brunetti J, Pini A, Bracci L, Ambrosini C, Lupetti P, et al. Investigations into the killing activity of an antimicrobial peptide active against extensively antibiotic-resistant K. pneumon iae and P. aeruginosa. *Biochimica et Biophysica Acta - Biomembranes*. **2017**;1859(10):1796-804.

11. Ščasnár V, van Lier JE. The use of SEP-PAK Sl cartridges for the preparation of gallium chloride from the citrate solution. *European Journal of Nuclear Medicine*. **1993**;20(3):273.

12. Hwang DW, Ko HY, Lee JH, Kang H, Ryu SH, Song IC, et al. A nucleolin-targeted multimodal nanoparticle imaging probe for tracking cancer cells using an aptamer. *Journal of Nuclear Medicine*. **2010**;51(1):98-105.

13. Stelter L, Pinkernelle JG, Michel R, Schwartländer R, Raschzok N, Morgul MH, et al. Modification of aminosilanized superparamagnetic nanoparticles: Feasibility of multimodal detection using 3T MRI, small animal PET, and fluorescence imaging. *Molecular Imaging and Biology*. **2010**;12(1):25-34.

14. Hunter WM, Greenwood FC. Preparation of iodine-131 labelled human growth hormone of high specific activity. *Nature*. **1962**;194(4827):495-6.

15. Leidy Jr JW. Reversed-phase high-performance liquid chromatographic purification of 125-I-labeled rat growth hormone-releasing hormone for radioimmunoassay. *Journal of Chromatography A*. **1989**;483(C):253-62.

16. Fraker PJ, Speck Jr JC. Protein and cell membrane iodinations with a sparingly soluble chloroamide, 1,3,4,6-tetrachloro-3a,6a-diphenylglycoluril. *Biochemical and Biophysical Research Communications*. **1978**;80(4):849-57.

17. Bolton AE, Hunter WM. The labelling of proteins to high specific radioactivities by conjugation to a ^{125}I containing acylating agent. Application to the radioimmunoassay. *Biochemical Journal*. **1973**;133(3):529-38.

18. Breslav M, McKinney A, Becker JM, Naider F. Preparation of radiolabeled peptides via an iodine exchange reaction. *Analytical Biochemistry*. **1996**;239(2):213-7.

19. Kim SW, Lee YK, Kim SH, Park JY, Lee DU, Choi J, et al. Covalent, Non-Covalent, Encapsulated Nanodrug Regulate the Fate of Intra- and Extracellular Trafficking: Impact on Cancer and Normal Cells. *Scientific Reports*. **2017**;7(1).

20. Hildebrandt N, Hermsdorf D, Signorell R, Schmitz SA, Diederichsen U. Superparamagnetic iron oxide nanoparticles functionalized with peptides by electrostatic interactions. *Arkivoc*. **2007**;2007(5):79-90.

21. Wang A, Perera YR, Davidson MB, Fitzkee NC. Electrostatic Interactions and Protein Competition Reveal a Dynamic Surface in Gold Nanoparticle-Protein Adsorption. *Journal of Physical Chemistry C*. **2016**;120(42):24231-9.

22. Hamman JH, Enslin GM, Kotzé AF. Oral delivery of peptide drugs: Barriers and developments. *BioDrugs*. **2005**;19(3):165-77.

23. Langguth P, Bohner V, Heizmann J, Merkle HP, Wolffram S, Amidon GL, et al. The challenge of proteolysis enzymes in intestinal peptide delivery. *Journal of Controlled Release*. **1997**;46(1-2):39-57.

24. Lim SB, Rubinstein I, Sadikot RT, Artwohl JE, Önyüksel H. A novel peptide nanomedicine against acute lung injury: GLP-1 in phospholipid micelles. *Pharmaceutical Research*. **2011**;28(3):662-72.

25. Kuzmis A, Lim SB, Desai E, Jeon E, Lee BS, Rubinstein I, et al. Micellar nanomedicine of human neuropeptide Y. *Nanomedicine: Nanotechnology, Biology, and Medicine*. **2011**;7(4):464-71.

26. Lim SB, Rubinstein I, Önyüksel H. Freeze drying of peptide drugs self-associated with long-circulating, biocompatible and biodegradable sterically stabilized phospholipid nanomicelles. *International journal of pharmaceutics*. **2008**;356(1-2):345-50.

27. Guo J, Wu T, Ping Q, Chen Y, Shen J, Jiang G. Solubilization and pharmacokinetic behaviors of sodium cholate/lecithin- mixed micelles containing cyclosporine A. *Drug Delivery: Journal of Delivery and Targeting of Therapeutic Agents*. **2005**;12(1):35-9.

28. Dagar S, Önyüksel H, Akhter S, Krishnadas A, Rubinstein I. Human galanin expresses amphipathic properties that modulate its vasoreactivity in vivo. *Peptides*. **2003**;24(9):1373-80.

29. Banerjee A, Onyuksel H. Human pancreatic polypeptide in a phospholipid-based micellar formulation. *Pharmaceutical Research*. **2012**;29(6):1698-711.

30. Sadikot RT, Rubinstein I. Long-acting, multi-targeted nanomedicine: Addressing unmet medical need in acute lung injury. *Journal of Biomedical Nanotechnology*. **2009**;5(6):614-9.

31. Krishnadas A, Önyüksel H, Rubinstein I. Interactions of VIP, secretin and PACP(1-38) with phospholipids: A biological paradox revisited. *Current Pharmaceutical Design*. **2003**;9(12):1005-12.

32. Önyüksel H, Séjourné F, Suzuki H, Rubinstein I. Human VIP-α: A long-acting, biocompatible and biodegradable peptide nanomedicine for essential hypertension. *Peptides*. **2006**;27(9):2271-5.

33. Önyüksel H, Ikezaki H, Patel M, Gao XP, Rubinstein I. A novel formulation of VIP in sterically stabilized micelles amplifies vasodilation in vivo. *Pharmaceutical Research*. **1999**;16(1):155-60.

34. Rambanapasi C, Barnard N, Grobler A, Buntting H, Sonopo M, Jansen D, et al. Dual radiolabeling as a technique to track nanocarriers: The case of gold nanoparticles. *Molecules*. **2015**;20(7):12863-79.

35. Freund B, Tromsdorf UI, Bruns OT, Heine M, Giemsa A, Bartelt A, et al. A simple and widely applicable method to 59Fe-radiolabel monodisperse superparamagnetic iron oxide nanoparticles for in vivo quantification studies. *ACS Nano*. **2012**;6(8):7318-25.

36. Wang H, Kumar R, Nagesha D, Duclos RI, Jr., Sridhar S, Gatley SJ. Integrity of ^{111}In-radiolabeled superparamagnetic iron oxide nanoparticles in the mouse. *Nuclear Medicine and Biology*. **2015**;42(1):65-70.

37. Llop J, Marradi M, Jiang P, Gómez-Vallejo V, Baz Z, Echeverría M, et al., editors. In vivo stability of protein coatings on poly lactic co glycolic nanoparticles. MRS Advances; 2016.

38. Casals E, Puntes VF. Inorganic nanoparticle biomolecular corona: Formation, evolution and biological impact. *Nanomedicine*. **2012**;7(12):1917-30.

39. Tenzer S, Docter D, Kuharev J, Musyanovych A, Fetz V, Hecht R, et al. Rapid formation of plasma protein corona critically affects nanoparticle pathophysiology. *Nature Nanotechnology*. **2013**;8(10):772-81.

40. Anderson DS, Patchin ES, Silva RM, Uyeminami DL, Sharmah A, Guo T, et al. Influence of particle size on persistence and clearance of aerosolized silver nanoparticles in the rat lung. *Toxicological Sciences*. **2015**;144(2):366-81.

41. Woods A, Patel A, Morgan A, Vasquez Y, Bruce K, A. Dailey L, et al. The fate of albumin nanoparticles in the 'black box' of the lung - In vivo investigations of albumin nanoparticle localisation into lung tissue, broncheoalveolar lavage cells and fluid 48 hours post-inhalation. *Journal of Aerosol Medicine and Pulmonary Drug Delivery*. **2015**;28:A22-A3.

Chapter 6. General conclusions

1- The preparation of the radiofluorinated gases [^{18}F]CF_4 and [^{18}F]SF_6 can be achieved following a simple method, based on a dual proton irradiation approach. This method results in higher production yields than direct proton irradiation of the fluorinated gases.

2- The radiofluorinated gases [^{18}F]CF_4 and [^{18}F]SF_6 are suitable tracers for the determination of regional lung ventilation using PET-CT, and may become powerful tools for the diagnostic, prognostic or evaluation of response to treatment in a wide variety of lung diseases.

3- Endotracheal insufflations of aqueous solutions into rats using the PennCentury microsprayer result in close-to-quantitative deposition of the aerosol in the lungs, with non-uniform distribution within the different lung regions and high intra-subject variability.

4- Lung administration of aerosols in rats using the commercially available Aeroneb nebuliser and the nebuliser developed by Ingeniatrics Tecnologías results in an homogeneous distribution of the aerosol within the lungs, although less than 0.1% of the nebulised solution is actually deposited in the lungs.

5- Nuclear imaging techniques are perfectly suited to investigate the pharmacokinetic properties of drugs, drug carriers and their combinations into nanosystems.

6- The residence time in the lungs of antimicrobial drugs after endotracheal insufflation can be prolonged by appropriate conjugation/entrapment with/into nanocarriers.

Acknowledgments

First of all, I would like to express my gratitude to Professor Manuel Martín Lomas and Professor Luis Liz-Marzán, former and current scientific directors of CIC biomaGUNE, respectively, for allowing me to conduct the experimental work of this PhD in the outstanding facilities of the centre. Thanks for the precious opportunity to get familiar with such an amount of diverse equipment in a multi-disciplinary, multi-cultural environment.

I would like to express my sincere appreciation and thanks to my research supervisor Dr. Jordi Llop for giving me the opportunity to undertake my PhD thesis under his supervision, teaching me many things about this fascinating field and for being very supportive throughout these four years. I am very grateful to be given the chance to be part of such an interesting project as the PneumoNP; it has allowed me to grow up not only at a professional level, but also at a personal level.

Special thanks also to Dr. Vanessa Gómez-Vallejo for her invaluable support since the very beginning. Thanks for all the encouraging words and help during the experimental work.

I take this moment to shower my word of gratitude to all my former and current colleagues in the Radiochemistry and Nuclear Imaging Group. It has been a pleasure meeting you all and working with you side by side in this entire journey. I will always remember all the good times down there.

Apart from my laboratory mates, I also want to thank people at CIC biomaGUNE that have helped me in one way or another throughout these years.

Nobody has been more important to me but my family members who supported me throughout the thesis project. Zorte handiko pertsona naiz zuek nere ondoan izateagatik. Hitzekin ezin da eskertu urte guzti hauetan eman didazuen animo eta babesa. Mila esker bihotzez.

Nola ez, nire eskerrik beroenak zuretzat, Ane. Zu zara abentura zoragarri honetan izan nezakeen bazkiderik onena; mila esker zure laguntza, babes eta pazientziarengatik.

Acknowledgments

Eskerrik asko urte guzti hauetan eman dizkidazun animo guztiengatik eta beti nigan sinisteagatik.